Analysis and Modeling of Uncooled Microbolometers with Tunable Thermal Conductance

by

Nezih Topaloglu

A thesis
presented to the University of Waterloo
in fulfillment of the
thesis requirement for the degree of
Doctor of Philosophy
in
Mechanical Engineering

Waterloo, Ontario, Canada, 2009

I hereby declare that I am the sole author of this thesis. This is a true copy of the thesis, including any required final revisions, as accepted by my examiners.

I understand that my thesis may be made electronically available to the public.

Abstract

Uncooled microbolometers have attracted significant interest due to their small size, low cost and low power consumption. As the application range of microbolometers broadens, increasing the dynamic range becomes one of the main objectives of microbolometer research. Targeting this objective, tunable thermal conductance microbolometers have been proposed recently, in which the thermal conductance is tuned by electrostatic actuation. Being a new concept in the field, the current tunable thermal conductance microbolometers have significant potential for improvement in design and performance. In this thesis, an extensive analysis of tunable thermal conductance microbolometers is made, an analytical model is constructed for this purpose, and solutions are proposed to some potential problems such as in-use stiction and variation in spectral response.

The current thermal conductance tuning mechanisms use the substrate for electrostatic actuation, which does not support pixel-by-pixel actuation. In this thesis, a new thermal conductance tuning mechanism is demonstrated, that enables pixel-by-pixel actuation by using the micromirror as an actuation terminal instead of the substrate. In addition, a stopper mechanism is used to decrease the risk of in-use stiction. With this new mechanism, the thermal conductance can be tuned by a factor of three at relatively low voltages, making it a promising thermal conductance tuning mechanism for adaptive infrared detectors.

Effective estimation of the performance parameters of a tunable thermal conductance microbolometer in the design state requires an analytical model that combines the physics of infrared radiation detection and the thermal conductance tuning mechanisms. As a part of this research, an extensive analytical model is presented, which includes the electrostatic-structural modeling of the thermal conductance tuning mechanism, and electromagnetic and thermal modeling of the microbolometer. The accuracy of the thermal model is of significant importance as the operation of the tuning mechanism within the desired range should be verified in the design stage. A thermal model based on the solution of the microbolometer heat conduction equation is established, which is easily applicable to conventional and tunable thermal conductance microbolometers of various shapes. The constructed microbolometer model is validated by experiments and finite element model simulations.

Furthermore, the effect of thermal conductance tuning on spectral response is analyzed. The present thermal conductance tuning mechanisms result in variations in spectral response, which is an undesired effect in many applications. As a solution, a new microbolometer architecture is proposed, in which the spectral response is not affected by thermal conductance. The microbolometer is designed using an analytical model and its performance is characterized by finite element model simulations. To realize the proposed design, a fabrication process flow is offered. It is shown that the proposed microbolometer exhibits high performance, tunable thermal conductance and constant spectral response.

Acknowledgements

First and foremost, I am deeply grateful to my advisors, Dr. Patricia M. Nieva, Dr. Mustafa Yavuz and Dr. Jan P. Huissoon for their continuous support and guidance during my graduate studies. I cannot thank them enough for their constant management and friendly assistance that helped me improve my technical skills and academical knowledge.

I would like to express my gratitude to Dr. Ted Hubbard of Dalhousie University for serving as my external examiner. I also thank to my committee members Dr. Eihab Abdel-Rahman, Dr. Richard Culham and Dr. Amir Khajepour, for their suggestions and advice.

I would like to thank my colleagues Dr. Shavezipur and Jim Kuo for their help and technical discussions. I also thank Dr. Xiaogang Li, Dr. Yuquan Ding and Aashish S. Shah for their thoughtful help during my experimental measurements.

Thanks to my officemates M. Said Boybay and Caglar Elbuken. Let me also say "thank you" to Onur Gunduz, S. Aylin Gurses, Ezgi Akin and Cem E. Sozgen. I am blessed with their endless friendship and support that I will never forget through my whole life. Thank you to all my dearest friends.

Finally, I extend my deepest thanks to my parents Vildan and Ragip Topaloglu, my grandfather Ahmet Topaloglu, and my dear sister Hande Topaloglu for their love and faithful support.

To my father

Contents

List of Tables

List of Figures

Nomenclature

α	Temperature coefficient of resistance (TCR) [K^{-1}]
α	Thermal diffusivity [m^2/sec]
β	Eigenvalue [$1/sec^{1/2}$]
ϵ	Permittivity [F/m]
ϵ_r	Relative permittivity [dimensionless]
η	Coupling efficiency [dimensionless]
Γ	Overall reflection coefficient [dimensionless]
γ	Volumetric heat capacity [$J/(m^3K)$]
κ	Pixel fill-factor [dimensionless]
λ	Relative mean plane separation [dimensionless]
λ	Wavelength [μm]
μ	Permeability [H/m]
μ_r	Relative permeability [dimensionless]
ν	Poisson's ratio [dimensionless]
ω	Frequency of the incoming IR wave [rad/sec]
ω	Modulation frequency [rad/sec]
Φ	Angle of torsional twist [rad]
Ψ_k	Stress function (Swanson's Method) [N rad]

$\Re$	Responsivity [V/W]
ρ	Density [kg/m^3]
σ	Conductivity [1/(Ω m)]
σ	Effective surface roughness [nm]
σ	Stefan-Boltzmann constant [J /(sec m^{2}K^4)]
σ_{sd}	Skin depth [μm]
τ	Thermal time constant [sec]
θ	Bending angle [rad]
θ	Excess temperature [K]
θ_{avg}^{SS}	Area-averaged microplate temperature change at steady-state [K]
A	Area [μm^2]
A_a	Apparent contact area [μm^2]
A_r	Real contact area [μm^2]
A_{mp}	Microplate area [μm^2]
C	Thermal capacitance [J/K]
c	Specific heat capacity [J/(kg K)]
C_{el}	Electrical capacitance [pF]
E	Young's modulus [N/m^2]
EI	Bending stiffness [N m^2]
F_{ES}	Electrostatic attraction force [N]
F_{mech}	Mechanical restoring force [N]
F_{no}	Number of optics [dimensionless]
G	Thermal conductance [W/K]

G	Torsional modulus of rigidity [N/m^2]
g	The gap between the base plate and the movable plate [μm]
g_0	The gap between the base plate and the movable plate in the unactuated state [μm]
$g_{contact}$	The gap between the base plate and the movable plate at the contact state [μm]
$g_r(x,t)$	Heat generation function for region r [W/m^3]
h	Planck constant [J sec]
h_c	Contact conductance [W/(K m^2)]
H_e	Elastic microhardness [N/m^2]
I	Area moment of inertia [μm^4]
I_b	Bias current [A]
k	Propagation constant [rad/μm]
k	Thermal conductivity [W/(m K)]
k_B	Boltzmann constant [J/K]
k_s	Effective thermal conductivity of the joint [W/(m K)]
k_{eq}	Equivalent spring constant [N/m]
KG	Torsional stiffness [N m^2]
L	Length [μm]
L_T	Radiance of the target [W/(sr m^2)]
M	Moment [N m]
m	Effective mean asperity slope [dimensionless]
n	Contact spot density [1/m^2]
P	Contact pressure [N/m^2]

P_0	Incident radiation peak power on the microplate [W]
P_{abs}	Absorbed radiation peak power on the microplate [W]
P_{el}	Power generated by Joule heating [W]
P_{in}	Radiation power incident on the microplate [W]
P_{IR}	Incident radiation power on the pixel [W]
R	Resistance [Ω]
r	Contact spot radius [nm]
r	Reflection coefficient [dimensionless]
R_c	Contact resistance [K/W]
$R_{shape-A}$	Constriction resistance of shape-A half-microbolometer [K/W]
$R_{shape-B}$	Constriction resistance of shape-B half-microbolometer [K/W]
$S(z)$	Complex Poynting vector at position z [W/m^2]
T	Microplate temperature [K]
T	Twisting moment [N m]
t	Time [sec]
t	Transmission coefficient [dimensionless]
T_s	Substrate temperature [K]
$v(x)$	Elastic curve function [μm]
V_b	Bias voltage [V]
V_{act}	Actuation voltage [V]
$V_{contact}$	Contact voltage [V]
W	Width [μm]
$X_{rn}(x)$	nth eigenvector for region r [dimensionless]

Y	Admittance [Ω^{-1}]
Z	Thickness [μm]
z_{tr}	Relative truncation level [dimensionless]
CMR	Colossal magnetoresistive
DI	Deionized
FEM	Finite element model
FPA	Focal planar array
HFSS	High-Frequency Structural Simulator
IR	Infrared
LPCVD	Low-Pressure Chemical Vapor Deposition
LWIR	Long Wave Infrared
MUMPs	Multi-User MEMS Processes
MWIR	Medium Wave Infrared
NEP	Noise equivalent power
PECVD	Plasma Enhanced Chemical Vapor Deposition
PSG	Phosphosilicate glass
PVD	Physical vapor deposition
RIE	Reactive Ion Etching
SEM	Scanning Electron Microscope
TCC	Thermal contact conductance
TEM	Transverse electromagnetic

Chapter 1

Introduction

Infrared (IR) radiation is a form of electromagnetic radiation covering the frequency range between microwave and visible light in the electromagnetic spectrum. Devices that sense IR radiation are called IR detectors. IR detectors can be classified into two groups: photon detectors and thermal detectors. Photon detectors are extensively used in military and astronomical applications, due to their high sensitivity and fast response time. However, they require bulky and expensive cryogenic coolers, which make them too expensive for commercial applications. Thermal detectors are smaller in size, offer low power consumption and can be operated at room temperature [6]. These characteristics result in cheaper imaging systems that have been applied to a broad range of military and civilian consumer applications, such as air-to-air and land-to-air missiles, search and rescue, night vision goggles, fire detection, crack determination and medical imaging [7, 8]. Consequently, the demand for uncooled IR detectors has steadily increased over the past several years.

Among different types of uncooled infrared detectors (pyroelectric detectors, thermopiles and resistive microbolometers), resistive microbolometers are one step ahead due to their reliability, high sensitivity and simplicity of fabrication [8, 9]. *A resistive microbolometer*, which is referred in this dissertation as a *microbolometer*, is a microstructure that converts the IR radiation to electrical voltage. In this device, a fraction of the incoming IR radiation is absorbed by a planar IR sensitive structure (or microplate), which is suspended above the substrate by two long arms. The fraction of the absorbed infrared radiation is called the coupling efficiency (η), and depends on the material properties and thicknesses of the thin films constituting the microbolometer, the thickness of the gap between the microplate and the

substrate, and the wavelength of the IR radiation. After absorbing the incoming IR radiation, the temperature of the microplate increases, which means that the electromagnetic energy (IR radiation) is converted into thermal energy (temperature increase). The temperature increase of the microplate results in a change of its electrical resistance. This change is sensed by converting it to an electrical signal by biasing the microplate through the arms with a constant current or voltage.

To prevent the dissipation of absorbed radiation power to the environment, the microplate is thermally isolated from the environment, both by fabricating the microplate so it is suspended above the substrate and by packaging it in vacuum. The parameter that gives the measure of how well the microplate is thermally isolated from the substrate is the thermal conductance (G). Lower thermal conductance means higher thermal isolation, which results in higher microbolometer sensitivity since the absorbed IR power will result in a higher temperature rise within the microplate. However, low thermal conductance will also result in a high thermal time constant, which in turn results in a microbolometer with low video frame-rate. Therefore, careful consideration of the thermal conductance is required at the design stage to optimize sensitivity without compromising speed.

Over the last few years, there has been an increased interest in using microbolometers for imaging in harsh environments. The dynamic range of conventional microbolometers is not suitable for usage in harsh environments [4]. For example, when a high temperature scene such as an explosion is imaged, the IR power coming from the scene can lead to an excessive temperature increase in the microplate, which results in undesirable effects on the resulting image, such as temporary afterimage and blindness. In addition, excessive temperature increase at the microplate can damage the device mechanically, leading to plastic deformation, buckling and ultimately device failure. These problems gave rise to the idea of a tunable thermal conductance microbolometer. In a tunable thermal conductance microbolometer, the thermal conductance is increased temporarily, to prevent excessive temperature increase on the microplate when a high temperature scene is imaged. In addition, since increasing the thermal conductance decreases the sensitivity and increases the video frame rate, by adjusting the thermal conductance, the end user gains an opportunity to switch between high sensitivity and high frame rate. These key features make tunable thermal conductance microbolometers a great candidate for the next generation of uncooled infrared detectors [4].

This thesis presents an extensive analysis of tunable thermal conductance microbolometers (referred to hereinafter as on *tunable G microbolometers*), and addresses the problems in their thermal conductance tuning mechanisms (referred to as *G tuning mechanisms*). Existing microbolometer models are improved and extended for the case of tunable G microbolometers. Finally, a new microbolometer pixel design with a tunable G is introduced for which the spectral response remains unaffected.

1.1 Motivation

Although tunable G microbolometers have received much attention among researchers since the first demonstration of the actuation mechanism in 2002, the related literature available on the subject is scarce. Moreover, there is a need for a more accurate thermal analysis and the investigation of problems and potential risks associated with their operation.

The operation of a microbolometer is based on electromagnetic wave theory and thermal conduction, whereas the typical operation of a G tuning mechanism is based on beam bending due to electrostatic actuation. Therefore the modeling of a tunable thermal conductance microbolometer requires a multidisciplinary analysis. The literature available for tunable G microbolometers does not use any model that combines the electrostatic-structural modeling of the G tuning and the electromagnetic and thermal modeling of the microbolometer operation. Designs of the microbolometer pixel are based on finite element model simulations instead.

Accurate thermal modeling is an important aspect of microbolometer design, since the detector performance depends strongly on this. The accuracy of the thermal model becomes even more important in a tunable G microbolometer, since proper operation of the tuning mechanism within the desired tunability range should be verified at the design stage. Existing thermal models assume that the temperature of the microplate is uniform, and they only consider a linear temperature drop within the microbolometer arms for the determination of thermal parameters. The effect of the microplate dimensions and the general aspects of the microbolometer shape such as the location of the microplate-arm connection are not considered, resulting in significant errors in the estimation of the thermal

parameters. In addition, existing thermal models do not estimate specifically the thermal conductance of a tunable G microbolometer. Finally, the relationship between the thermal conductance tuning mechanism and the spectral response needs consideration as well. The gap thickness between the microplate and the substrate changes during electrostatic attraction, resulting in a change of the IR absorption spectrum, namely a change in the spectral dependance of the coupling efficiency η. This change in absorption spectrum is undesired, since it leads to distortion in the resulting image.

The G tuning mechanism is obtained by deflecting the microplate to the substrate by electrostatic actuation [4, 5], which is realized by applying a voltage (actuation voltage) between the microplate and the substrate. However, when the substrate is biased, the whole microbolometer array is actuated. This does not allow pixel-by-pixel actuation, which is necessary for simultaneous imaging of hot and cold regions. In addition, the high voltage on the substrate can adversely affect the proper operation of the other components on the chip. Finally, due to the in-use stiction of the microplate to the substrate, the deflection of the microplate may also be a potential risk. Hence, the main motivation of this dissertation is to fulfill the requirement of a thorough investigation of thermal conductance of uncooled microbolometers, and more specifically, uncooled microbolometers with tunable thermal conductance.

1.2 Objectives

The research objectives explained above can be itemized as follows:

- Develop a complete analytical model for tunable thermal conductance microbolometers, that combines the physics of IR radiation detection and thermal conductance tuning mechanisms. This model includes:
  - Estimation of the coupling efficiency, based on the propagation of electromagnetic waves in a multi-layer medium (infrared absorption model).
  - Estimation of thermal conductance and thermal capacitance, based on the solution of heat conduction equation (thermal model). The model can be easily modified to account for many other pixel architectures.

The temperature distribution within the microplate is also taken into account.

  - Estimation of the microplate deflection as a function of the actuation voltage (electrostatic-structural model).

- Develop and demonstrate an effective pixel-by-pixel thermal conductance tuning mechanism, which can be used in next generation adaptive microbolometers.

- Design a novel pixel architecture that offers a tunable thermal conductance for which the absorption spectrum does not change due to thermal conductance tuning.

1.3 Organization of the Thesis

This dissertation can be divided into three main parts: design and development of a new G tuning mechanism for microbolometers (Chapter 2), modeling and experimental verification of the new mechanism (Chapters 3 and 4), and tunable G microbolometers with constant spectral response (Chapter 5).

Following the motivation and objectives given in Chapter 1 of this thesis, Chapter 2 starts with a review of microbolometer theory, the parameters that characterize detector performance, the existing thermal modeling approaches and tunable G microbolometers. The motivation behind the idea of tunable G microbolometers is explained in this chapter and an effective G tuning mechanism is developed. The details of the design and fabrication process are also included.

Chapter 3 describes the modeling of the proposed G tuning mechanism, including the infrared absorption model, the thermal model, the electrostatic-structural model, and a finite element model. The results of these models are compared to finite element model simulations and experimental results in Chapter 4. As the result of the experiments, the proper operation of the proposed mechanism is verified.

Chapter 5 addresses the spectral distortion problem in current tunable thermal conductance microbolometer designs, and a new pixel architecture is proposed and developed to provide tunable thermal conductance without changing the spectral absorption. For this purpose, a typical fabrication process flow is suggested. The

performance of this new proposed architecture is analyzed with finite element model simulations.

Chapter 6 summarizes the contributions of this study and suggests some potential directions for future work.

Chapter 2

Background and Literature Review

In this chapter, a review of microbolometer theory, current thermal modeling approaches and tunable thermal conductance microbolometers is presented. Problems with the existing tuning mechanisms are explained and an efficient thermal conductance tuning mechanism is proposed.

2.1 Uncooled Microbolometers

2.1.1 Operation

Infrared detectors are fabricated in a two-dimensional array structure, known as a focal planar array (FPA). The number of pixels in a FPA defines the resolution of the thermal image. The microbolometer design theory is constructed by defining and solving the heat balance equation of a single pixel.

Fig. 2.1 depicts a simple and typical microbolometer pixel. The pixel consists of a microplate, which is a stack of thin-film layers connected to the substrate by two long arms. The top layer of the microplate, called the absorber layer, absorbs the infrared radiation incident on it, and hence the temperature of the microplate increases. The electrical resistivity of one of the thin-film layers forming the microplate is strongly dependent on its temperature. This layer is called the IR

sensitive layer, and due to its temperature-dependent resistivity, the temperature increase due to incoming IR radiation changes the overall electrical resistance of the microplate. By applying a bias current or voltage through the arms, the resistance change can be measured electrically.

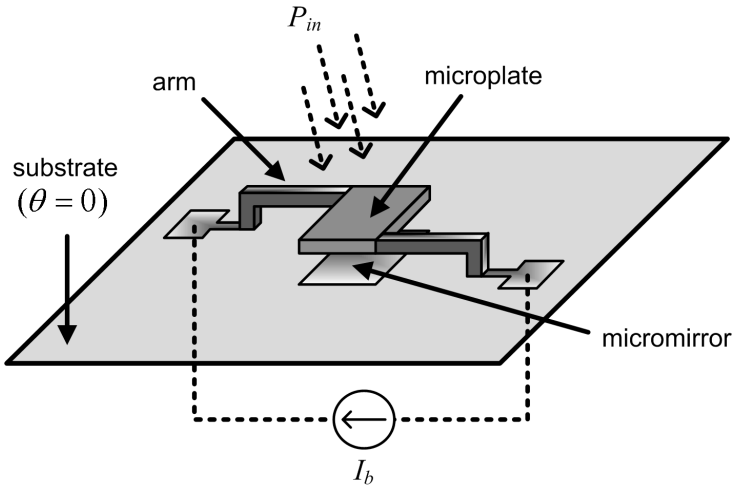

Figure 2.1: Basic structure of an uncooled microbolometer pixel.

In order to understand the sensing mechanism, the microbolometer heat equation should be solved. Assuming no electrical biasing, the heat equation is given by

$$C\frac{d\theta}{dt} + G\theta = P_{in}, \tag{2.1}$$

where C is the thermal capacitance (heat capacity), G is the thermal conductance, P_{in} is the incident radiation power and θ is the excess temperature, defined as

$$\theta = T - T_s, \tag{2.2}$$

where T is the microplate temperature and T_s is the temperature of the substrate.

Usually, the incident radiation is modulated by using a mechanical chopper. In this case, P_{in} can be expressed as

$$P_{in} = \eta P_0 e^{j\omega t} = P_{abs} e^{j\omega t}, \tag{2.3}$$

where P_0 is the incident radiation peak power, ω is the modulation frequency and η is the coupling efficiency, which is defined as the ratio of the absorbed radiation to the total incident radiation (P_{abs}/P_0), or simply the percentage of the incident

infrared radiation that is "used" by the microplate. Most microbolometers have a micromirror below the microplate, which reflects back the radiation incident on it, thus increasing the coupling efficiency (see Fig. 2.1).

The solution to the heat equation is given as:

$$\theta(t) = \frac{\eta P_0}{G\sqrt{1+\omega^2\tau^2}}\left(1 - e^{-\frac{t}{\tau}}\right), \tag{2.4}$$

where τ is the thermal time constant, expressed as:

$$\tau = \frac{C}{G}. \tag{2.5}$$

The second term of Eq. (2.4) converges to zero at steady-state, yielding

$$\theta_{ss} = \frac{\eta P_0}{G\sqrt{1+\omega^2\tau^2}} \tag{2.6}$$

as the steady-state temperature change θ_{ss}, due to the incident radiation with peak power P_0.

In the case when a bias current is applied through the arms for readout, a new term (P_{el}) is added to the right-hand side of Eq. (2.1), giving:

$$C\frac{d\theta}{dt} + G\theta = P_{in} + P_{el}, \tag{2.7}$$

where P_{in} is the incident radiation power given by Eq. (2.3), and P_{el} is the power generated by electrical biasing (electrical Joule heating). Defining I_b as the bias current, P_{el} is given by

$$P_{el} = I_b^2 R(\theta), \tag{2.8}$$

where $R(\theta)$ is the electrical resistance of the microplate. The temperature dependence of the resistance is stated as:

$$R(\theta) = R_0(1 + \alpha\theta), \tag{2.9}$$

where α is the temperature coefficient of resistance (TCR), given by

$$\alpha = \frac{1}{R_0}\frac{dR}{dT}. \tag{2.10}$$

The solution of the heat balance Eq. (2.7) can be found as:

$$\theta(t) = \frac{\eta P_0}{G_{eff}\sqrt{1+\omega^2\tau_{eff}^2}}\left(1 - e^{-\frac{t}{\tau_{eff}}}\right), \tag{2.11}$$

where G_{eff} is the effective thermal conductance, given by

$$G_{eff} = G + I_b^2 \alpha R_0 \tag{2.12}$$

and τ_{eff} is the effective thermal time constant, given by

$$\tau_{eff} = \frac{C}{G_{eff}}. \tag{2.13}$$

The changes in G and τ are the result of the electrothermal feedback due to the temperature dependence of the microplate resistance. If the temperature increase of the microplate is small enough ($\alpha\theta << 1$), this effect becomes negligible ($G_{eff} \approx G$).

The temperature increase is determined by measuring the change in output voltage ΔV_{out}, according to the formula

$$\Delta V_{out} = I_b \left(R(\theta) - R_0\right) = I_b R_0 \alpha \theta. \tag{2.14}$$

Eqs. (2.6) and (2.14) are the two main formulae that identify the sensing mechanism of the microbolometer. Eq. (2.6) represents the conversion of IR radiation to temperature increase, and in Eq. (2.14), the relationship between the output voltage and temperature increase is given. Combining Eq. (2.6) and Eq. (2.14), the direct relationship between the input power and the output potential difference can be found

$$\Delta V_{out} = \frac{\eta P_0 I_b R_0 \alpha}{G\sqrt{1 + \omega^2 \tau^2}}. \tag{2.15}$$

This completes the basic microbolometer theory. In the next section, the parameters that define the microbolometer performance are reviewed.

2.1.2 Performance Parameters

In the previous section, the solution to the microbolometer heat balance equation was provided, and as a result, the temperature increase θ at the microplate is found. In this section, the parameters that characterize the detector performance are defined, and the effect of various design parameters, such as G, C and η on detector performance are elaborated.

- **Responsivity ($\Re$):** Responsivity is defined as the output voltage signal divided by the input IR power incident on a microbolometer pixel (P_{IR}). The

relationship between P_{IR} and the power incident on the microplate (P_0) is given by

$$P_0 = \kappa P_{IR}, \tag{2.16}$$

where κ is the fill-factor, defined as the ratio of the microplate area to the pixel area. Using Eq. (2.15) and Eq. (2.16), $\Re$ can be expressed as

$$\Re = \frac{\Delta V_{out}}{P_{IR}} = \frac{\eta \kappa I_b R_0 \alpha}{G\sqrt{1+\omega^2\tau^2}}. \tag{2.17}$$

Responsivity is the main parameter that characterizes the "gain" of the microbolometer, and it is the basic figure-of-merit of the detector performance.

Eq. (2.17) indicates that responsivity increases by decreasing the thermal conductance G and by increasing the coupling efficiency η, fill-factor κ, bias current I_b, microplate resistance R_0 and temperature coefficient of resistance α. Within these parameters, I_b and R_0 can not be increased without bound; otherwise excessive Joule heating from the bias source can lead to overheating and failure of the pixel. Therefore, the main design parameters that can be tailored to increase the responsivity are η, κ, α and G. Among these parameters, α is the property of the IR sensitive material, and therefore only choosing an IR sensitive material with higher TCR will increase α. On the other hand, the other parameters depend on the pixel geometry as well as the material properties of the layers forming the pixel.

- **Thermal time constant (τ):** The thermal time constant is defined as the time for the excess temperature $\theta(t)$ to reach $\sim 63\%$ of its steady-state value, following a step change in input power. Therefore, it defines the response speed of the microplate temperature to a change in input power. The frame video rate of the imaging system is limited by τ. For instance, a video frame rate of 30 Hz requires the time constant to be less than 15 msec [10].

  The expression for τ was previously defined in Eq. (2.5) as the ratio of the thermal capacitance C to the thermal conductance G. According to this expression, in order to reduce τ, C should be decreased and G should be increased. Reducing C may be a good idea, however increasing G would end up in a lower responsivity $\Re$. Therefore, to increase $\Re$, a reduction in G should be made in conjunction with a reduction in C, so as to keep τ in a predefined range.

- **Noise equivalent power (NEP):** Responsivity is a good measure of microbolometer performance, however it does not take electrical noise into account. Noise equivalent power, defined as the minimum IR power a detector can *see* [11], can be formulated as

$$NEP = \frac{n}{\Re}, \tag{2.18}$$

where $\Re$ is responsivity and n is noise spectral density, defined as the noise that would occur if the electrical bandpass was reduced to 1 Hz.

- **Detectivity (D^*):** NEP is a convenient measure for predicting the minimum power a given system can detect; however, it is not "size-normalized". Detectors of different sizes have different NEPs, so a generalization for an optimum NEP cannot be made unless the microplate area is specified. Detectivity (also referred to as specific detectivity) can be expressed as

$$D^* = \frac{\Re\sqrt{A_{mp}}}{n}, \tag{2.19}$$

where A_{mp} is the microplate area.

2.1.3 Review of Uncooled Microbolometers

Improvement of the microbolometer performance can be classified mainly under two research titles:

- Material design: Research on a low-noise and high-TCR IR sensitive material
- Pixel design: Improving the pixel structure to enhance responsivity and/or thermal time constant

In this section, a general review on the improvements on the IR sensitive material research and pixel design is given.

Material Design:

The first microbolometer arrays employed metal films as IR sensitive materials, such as nickel (Ni), nickel-iron (Ni-Fe), titanium (Ti), Platinum (Pt), etc. These

films have low low-frequency (1/f) noise and their deposition rates can be well-controlled; however they have very low TCR (0.42 %/K for Ti [12] and 0.18 %/K for Pt [13]). In addition to low TCR, the low resistance values of these films also limit their responsivity (recall Eq. (2.17)).

Semiconductor films usually have negative TCRs, and the absolute value of their TCR is higher than that of metal films, which makes them promising IR sensitive materials. In addition, most are compatible with standard CMOS fabrication process. Some semiconductor thin films successfully used in microbolometers are poly silicon-germanium (Poly Si-Ge) [14, 15], hydrogenated amorphous silicon (a-Si:H) [16], and amorphous silicon-germanium [17, 18]. Among these semiconductor films, the most promising candidate appears to be a-Si:H, with a TCR ranging from -2.5 %/K for low-resistivity films to 8 %/K for high-resistivity films. However, the high TCR values are accompanied by a high level of 1/f noise [19].

Thin films of mixed vanadium oxides are also commonly used in microbolometer fabrication [20, 21], since they assure a combination of high TCR (around $\sim$2 %/K), low noise and moderate values of electrical resistivity (0.1-10 Ωcm [21]). Responsivities up to 2.5×10^7 V/W have been obtained with state-of-art vanadium oxide microbolometers [22]. However, the high-TCR region of vanadium oxide films is observed around 320 K to 340 K [23], which is higher than the standard operation temperature of a microbolometer (300 K), and the maximum TCR is limited to 6 %/K [24]. In addition, the fabrication of low-noise and high-TCR vanadium oxide thin films requires carefully controlled deposition conditions and high-temperature annealing steps. In addition, some hysteresis is present in the temperature-resistivity curve of VO_2 [25], a very common vanadium oxide compound used in microbolometers. The hysteresis problem can be partially solved by fabricating vanadium oxide films free of the VO_2 compound, which is a very challenging task.

Very encouraging results have also been obtained using new materials, such as semiconducting Yttrium-Barium-Copper-Oxide [26, 27] (YBCO), hydrogenated silicon carbide (Si:C:H) [28], and colossal magnetoresistive (CMR) manganites, such as La-Sr-MnO_3, La-Ca-MnO_3, La-Ba-MnO_3 [29–33]. Typical values of TCR are around $\sim$3 %/K for YBCO, $\sim$6 %/K for Si:C:H and $\sim$5-30 %/K for CMR manganites. However, the fabrication complexity and the 1/f noise level increases with increasing TCR [30]. The recent review article by Todd et al [31] provides a nice

overlook of the CMR manganite materials research for microbolometers.

Pixel Design:

Researchers have designed numerous different microbolometer pixels, to increase the detector performance. The primary aim of most of these designs is to enhance the responsivity by decreasing the thermal conductance G, and/or increasing the coupling efficiency η and the fill-factor κ, whereas some designs aimed on reducing the thermal time constant by decreasing the thermal capacitance C.

Five different pixel architectures, designed to increase thermal isolation, are shown in Figure 2.2. Three conventional pixel architectures, where the arms and the microplate are at the same level, are shown in Fig. 2.2(a),(b) and (c). The aim of the design in Fig. 2.2(b) is to increase the fill-factor and to decrease the overall pixel area, with a slight increase in G [34]. An effective way to decrease G is to fabricate thinner and longer arms. However, as the arms get longer, they occupy more area, which decreases the pixel fill-factor (see Fig. 2.2(c)). To avoid this trade-off, a hidden arm architecture was developed, where the arms are deposited underneath the microplate [35]. These devices are also referred as double-stage microbolometers (see Fig. 2.2(d) and (e)). Since the hidden-arm structure enables the length of the arms to be greatly increased without decreasing the fill-factor, numerous designs, where the arms fill most of the gap underneath the microplate, have been fabricated, such as the zigzag arm structure in Fig. 2.2(e) [1, 5, 36]. However in these cases, the arms partly block the infrared radiation propagating the gap below the microplate, so they degrade the coupling efficiency.

Enhancing the coupling efficiency η is another method to increase responsivity. Depositing a micromirror on top of the substrate, below the microplate, creates a resonant cavity between the micromirror and the microplate, which increases the coupling efficiency (see Figure 2.1). The gap between the micromirror and microplate is around $\lambda/4$ where λ is the wavelength of interest. Another method that increases η is to deposit a very thin (a few nanometers) metal absorber layer, such as Titanium [37] or goldblack [38], on top of the microplate. However, as the number of stacked layers constituting the microplate increases, the fabrication becomes more complex, and more buffer layers are required in order to minimize the residual stress on the microplate prior to sacrificial layer release, which is based on

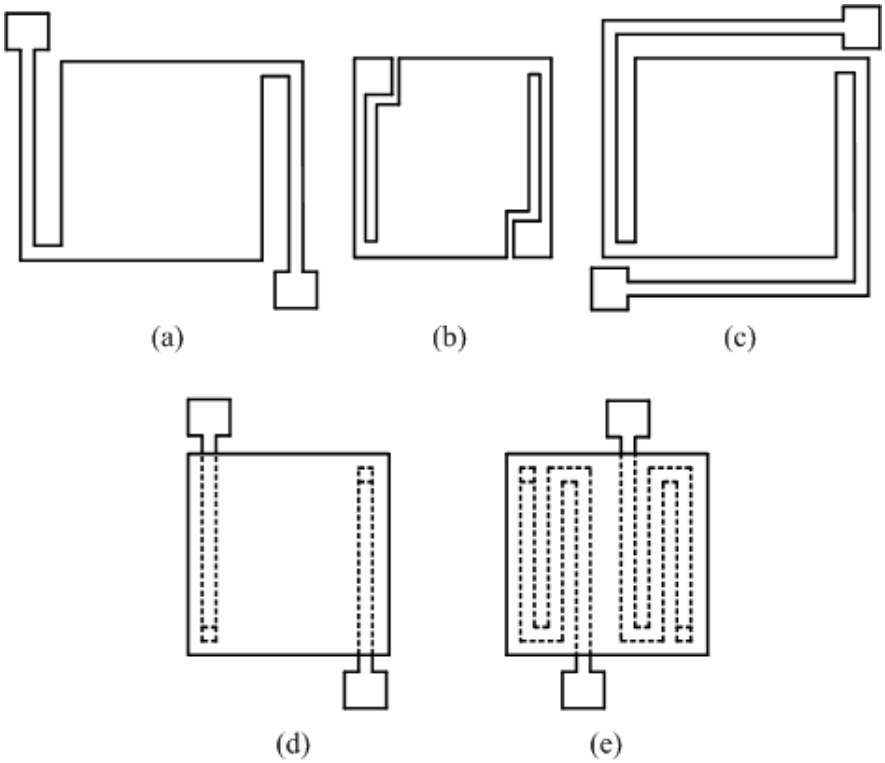

Figure 2.2: Single and multi-level pixel designs: (a), (b), (c) are single-level designs, (d), (e) are multi-level designs

lattice parameter mismatch. This results in an increase in the thermal capacitance C, which raises the thermal time constant of the detector.

According to Eq. (2.5), the thermal time constant can be reduced in two ways: increasing G, and decreasing C. Increasing G is not feasible since it results in less responsivity. Decreasing C can be done most effectively by decreasing the mass of the microplate [3, 39]. Almasri et al. [3] developed a microbolometer which has a microplate that consists only of a self-supporting 400 nm YBCO thin-film, and the thermal capacitance of the overall device was measured as $\sim 3.5 \times 10^{-10}$ J/K. However, since no absorber layer is used, the coupling efficiency η is fairly low (30 %). An SEM image of this microbolometer pixel array is shown in Fig. 2.3. Another method to decrease C is to decrease the pixel size, which also has additional advantages such as enhanced pixel resolution and decreased cost, weight and size of the camera optics [8]. However, decreasing the pixel size presents significant challenges in the fabrication process, pixel design and noise reduction.

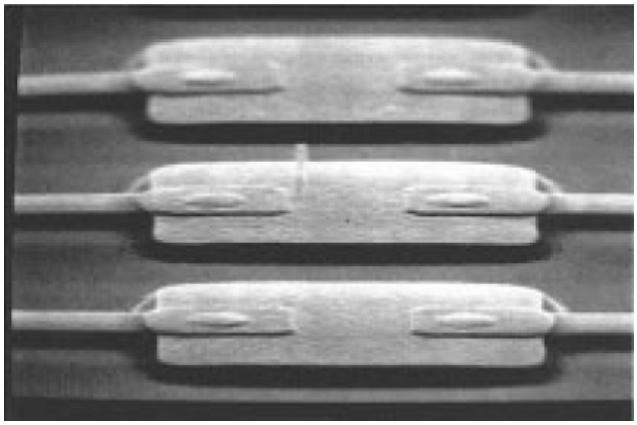

Figure 2.3: SEM image of the microbolometer pixel array with a self-supporting 400 nm YBCO microplate. Reprinted from [3].

2.2 Review of Thermal Modeling of Uncooled Microbolometers

The effect of thermal parameters G and C on detector performance parameters was discussed in the previous sections. Having a thermal model for G and C is important for design optimization, and can drastically decrease the computation cost, in comparison to finite element analysis. In this section, a comprehensive review of existing thermal models is made.

2.2.1 Thermal Capacitance

The thermal capacitance of a microbolometer is defined as the amount of energy required to increase the area-averaged microplate temperature by 1 K, and can be expressed as

$$C = \frac{\Delta U}{\Delta T} \qquad (J/K), \tag{2.20}$$

where ΔU is the input energy and ΔT is the temperature increase. Thermal capacitance of a lumped mass can be found by using the following formula

$$C = \gamma V, \tag{2.21}$$

where V is the volume and γ is the volumetric heat capacity of the mass, defined as

$$\gamma = c\rho, \tag{2.22}$$

where c is the specific heat capacity and ρ is the density. When Eq. (2.21) is applied for the microbolometer case, the following expression is obtained [40]

$$C = 2\sum_{i=1}^{N} \gamma_i^{arm} V_i^{arm} + \sum_{i=1}^{M} \gamma_i^{mp} V_i^{mp} \quad (J/K). \tag{2.23}$$

where

γ_i^{arm}	volumetric heat capacity of ith layer of each arm;
γ_i^{mp}	specific heat of ith layer of microplate;
V_i^{arm}	volume of ith layer of each arm;
V_i^{mp}	volume of ith layer of microplate;
N	total number of layers in each arm;
M	total number of layers in microplate.

Eq. (2.23) basically adds up the thermal capacitances of all layers forming the microbolometer pixel, and the number two in this equation denotes the number of arms. This method treats the whole microbolometer as a lumped mass. Therefore, it is assumed that the whole microbolometer is at the same temperature, which contradicts the fact that there is a temperature gradient on the arms, as a result of the heat flow to the substrate through them. Therefore, Eq. (2.23) is not a good estimation of C. As an example, Yaradanakul [41] estimated the thermal capacitance of an uncooled YBCO microbolometer using Eq. (2.23), which results in an error as high as 78 %.

Another approach for C estimation is scaling the thermal capacitances of the arm layers by a correction factor of 1/3, which can be stated as

$$C = \frac{2}{3}\sum_{i=1}^{N} \gamma_i^{arm} V_i^{arm} + \sum_{i=1}^{M} \gamma_i^{mp} V_i^{mp}. \tag{2.24}$$

Despite giving better results than Eq. (2.23), Eq. (2.24) is still a rough estimation and it does not depend on the solution of the heat conduction equation.

2.2.2 Thermal Conductance

The thermal conductance of a microbolometer is defined as the amount of power required to increase the area-averaged temperature of the microplate by 1 K. Math-

ematically, this can be expressed as

$$G = \frac{Q}{\theta_{avg}^{SS}} \qquad (W/K), \tag{2.25}$$

where Q is the total generated power and θ_{avg}^{SS} is the area-averaged microplate temperature increase at steady-state, which is given by

$$\theta_{avg}^{SS} = T_{avg}^{SS} - T_s, \tag{2.26}$$

where T_{avg}^{SS} is the area-averaged microplate temperature at steady-state and T_s is the substrate temperature (see Fig. 2.4). Thermal resistance, which is the reciprocal of thermal conductance, is denoted by Z, and can be defined as the area-averaged temperature increase of the microplate as 1 W of heat is supplied to it.

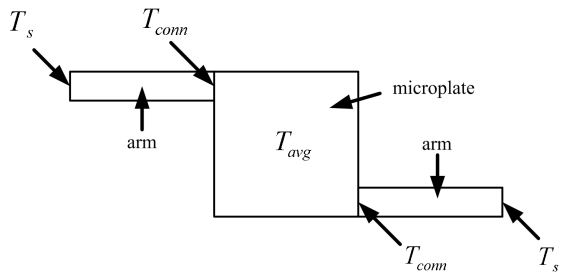

Figure 2.4: Schematic showing the locations of temperatures T_{avg}, T_{conn} and T_s.

The main heat transfer mechanisms involved in the operation of a microbolometer are the convection and radiation between the pixel and its surroundings, and the conduction to the substrate through the arms. For thermal isolation, microbolometers are packaged in vacuum, which means convection can be neglected.

The radiation power P_{rad} emitted from the microplate to the ambient can be expressed as

$$P_{rad} = 2A_{mp}\epsilon_{mp}\sigma\left((T_{avg}^{SS})^4 - T_s^4\right), \tag{2.27}$$

where ϵ_{mp} is the emissivity, σ is the Stefan-Boltzmann constant, A_{mp} is the microplate area and T_s is the ambient temperature. The number two at this equation denotes that both bottom and top surfaces of the microplate emit radiation. In this case, the thermal conductance due to radiation based heat loss (G_{rad}) can be written as

$$G_{rad} = \frac{d\left(2A_{mp}\epsilon\sigma(T_{avg}^{SS})^4 - T_s^4\right)}{dT} = 8A_{mp}\epsilon\sigma(T_{avg}^{SS})^3. \tag{2.28}$$

Radiation based heat losses are mostly negligible; when compared to the thermal conduction through the microbolometer arms [42]. However, when a state-of-art microbolometer having extremely low thermal conductance is considered, the effect of radiation should be taken into account.

The variation of temperature along the thickness (z direction) of the microplate is also neglected. This is due to the fact that the microplate thickness (usually $<1\mu$m) is smaller than the wavelength of the incoming radiation (4 - 12 μm), which results in fairly uniform absorption of radiation by the microplate in z direction. In addition, a part of the infrared radiation propagates through the microplate, and reflects back from the micromirror. Therefore, there is also an inward heat flow from to the microplate from its bottom surface, which also increases the temperature uniformity along the microplate thickness.

The thermal conductance of a typical microbolometer due to the thermal conduction through its arms is estimated by applying Fourier's First Law of Conduction to the arms [15, 43–45]:

$$G = 2\frac{k_{arm}A_{arm}}{L_{arm}}, \tag{2.29}$$

where k_{arm}, A_{arm} and L_{arm} are the thermal conductivity, cross-sectional area and length of the arms, respectively. The microbolometer arms are usually a stack of thin film layers. In this case, the thermal conductance of each thin film layer should be added up. Therefore, Eq. (2.29) can be rewritten as

$$G = 2\sum_{i=1}^{N} k_i \frac{W_i Z_i}{L_i}, \tag{2.30}$$

where W_i, Z_i, L_i and k_i are the width, thickness, length and thermal conductivity of thin film layer i, respectively. Eq. (2.30) assumes that there is no temperature gradient on the microplate; thus it only accounts for the linear temperature drop on the arms. Mathematically, this assumption can be expressed as

$$T_{avg}^{SS} - T_{conn}^{SS} << T_{conn}^{SS} - T_s, \tag{2.31}$$

where T_{conn} is the temperature at the microplate-arm connection at steady-state (see Fig. 2.4). However, it is shown that this assumption can only be valid for sufficiently long arms [15]. As the arms get shorter, the temperature drop within the microplate becomes more effective. To illustrate this, a finite element model of a single layer microbolometer made of polysilicon has been constructed, and

the temperature distribution was found as the arm length is varied. After each simulation, the resulting temperature distribution was postprocessed to find χ, which is defined as the ratio of the temperature drop within the microplate to the temperature drop within the arms.

$$\chi = \frac{T_{avg}^{SS} - T_{conn}^{SS}}{T_{conn} - T_s} \tag{2.32}$$

The results of the simulations are shown in Fig. 2.5. From this figure, it can be concluded that Eq. (2.30) is not valid as the arms get shorter. In addition, since the arms are usually much narrower than the microplate, the radial heat conduction is constricted as heat flows from a wide to narrow cross section, resulting in a constriction thermal resistance, or simply a "constriction resistance" [46]. Therefore, for proper estimation of the thermal conductance, both the heat conduction within the arms as well as within the microplate need to be taken into account [41].

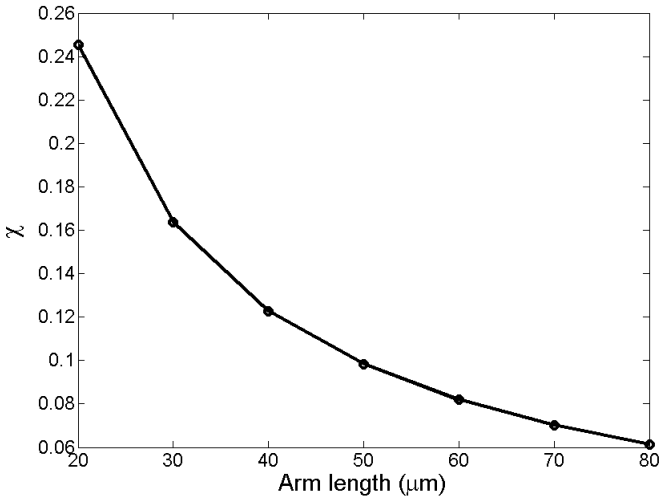

Figure 2.5: The plot of χ as the result of the FEM simulations of a single layer polysilicon microbolometer, as the arm length is varied from 20 μm to 80 μm. The microplate area is $40 \times 40\,\mu\text{m}^2$ and the arm width is 10 μm.

2.3 Microbolometers with Tunable Thermal Conductance

Over the last few years, the attention of microbolometer research focused on increasing the detector's dynamic range, due to the increasing demand on IR detectors for imaging high temperature processes. The dynamic range of a typical microbolometer is not suitable for high temperature process imaging, as the overheating of the microplate due to high scene temperature leads to nonlinear response and device damage. To avoid this problem, the thermal conductance (G) can be made tunable so that it can be increased when a high temperature scene is imaged, and excessive heating of the microplate is avoided. Another advantage is the opportunity to switch between high sensitivity and high frame rate, which is the result of the inverse proportion between the thermal conductance and thermal time constant (recall Eq. (2.5)).

This section starts with a comprehensive introduction to tunable thermal conductance (tunable G) microbolometers and the motivations behind the concept (Section 2.3.1). Existing tunable G microbolometers are reviewed (Section 2.3.2), and the design and fabrication details of a new and improved tunable G mechanism are proposed at the end (Section 2.3.3).

2.3.1 Background

The sensitivity of microbolometric IR detectors have increased significantly over the last few decades. This increase is mainly due to the advances in microfabrication technology, which has enabled the fabrication of microbolometers with very low thermal conductance. After the introduction of double layer microbolometer structures [1, 5, 35], the thermal conductance of state-of-art microbolometers has been reduced to values as low as 5×10^{-8} W/K [1].

High thermal isolation makes the microbolometer extremely receptive to small differences in the scene temperature. However, high sensitivity can lead to overheating of the microplate when a very high temperature scene is being imaged, for example, a fire or explosion.

To see the effect of a high temperature object on the microplate, the temperature

change induced on the microplate by a change in the temperature of the target object should be calculated first. Fig. 2.6 shows the collection optics of an IR camera. The target temperature and the microplate temperature are denoted by T_T and T_{mp}, respectively. It is assumed that the lens, which is circular and perfectly transparent, subtends a solid angle Ω with semicone angle θ_s at the microplate. The number of optics (F-number) of this optical arrangement can be defined as [24]

$$F_{no} = \frac{1}{2\sin\theta_s}. \tag{2.33}$$

The IR radiation power incident on a microplate is given by [24]

$$P_{in} = \pi L_T A_{mp} \sin^2\theta_s = \frac{\pi L_T A_{mp}}{4F_{no}^2}, \tag{2.34}$$

where L_T is the radiance (emitted power per unit area per solid angle) of the target, and A_{mp} is the microplate area. Given the coupling efficiency η, the absorbed power P_{abs} by the microplate is

$$P_{abs} = \eta P_{in} = \frac{\pi\eta L_T A_{mp}}{4F_{no}^2}. \tag{2.35}$$

Assuming that the target is a blackbody, the radiance L_T of the target is given by [47]

$$L_T = 2hc^2 \int_{\lambda_1}^{\lambda_2} \frac{d\lambda}{\lambda^5 \left(\exp\left(hc/k_B T_T \lambda\right) - 1\right)}, \tag{2.36}$$

where λ_1 and λ_2 are the lower and upper values of the wavelength, h is Planck's constant, c is the speed of light and k_B is the Boltzmann constant. The ratio of the temperature increase at the microplate to the temperature increase at the target is found as

$$\frac{\partial T_{mp}}{\partial T_T} = \frac{\partial T_{mp}}{\partial P_{abs}} \frac{\partial P_{abs}}{\partial T_T} = \frac{\partial T_{mp}}{\partial P_{abs}} \frac{\pi\eta A_{mp}}{4F_{no}^2} \left(\frac{\partial L_T}{\partial T_T}\right), \tag{2.37}$$

where $\partial T_{mp}/\partial P_{abs}$ is equal to the thermal resistance (i.e. the inverse of thermal conductance G). Therefore, we obtain

$$\frac{\partial T_{mp}}{\partial T_T} = \frac{\pi\eta A_{mp}}{4GF_{no}^2} \left(\frac{\partial L_T}{\partial T_T}\right), \tag{2.38}$$

where $\partial L_T/\partial T_T$ can be found by differentiating Eq. (2.36) with respect to T_T.

As an example, $\partial T_{mp}/\partial T_T$ is calculated for the state-of-art microbolometer in [1], whose parameters are tabulated in Table 2.1. Assuming the initial values $T_T = T_{mp} = 300\,K$, it can be calculated that if the target temperature increases to 400 K

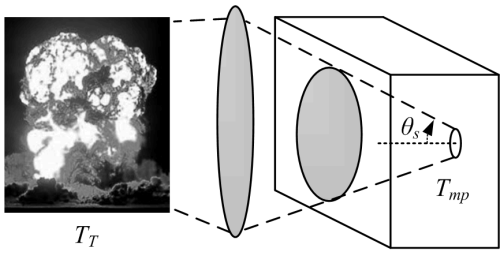

Figure 2.6: The collection optics of the IR detector camera. The microplate temperature is T_{mp}, the target temperature is T_T and the semicone angle is θ.

Table 2.1: Parameters for the microbolometer in [1].

Parameter	Value
Microplate area	$25\,\mu$m $\times$ $25\,\mu$m
η	0.8
Spectral range	8 - 14 μm
G	5×10^{-8} W/K
F_{no}	1

($\Delta T_T = 100\,K$), the microplate temperature increases to $\sim 301\,K$, which will not affect the proper operation of the microplate. On the other hand if an explosion of temperature $T_T = 3000\,K$ is imaged, then the microplate temperature increases to $\sim 391\,K$. The dynamic range of the microbolometer in [1] is limited to 233 K to 333 K. Therefore, the microplate temperature of 391 K is out of the dynamic range, and can adversely affect the microbolometer operation, such as

- temporary afterimage and blindness
- image non-uniformity, distortion, etc
- delamination and plastic deformation of arms
- device failure

These effects can be attributed to several different factors. One of these is the substantial change in the material properties of the thin film layers forming the microplate. For instance, vanadium oxide (VO_x), which is the most common IR sensitive material, shows a huge change in its absorption and resistivity properties when its temperature is above 68°C [23]. This behavior of VO_x can be clearly seen

in Figure 2.7. When a fire or explosion is imaged with the IR detector in [1], these adverse effects are quite likely to occur.

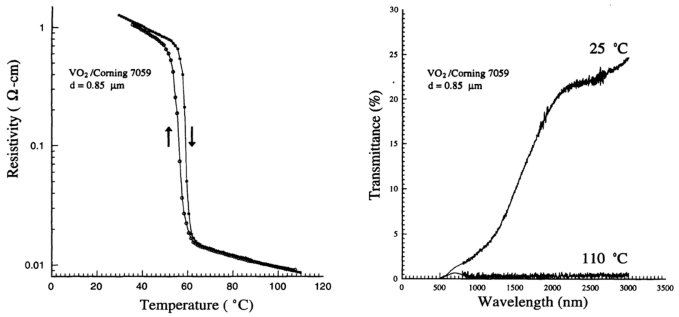

Figure 2.7: The electrical and optical properties of VO_2 films deposited on Corning 7059 glass substrates at 450°C. Reprinted from [23].

Temporary afterimage is an important problem as well, since it can cause misinterpretations when comparing the temperatures of two different targets. This effect is shown in Fig. 2.8. Let us assume a two-pixel array, where pixel 1 images target 1, and pixel 2 images target 2. The temperature of target 1 and target 2 (T_{T1} and T_{T2}) with respect to time are plotted in Fig. 2.8(a), and the corresponding microplate temperatures of pixel 1 and pixel 2 (T_{mp1} and T_{mp2}) are plotted in Fig. 2.8(b). As can be seen from the microplate temperatures, even after the temperature of target 1 decreases to 300 K, the corresponding microplate temperature does not decrease to 300 K, for a long time. Therefore, the pixel temperature at time t leads the user to the wrong conclusion that target 1 is hotter than target 2. This error is more common in microbolometers with a larger thermal time constant.

Excessive temperature at the microplate can also lead to mechanical damage of the device, such as delamination and plastic deformation of the microbolometer arms, or device failure due to overheating. In addition, the thermal expansion of the arms can result in substantial bending of the microplate, which degrades the planarity of the microplate.

All the hurdles explained above can be solved if the thermal conductance G of the microbolometer is increased sufficiently, when a high temperature scene is imaged. That way, the overheating of the microplate can be prevented, and safe imaging of high temperature scenes will be possible. For instance, if the thermal

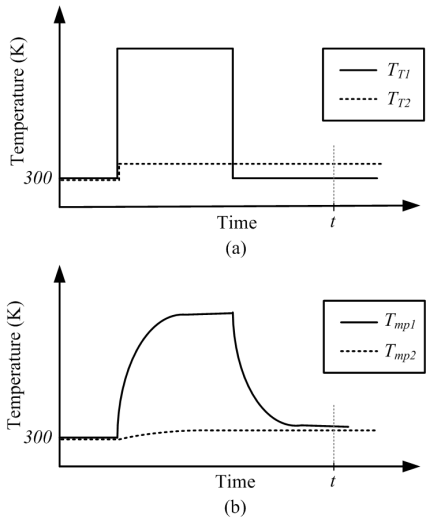

Figure 2.8: The plot showing the temperature of (a) target 1 and target 2, and (b) pixel 1 and pixel 2, with respect to time.

conductance G of the microbolometer in [1] (recall Table 2.1) was to be increased from 5×10^{-8} W/K to 5×10^{-7} W/K when a 3000 K target is imaged, the microplate temperature will increase to a safe value of 309 K instead of 391 K.

In addition to providing an efficient solution to imaging high temperature scenes, tuning the thermal conductance gives the user the opportunity to switch between high sensitivity and high video frame rate. As previously stated by Eq. (2.5), increasing the thermal conductance results in a lower thermal time constant, meaning a higher frame rate. Therefore, if the sensitivity is of primary importance, the thermal conductance can be tuned to its lowest value. Likewise, if the frame rate is the primary concern, the thermal conductance can be increased so that the frame rate is increased with a trade-off in sensitivity.

2.3.2 Review of Microbolometers with Tunable Thermal Conductance

A microbolometer with adjustable thermal conductance was first proposed by Leonov and Butler in 2001 [48]. The proposed design is shown schematically in Fig. 2.9. The idea of this design was to tune the gap between the microbolometer and the micromirror, to achieve a multicolor IR image. In addition, a thermally conducting cantilever beam, called a "thermal microchopper" was designed to contact the de-

tector pixel immediately after each readout process, in order to maintain the same video frame rate while multicolor imaging is realized. Therefore, there were basically two actuator types in this design: a moving micromirror to tune the spectral response, and a thermal microchopper to cool down the microplate to maintain high frame rate operation. Among many actuation mechanisms, electrostatic actuation was chosen due to its fast response, easy fabrication and low power consumption. The calculated actuation voltage for the thermal microchopper was very low (0.2 V), however this complex device was not fabricated. In addition, the excessive heating problem due to imaging of hot regions was not addressed.

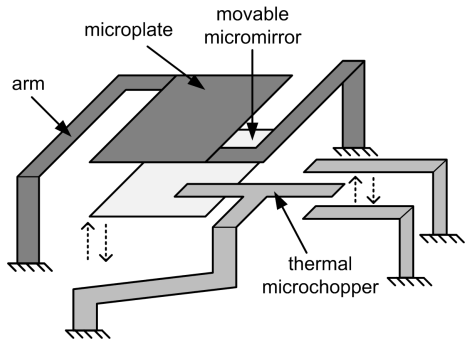

Figure 2.9: The thermal microchopper mechanism for a two-color microbolometer, proposed in [48]

.

The idea of tunable thermal conductance for simultaneous imaging of hot and cold regions was first proposed by Song et al in 2002 [4]. They fabricated a simple and effective system, where the microplate and the arms are attracted to the substrate by the application of an actuation voltage (V_{act}) (see Fig. 2.10). In 2006, they improved the design and increased the fill-factor of the device by locating zigzagged arms below the microplate [5]; however the actuation mechanism was still based on using the substrate as the actuation electrode. The shape of the improved design is depicted in Fig. 2.11.

Applying voltage to the substrate leads to the actuation of the whole microbolometer array, which is not desirable. Pixel-by-pixel actuation, which is necessary when both hot and cold regions are imaged with the same focal planar array, is not possible if the actuation voltage is applied to the substrate. Another disadvantage is the high electric field induced on the die, which may affect the proper operation of the electronics associated with the microbolometer array.

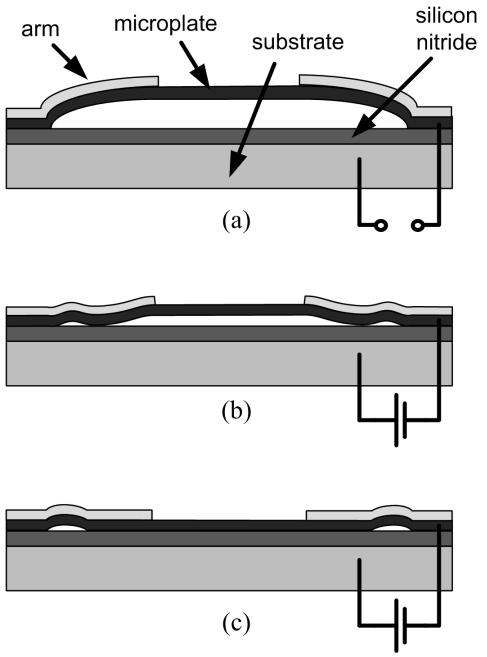

Figure 2.10: The thermal conductance tuning mechanism proposed in [4]

In order to avoid the disadvantages of substrate actuation, the micromirror can be actuated. The micromirror is electrically isolated from the substrate by an insulator layer, which is deposited to electrically isolate the substrate from the surface structures and electronics. The micromirror can be employed for actuating the microplate without affecting the substrate. Furthermore, the location of the micromirror, which is below the microplate, makes it very suitable to be used for actuating the microplate. A potential problem of applying voltage to the micromirror however, is how to prevent electrical contact between the microbolometer and the micromirror when the microbolometer snaps onto the micromirror as pull-in voltage is exceeded. This problem is not present when the bottom layer of the microplate is an insulator, such as the silicon nitride layer in [5] that is used as a structural layer to support the microplate. However, if there is no insulator layer under the IR sensitive film through which the bias current passes, the actuation terminals will electrically short as the microplate contacts the micromirror, which in turn will lead to device failure due to high current (An example of microbolometers with an unsupported IR sensitive layer is studied in [3]). In this case, an insulator layer can be deposited on the micromirror to prevent the micromirror-microplate contact.

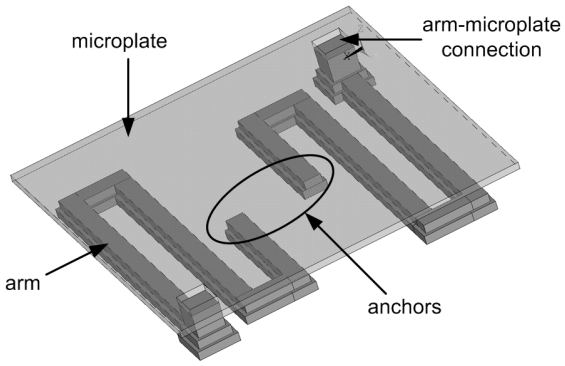

Figure 2.11: The shape of the tunable thermal conductance mechanism, presented in [5].

Another important point to consider is that the actuation of the microplate may result either in continuous or discrete tuning of thermal conductance. Discrete tuning means a sharp and considerable change in thermal conductance, whereas continuous tuning means a more linear relationship between the actuation voltage and thermal conductance. Continuous tuning adds more functionality to the tunability of thermal conductance. It allows fine tuning of the thermal conductance to the desired value, which can be precisely determined by the pixel temperature or the user adjusted video frame rate. Therefore, continuous tuning is preferable to discrete tuning. For the microbolometer shown in Fig. 2.10(b), the microbolometer arms snap down at a lower voltage than the detector plate, allowing a continuous thermal conductance tuning. This is achieved by the curved bilayer microbolometer arms due to the residual stress. Therefore, this tuning mechanism puts an important requirement on the microbolometer design: bilayer arms. In addition, if a micromirror is used as the actuation terminal instead of the substrate, the arms may not snap-down before the microplate, since the micromirror area is too small to enclose the arms. The bilayer arms structure shown in Fig. 2.10 is also used by Song et al [5], however, as can be seen in Fig. 2.11, the arms are located below the microplate, resulting in a double layer structure. In this case, thermal conductance can be tuned continuously if a micromirror is used instead of the substrate for actuation. However, placing the arms between the microplate and the micromirror will partly block the IR radiation that propagates through the air gap, resulting in less infrared absorption.

Another potential problem of all of the mechanisms explained above is the in-

use stiction, which refers to the stiction of the microbolometer to the base plate even after the actuation voltage is removed. In-use stiction occurs when the stiction force is greater than the restoring force, which is the mechanical force that tries to separate the microplate from the base plate and restore it to its original position. The stiction force depends on many factors, and a significant one is the contact area. In the structures introduced above, the whole microplate snaps onto the substrate at pull-in, resulting in a large contact area. In-use stiction was observed in the device in Fig. 2.11 at full snap-down of the microbolometer [5].

2.3.3 Proposed Design and Fabrication

In this section, a new mechanism that avoids the problems addressed in the previous section is proposed. This mechanism, which in thesis is called "the stopper mechanism", is illustrated in Fig. 2.12. The stoppers are rigid structures anchored to the substrate, and they extend partly into the gap between the microplate and the micromirror. Their purpose is similar to the "stand-off" mechanisms [49, 50], which are used to prevent stiction and to limit the actuation range of the micromirrors and other electrostatic microdevices. As the microplate deflects towards the biased micromirror, the stoppers prevent it from deflecting any further, thus avoiding contact with the micromirror (see Fig. 2.12(b)). At the same time, the thermal conductance will increase, since the heat will flow to the substrate is mainly through the stoppers, which provide a good heat link between the microbolometer and the substrate. This state is called the actuated state or "contact state". When the bias voltage is decreased to zero volts, the microplate will revert back to its original position, thus eliminating the heat link provided by the stoppers (Fig. 2.12(a)). In that case, thermal conductance will decrease back to its lowest value, which is then limited by heat conduction through the long microbolometer arms. This state is called the unactuated state.

To demonstrate this mechanism, several test structures were fabricated using PolyMUMPs (Polysilicon Multi-User MEMS Process) run 82 [2]. PolyMUMPs is a surface micromachining technology, composed of three polysilicon (Poly 0, Poly 1 and Poly 2) layers, two sacrificial (Oxide 1 and Oxide 2) layers and one metal (gold) layer on an insulating silicon nitride layer. The nominal thicknesses of these layers are shown in Table 2.2. PolyMUMPs was chosen for fabrication, due to

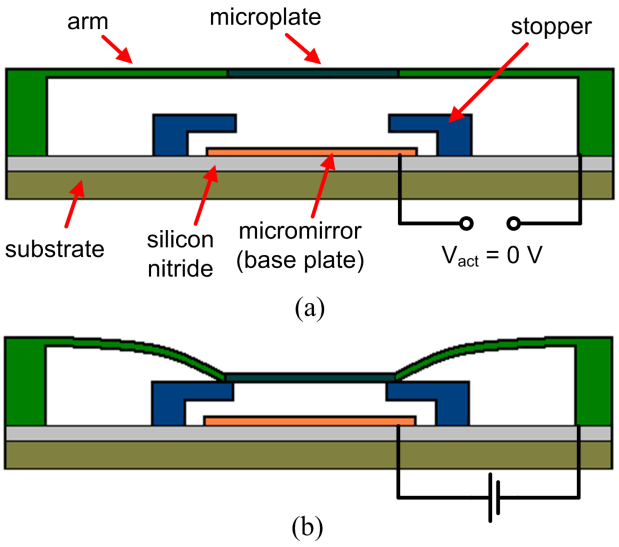

Figure 2.12: Cross-sectional schematic of the microbolometer with the stopper mechanism, in the (a) unactuated state and (b) actuated state (contact state). Not drawn to scale.

its reliability and well-defined process flow. The capabilities of the PolyMUMPs process are enough to demonstrate the G tuning mechanism and the microbolometer model. However, for fabrication of a real microbolometer pixel, a custom fabrication process and a larger variety of materials are required, to build a metallic micromirror below the microplate and to use a high TCR material for the active layer.

Among the various shapes and geometries studied for this work, two final designs are analyzed in this dissertation: *design T80* and *design T120*. The mask design of design T80 and T120 are shown in Fig. 2.13, and the dimensions of both designs

Table 2.2: Thicknesses of the material layers used in the PolyMUMPs Process [2].

Layer Name	Thickness (μm)
Silicon nitride	0.6
Poly 0	0.5
Oxide 1	2.0
Poly 1	2.0
Oxide 2	0.75
Poly 2	1.5
Metal	0.5

Table 2.3: The dimensions of design T80 and T120.

	design T80	design T120
Microplate side length (μm)	80	120
Arm width, polysilicon (μm)	10	10
Arm width, gold (μm)	4	4
Arm length, total (μm)	180	160
Arm length, 1^{st} piece (μm)	37	-
Arm length, 2^{nd} piece (μm)	143	-
Gap thickness[1] (μm)	2.75	2.75

are tabulated in Table 2.3. Both are test structures fabricated to show the tunable thermal conductance mechanism, and primarily differ in dimensions, such as the microplate size and the arm length. As can be seen from Fig. 2.13 and Table 2.3, in design T80, each arm is fabricated as two straight lines, joined perpendicularly to each other. The lengths of these two arm pieces are 43 μm and 137 μm, which gives a total arm length of 180 μm. In design T120, each arm is a straight line 160 μm long. The microplate side lengths are also different in these devices. The microplate side length of design T80 and design T120 are 80 μm and 120 μm, respectively. The gap between the base plate and the microplate is 2.75 μm for both designs, and the stoppers are located 750 nm below the microplate.

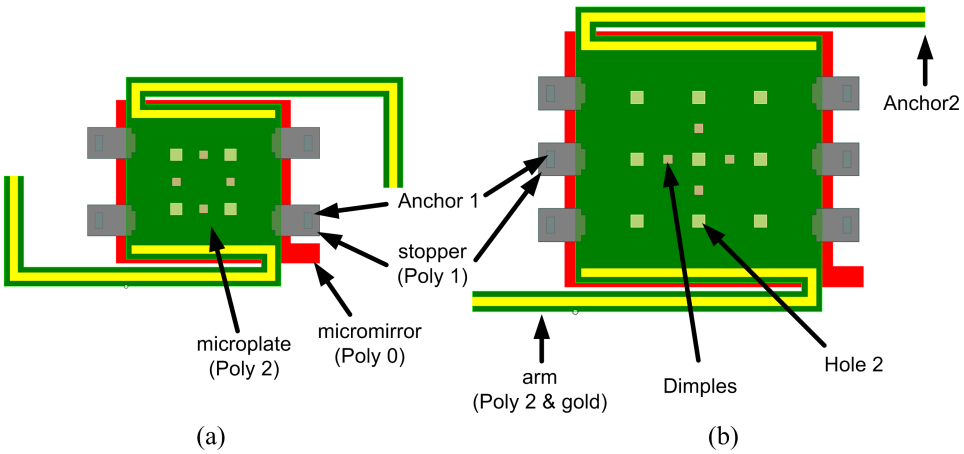

Figure 2.13: Schematic showing the mask design of (a) design T80 (b) design T120.

[1]This gap thickness is equal to the total oxide layer thickness (see Table 2.2). However, the gap thickness of the fabricated structures is different than the nominal value of 2.75 μm. The actual gap thickness is determined using the optical profiling method, which is explained in Section 4.1.

The process flow for the test devices fabricated in PolyMUMPs is shown schematically in Fig. 2.14. The process begins with an n-type (100) silicon wafer of 1-2 Ωcm resistivity. First, a 600 nm low-stress LPCVD (low pressure chemical vapor deposition) silicon nitride layer is deposited on top of the silicon wafer (Fig. 2.14(a)). This layer serves as an electrical isolation layer. Following the deposition of silicon nitride, a 500 nm LPCVD polysilicon layer (Poly 0) is deposited. Poly 0 is patterned by photolithography, a process including coating the wafer with photoresist, exposure of the photoresist with the appropriate mask, and developing the exposed photoresist for patterning. After patterning, Poly 0 is etched in an RIE (Reactive Ion Etch) system. In our design, the Poly 0 layer is used as the micromirror, and the base layer of electrical connection lines and pads. It should be noted that in an actual microbolometer, the micromirror is metallic. However, for the test structures, the Poly 0 layer is used as the base plate of the electrostatic actuator instead of a metallic layer, due to the limitations of the PolyMUMPs process. Nevertheless, this situation is not expected to affect the experimental results, since the micromirror material has no effect on electrostatic actuation. The side view after the pattern and etch of Poly 0 is shown schematically in Fig. 2.14(b).

A 2.0 μm phosphosilicate glass (PSG) is then deposited by LPCVD and annealed at 1050°C for one hour in Argon. This layer, known as Oxide 1 (or the First Oxide), is the first sacrificial layer. Oxide 1 is patterned twice. The first patterning is done with the dimple mask, which has a nominal depth of 750 nm. Four $4\,\mu\text{m} \times 4\,\mu\text{m}$ squares are patterned with the DIMPLE mask to reduce the risk of stiction upon release. The second mask used is the ANCHOR1 mask. This mask provides anchor holes (Fig. 2.14(c)), which will be filled with Poly 1.

After etching Anchor 1, the first structural layer of polysilicon (Poly 1) is deposited with a thickness of 2.0 μm. This layer is then patterned and etched, to form the stoppers (Fig. 2.14(d)). Patterning of the Poly 1 layer starts with the deposition of a 200 nm layer of PSG over Poly 1. Following the deposition of PSG, the wafer is annealed at 1050°C for 1 hour, in order to facilitate the diffusion of phosphorus from PSG to polysilicon, and to reduce the stress in the Poly 1 layer. After the anneal, the PSG layer is patterned and etched to produce a hard mask for the Poly 1 etch.

Following the Poly 1 etch, a second sacrificial PSG layer (Oxide 2 or Second Oxide) is deposited and annealed. Oxide 2 is patterned and etched using the

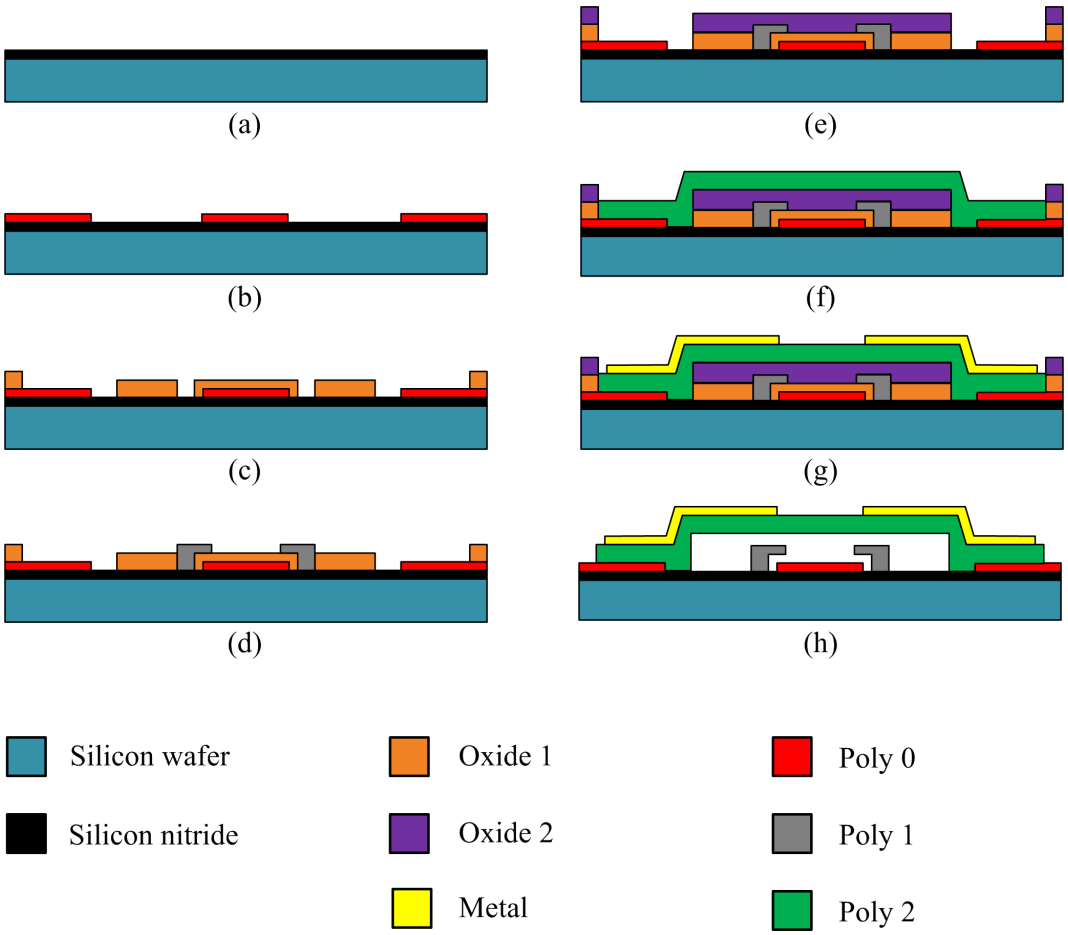

Figure 2.14: PolyMUMPs process flow for the test devices.

ANCHOR2 mask, to form the anchor of the arms. A second mask, known as the POLY1POLY2VIA mask, is also used for patterning Oxide 2 in the PolyMUMPs process. This mask is used to etch Oxide 2 down to the Poly 1 layer, in order to provide a connection between Poly 1 and Poly 2. Since there is no connection between Poly 1 (stoppers) and Poly 2 (the microplate and the arms) in our design, the POLY1POLY2VIA mask is not used. The side view after patterning and etching Oxide 2 is shown in Fig. 2.14(e). The second structural layer of polysilicon (Poly 2) is then deposited, patterned and etched to form the microplate and the arms (Fig. 2.14(f)). Similar to the patterning of Poly 1, a 200 nm PSG layer is used as a dopant source and etch mask for the Poly 2 layer. The patterning of Poly 2 also includes forming the etch holes using the HOLE2 mask, which reduces the stiction during the final release of the structure. Four $7\,\mu\text{m} \times 7\,\mu\text{m}$ holes are etched in design T80 and nine $7\,\mu\text{m} \times 7\,\mu\text{m}$ holes are etched in design T120.

The final deposited layer is a 0.5 μm thick gold layer. This layer, also known as the metal layer, is patterned to form the electrical connections, the gold coatings at the arms and the electrodes at the microplate. Coating the arms with gold decreases the electrical resistance of the arms. This way, the resistive heating takes place mainly on the microplate. To stay within the PolyMUMPs design rules, the Poly 2 layer should enclose the gold layer by at least 3 μm. Hence, the width of the gold layer at the arm is made 6 μm narrower than the polysilicon width at the arm (see Table 2.3). The two gold lines located close to the two edges of the microplate are used as electrodes. They increase the uniformity of the electrical current, resulting in more uniform resistive heating within the microplate. The effect of the electrodes can be observed from the finite element simulation results plotted in Fig. 2.15. After all the deposition steps are finished (Fig. 2.14(g)), the

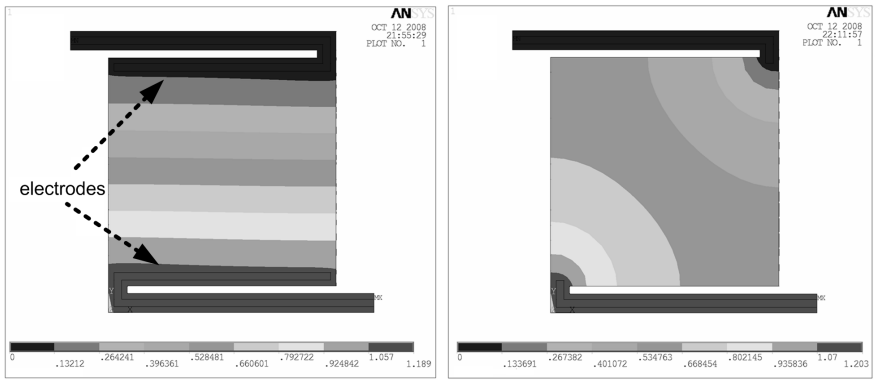

(a) (b)

Figure 2.15: Simulation results showing the voltage distribution of the design T120 microbolometer (a) with and (b) without the metal electrodes on the microplate.

sacrificial layer release is performed, which starts with immersing the chip in 49% HF solution at room temperature, followed by deionized (DI) water and alcohol for a few minutes and CO_2 drying. Finally, the chip is heated in an oven at 110°C at least for ten minutes. The side view of the chip after release is shown in Fig. 2.14(h), and the Scanning Electron Micrograph (SEM) image of the fabricated devices is shown in Fig. 2.16.

In this chapter, the general microbolometer theory was given and the concept of tunable thermal conductance was investigated. A novel pixel-by pixel thermal conductance mechanism was presented, and its design and fabrication process details were explained. In the next chapter, a complete microbolometer model is devel-

oped, which includes an infrared absorption model, an improved thermal model for the unactuated and the actuated state, and an electrostatic-structural model for the G tuning mechanism.

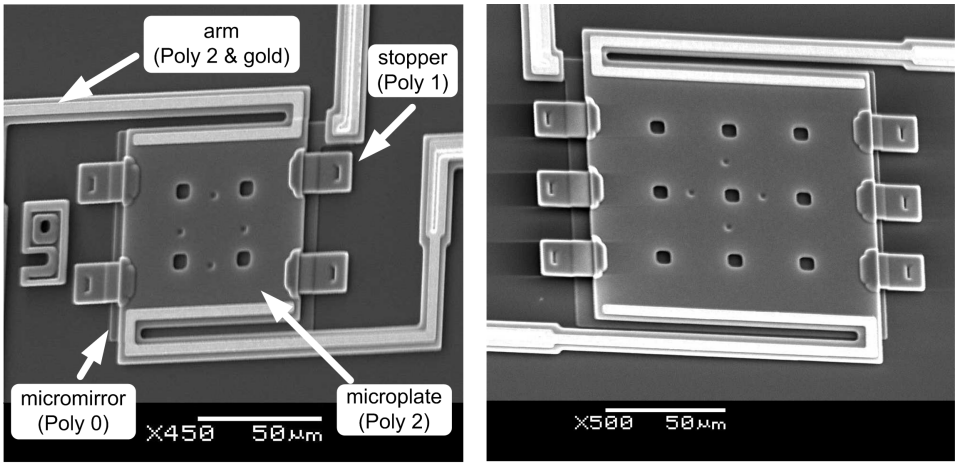

Figure 2.16: The SEM images of the two test structures ((a) design T80 and (b) design T120) analyzed in this work.

Chapter 3

Modeling of Microbolometers with Tunable Thermal Conductance

The tunable thermal conductance (tunable G) microbolometer is a device in which energy is converted from one form to another. The electromagnetic energy is partly converted to thermal energy within the microplate, and the thermal energy is converted to a change in the electrical energy of the readout signal. In addition, when the microplate is actuated with an actuation voltage, the electrical energy is converted into mechanical energy by electrostatic actuation.

The basic microbolometer analytical models are not comprehensive, and can lead to errors, especially in the calculation of the thermal parameters. In addition, these models cannot be directly applied to the tunable-G microbolometers. Therefore, an analytical model is necessary for early design and optimization stages of a tunable G microbolometer. Compared to a finite element model (FEM), an analytical model can drastically reduce the computation time. It also provides the opportunity to determine the coupling between the input parameters and design variables, such as the effect of actuation voltage on thermal conductance, or the coupling between the gap thickness and the spectral absorption. In addition, the design parameters can be optimized according to the performance requirements, with the help of the analytical model.

In this chapter, a comprehensive approximate analytical model for the test

structures is presented, which forms a basis for analytical modeling of tunable G microbolometers. The model is divided into three parts. The first part is the electrostatic-structural model (Section 3.1), which determines the stiffness of the structure, and uses basic movable plate capacitor theory to calculate the contact voltage, i.e. the voltage where the microplate contacts the stoppers. The second part is the infrared absorption model (Section 3.2), which uses electromagnetic wave theory to determine the electromagnetic energy absorbed in any layer, and calculates the coupling efficiency η accordingly. The third part is the thermal model, which calculates the thermal parameters in the unactuated state (Section 3.3) and the actuated state (Section 3.4). In the unactuated state, the temperature variation on the microplate and the constriction resistance as heat flows from the microplate to the arms, are taken into account, whereas in the actuation state, the thermal contact conductance between the microplate and the stoppers is calculated in terms of the actuation voltage, by employing a conforming rough surface thermal contact model. In addition, for each model, a FEM is constructed using commercial finite element analysis software, to verify the applicability of the model. The details of the finite element models are given in Section 3.5.

3.1 Electrostatic-Structural Model

In a microbolometer with tunable thermal conductance, an actuation voltage (V_{act}) is applied between the microplate and the base plate, to move the microplate towards the base plate by electrostatic actuation. The aim of the electrostatic-structural model is to find the displacement of the microplate as a function of V_{act}, and to find the contact voltage.

The electrostatic-structural model starts with the calculation of the bending stiffness of the cross-section (or simply section) of a microbolometer arm (Section 3.1.1). Since design T80 and T120 have identical sections, the calculations in Section 3.1.1 are the same for both designs. In Section 3.1.2, the equivalent spring constant k_{eq} of the arms is calculated, which is then used in the calculation of the contact voltage that is explained in Section 3.1.3. The results of the model are verified with finite element model (FEM) simulations and experiments in Chapter 4.

3.1.1 Bending Stiffness of the Arm Section

To find the spring constant of an arm, the bending stiffness of its section should be determined first. The section of an arm of a test structure is shown in Fig. 3.1(a). The upper section is gold, having the width W_{gold}, thickness Z_{gold}, Young's Modulus E_{gold} and Poisson's ratio ν_{gold}. The lower section is Poly 2, having the width W_{Poly2}, thickness Z_{Poly2}, Young's Modulus E_{PolySi} and Poisson's ratio ν_{PolySi}. Since the section is composite, the equivalent bending stiffness should be determined to make the beam bending analysis. A simple way to determine the equivalent stiffness of a composite section is to apply the transformed section method [51]. In this method, the composite section is reduced to a section of single material with identical bending stiffness and Young's modulus. The gold region is transformed by scaling its width with the ratio of Young's modulus of the two materials, which is given by

$$W'_{gold} = W_{gold}\frac{E_{gold}}{E_{Poly2}} \tag{3.1}$$

The thicknesses of the gold and Poly 2 regions (Z_{gold} and Z_{Poly2}) remain constant, in order to preserve the strain distribution. The resulting geometry after the transformation is composed of two rectangular sections of the same material (polysilicon), as shown in Fig. 3.1(b).

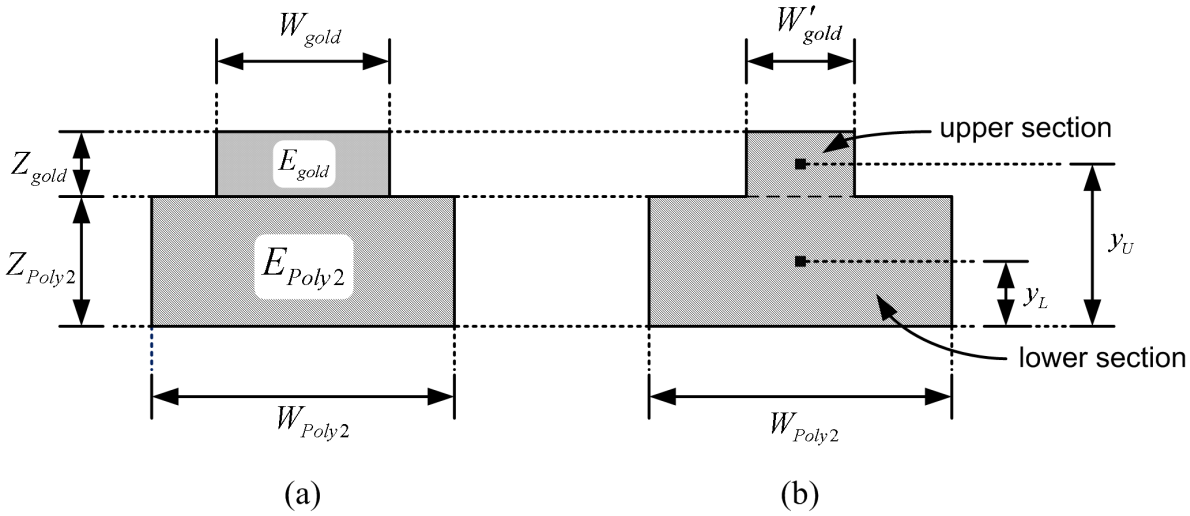

Figure 3.1: Schematic showing the application of the transformed section method to the arm section: (a) the section before the transformation and (b) after the transformation.

The area moment of inertia of the modified section can de determined by implementing the parallel axis theorem [51], which is shown schematically in Fig. 3.2. The parallel axis theorem states that the area moment of inertia of an object about an axis z parallel to the axis through the center of mass is given by

$$I_z = I_{cm} + Ad^2 \tag{3.2}$$

where

I_z	the area moment of inertia (I) of the object about axis z;
I_{cm}	the I of the object about the axis through the center of mass;
A	the area of the section;
d	the perpendicular distance between the two axes.

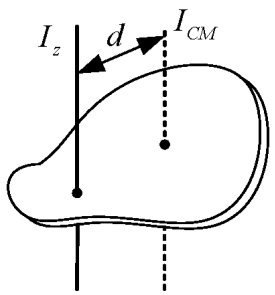

Figure 3.2: Schematic showing the parallel axis theorem.

Since the arm layers are assumed to be homogenous, the centroid locations can be used instead of the center of mass locations. The centroid location y_c of the transformed section can be determined by

$$y_c = \frac{A_L y_L + A_U y_U}{A_L + A_U} \tag{3.3}$$

where A_L and y_L are the area and the location of the centroid of the lower section, and A_U and y_U are the area and the location of the centroid of the upper section (refer to Fig. 3.1(b)). The areas A_L and A_U are given by

$$A_L = W_{Poly2} Z_{Poly2} \tag{3.4}$$

$$A_U = W'_{gold} Z_{gold} \tag{3.5}$$

and the locations of the centroids are given by

$$y_L = \frac{Z_{Poly2}}{2} \tag{3.6}$$

$$y_U = Z_{Poly2} + \frac{Z_{gold}}{2} \tag{3.7}$$

Once y_c is found from Eq. (3.3), the area moment of inertia of the composite region, I_{comp} can be found by applying Eq. (3.2), the parallel axis theorem.

$$I_{comp} = I_L + I_U + A_L \left(y_c - y_L\right)^2 + A_U \left(y_c - y_U\right)^2, \tag{3.8}$$

where I_L and I_U are the area moment of inertias of the rectangular sections, given by

$$I_L = \frac{1}{12} W_{Poly2} Z_{Poly2}^3 \tag{3.9}$$

$$I_U = \frac{1}{12} W'_{gold} Z_{gold}^3 \tag{3.10}$$

Once I_{comp} is found from Eq. (3.8), the bending stiffness $E_{Poly2} I_{comp}$ can be calculated. The next step of the model is to find the equivalent spring constants of the arms, which is explained next.

3.1.2 Equivalent Spring Constant of the Test Structures

In this section, the equivalent spring constant of designs T80 and T120 is calculated, based on the elastic beam theory. The calculation for design T120 is explained first, due to its simpler geometry (to compare the geometries of design T80 and T120, the reader may refer to Fig. 2.13).

Design T120

An arm of design T120 is shown schematically in Fig. 3.3(a). As can be seen from the mask design shown in Fig. 2.13, each arm of design T120 has two segments, but the segment that connects the arm to the plate is very short (4 μm), in comparison to the total arm length (160 μm). Therefore, it can be assumed that each T120 arm consists of one straight beam. In addition, it was assumed that the microplate is totally flat, and it moves down to the base plate without any change in its flatness. Based on this assumption, the right end of the beam, which is the arm-microplate connection, should be horizontal. Therefore, the right end of the beam is assumed to be guided, as can be seen in Fig. 3.3(a). A point load P is applied from this guided end. The left end, which is anchored to the substrate is considered as the fixed end. The reaction moments of the fixed and guided end are M_f and M_g.

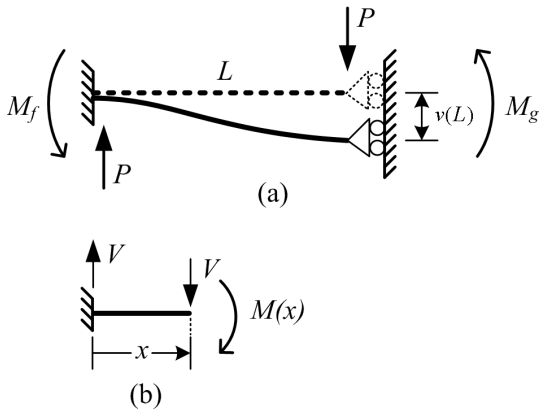

Figure 3.3: The equivalent elastic beam representation of one arm of design T120: (a) the whole beam (b) a portion of length x

Defining $v = f(x)$ the elastic curve function of the beam, the following differential equation is valid for an elastic beam [51]

$$\frac{\partial^2 v/\partial x^2}{\left[1 + (\partial^2 v/\partial x^2)^2\right]^{3/2}} = \frac{M(x)}{EI}, \tag{3.11}$$

where $M(x)$ is the internal moment in the beam at the point x and EI is the bending stiffness of the beam. Assuming $(\partial^2 v/\partial x^2)^2$ is negligible compared to unity, Eq. (3.11) can now be rewritten as

$$\frac{\partial^2 v}{\partial x^2} = \frac{M(x)}{EI}. \tag{3.12}$$

The free body diagram of a beam portion of length x is shown in Fig. 3.3(b). The internal moment at point x ($M(x)$) is equal to the difference of moment due to load P ($P(L-x)$) and M_g. Therefore, Eq. (3.12) becomes

$$EI\frac{\partial^2 v}{\partial x^2} = M_g - P(L-x). \tag{3.13}$$

Integrating Eq. (3.13), we reach

$$EI\frac{\partial v}{\partial x} = (M_g - PL)x + \frac{Px^2}{2} + C_1, \tag{3.14}$$

and if Eq. (3.14) is integrated further, the following expression is obtained:

$$EIv(x) = \frac{(M_g - PL)x^2}{2} + \frac{Px^3}{6} + C_1 x + C_2. \tag{3.15}$$

In order to solve Eq. (3.15), the unknowns C_1, C_2 and M_g need to be determined by employing the boundary conditions. The left end ($x = 0$) of the beam is the anchor point, hence it has zero displacement and slope, leading to the following two boundary conditions.

$$v(0) = 0 \tag{3.16}$$

$$\left.\frac{\partial v}{\partial x}\right|_{x=0} = 0 \tag{3.17}$$

The guided end ($x = L$) should have zero slope, leading to

$$\left.\frac{\partial v}{\partial x}\right|_{x=L} = 0. \tag{3.18}$$

Using Eq. (3.17) and Eq. (3.18) in Eq. (3.14) gives

$$M_g = \frac{PL}{2} \tag{3.19}$$

$$C_1 = 0. \tag{3.20}$$

Using Eq. (3.16) in Eq. (3.15) gives

$$C_2 = 0. \tag{3.21}$$

Finally, substituting C_1, C_2 and M_g in Eq. (3.15) with their values, we reach

$$EIv(x) = \frac{Px^3}{6} - \frac{PLx^2}{4}. \tag{3.22}$$

Using $x = L$ in the above equation, the displacement of the guided end can be found as

$$v(L) = -\frac{PL^3}{12EI}. \tag{3.23}$$

If the bending stiffness EI in Eq. (3.23) is replaced with $E_{Poly2}I_{comp}$, which is the bending stiffness of the composite section, the displacement of the guided end can be rewritten as

$$v(L) = -\frac{PL^3}{12E_{Poly2}I_{comp}}. \tag{3.24}$$

The spring constant of the arm is found by dividing the external load P by the displacement ($v(L)$), giving

$$k = -\frac{P}{v(L)} = \frac{12E_{Poly2}I_{comp}}{L^3}. \tag{3.25}$$

Finally, since the microplate is supported by two arms, the equivalent spring constant of design T120 is found by multiplying the spring constant of one arm by two, which yields

$$k_{eq} = \frac{24E_{Poly2}I_{comp}}{L^3}. \tag{3.26}$$

Design T80

The top view of a design T80 arm is shown schematically in Fig. 3.4. Similar to design T120, the 4 μm segment that connects the arm to the microplate is neglected. Therefore, it can be assumed that each design T80 arm consists of two straight beams (beam 1 of length L_1 and beam 2 of length L_2), perpendicular to each other. The left end of beam 1 is taken as fixed, and the right end of beam 2, which is the arm-microplate connection, is assumed to be guided. A point load P is applied to the end of beam 2 in the $-z$ direction.

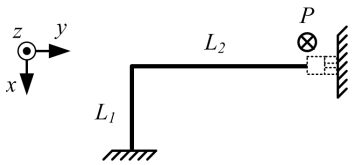

Figure 3.4: The equivalent elastic beam representation of one arm of design T80.

In order to find the spring constant of this 2-beam arm, a frame analysis that includes the torsional effects is required. The forces and moments acting on beam 1 and beam 2, which are shown in Fig. 3.5(a) and 3.5(b), respectively, are defined below:

M_g	the reaction moment at the guided end of beam 2;
M'_{junc}	the reaction moment at the junction, that applied to beam 2;
M_{junc}	the reaction moment at the junction, that applied to beam 1
T_1 and T_2	the twisting moment of beam 1 and beam 2.

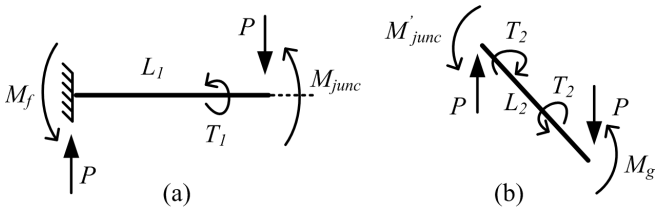

Figure 3.5: The forces and moments acting on (a) beam 1, (b) beam 2.

The point force P applied to the right end of beam 2 is directly transferred to the right end of beam 1. The total deflection of the arm-microplate connection (right end of beam 2) can be expressed as

$$v_{tot} = v_1(L_1) + v_2(L_2), \tag{3.27}$$

where

$v_1(L_1)$ the deflection of the right end of beam 1;
$v_2(L_2)$ the deflection of the right end of beam 2.

In order to find v_1, the elastic beam bending differential equation (Eq. (3.12)) is applied to a beam 1 portion of length x, which yields

$$EI\frac{\partial^2 v_1}{\partial x^2} = M_{junc} - P(L_1 - x). \tag{3.28}$$

Integrating Eq. (3.28) with respect to x gives the bending angle

$$\frac{\partial v_1}{\partial x} = \theta_1(x) = \frac{1}{EI}\left((M_{junc} - PL_1)x + \frac{Px^2}{2}\right) + C_1, \tag{3.29}$$

and integrating Eq. (3.29) gives the curve function of beam 1 $v_1(x)$

$$v_1(x) = \frac{1}{EI}\left(\frac{(M_{junc} - PL_1)x^2}{2} + \frac{Px^3}{6}\right) + C_1x + C_2. \tag{3.30}$$

The constants C_1 and C_2 are found from the boundary conditions for the fixed end, which can be stated as

$$v_1(0) = 0 \tag{3.31}$$

$$\left.\frac{\partial v_1}{\partial x}\right|_{x=0} = 0. \tag{3.32}$$

Using Eqs. (3.31) and (3.32) in Eqs. (3.29) and (3.30) yields

$$C_1 = C_2 = 0. \tag{3.33}$$

Therefore, the deflection and the bending angle of the free end is found as

$$v_1(L_1) = \frac{1}{EI}\left(\frac{M_{junc}L_1^2}{2} - \frac{PL_1^3}{3}\right) \tag{3.34}$$

$$\theta_1(L_1) = \frac{1}{EI}\left(M_{junc}L_1 - \frac{PL_1^2}{2}\right). \tag{3.35}$$

In order to find v_2, the elastic beam bending differential equation (Eq. (3.12)) is applied to a beam 2 portion of length x, which yields

$$EI\frac{\partial^2 v_1}{\partial x^2} = M_g - P(L_2 - x). \tag{3.36}$$

Integrating Eq. (3.36) with respect to x gives the bending angle

$$\frac{\partial v_2}{\partial x} = \theta_2(x) = \frac{1}{EI}\left((M_g - PL_2)x + \frac{Px^2}{2}\right) + D_1, \tag{3.37}$$

and integrating Eq. (3.37) gives the curve function of beam 2 $v_2(x)$

$$v_2(x) = \frac{1}{EI}\left(\frac{(M_g - PL_2)x^2}{2} + \frac{Px^3}{6}\right) + D_1 x + D_2. \tag{3.38}$$

The reaction moment M'_{junc} is found from the equilibrium of moments as

$$M'_{junc} = PL_2 - M_g. \tag{3.39}$$

The deflections of beam 1 and beam 2 are calculated separately; therefore the deflection of the left end of beam 2 is taken as zero:

$$v_2(0) = 0, \tag{3.40}$$

which leads to $D_2 = 0$.

Since the two beams are perpendicular, the reaction moment at the junction applying to one beam is equal to the twisting moment of the other beam, which can be stated as

$$M'_{junc} = T_1 \tag{3.41}$$

$$M_{junc} = T_2. \tag{3.42}$$

Similarly, at the junction, the bending angle of beam 1 equals the angle of twist of beam 2, and the bending angle of beam 2 equals the angle of twist of beam 1. These equalities can be stated as:

$$\theta_1(L_1) = \Phi_2(0) \tag{3.43}$$

$$\theta_2(0) = \Phi_1(L_1), \tag{3.44}$$

where

$\theta_1(L_1)$ and $\theta_2(0)$ bending angle of beam 1 and 2 at the junction;
$\Phi_1(L_1)$ and $\Phi_2(0)$ angle of twist of beam 1 and 2 at the junction.

The angles of twist are given by

$$\Phi_1(L_1) = \theta_2(0) = -\frac{T_1 L_1}{KG} \tag{3.45}$$

$$\Phi_2(0) = \theta_1(L_1) = -\frac{T_2 L_2}{KG}, \tag{3.46}$$

where G is the torsional modulus of rigidity, K is a factor dependent on the form and dimensions of the section, and the product of K and G (KG) is called the torsional stiffness. Using Eq. (3.42) in Eq. (3.35) gives

$$\theta_1(L_1) = \frac{1}{EI}\left(T_2 L_1 - \frac{PL_1^2}{2}\right) \tag{3.47}$$

and equating Eq. (3.47) to Eq. (3.46) gives

$$T_2 = \frac{PL_1^2}{2L_1 + \frac{2EIL_2}{KG}}. \tag{3.48}$$

Therefore, $v_1(x)$ can be expressed as

$$v_1(x) = \frac{1}{EI}\left(\frac{(T_2 - PL_1)x^2}{2} + \frac{Px^3}{6}\right), \tag{3.49}$$

where T_2 is given in Eq. (3.48).

In order to find $v_2(x)$, the unknowns M_g, D_1 and T_1 should be determined. Using Eq. (3.37), $\theta_2(0)$ is found to be equal to D_1. Therefore using Eq. (3.45), we reach

$$D_1 = -\frac{T_1 L_1}{KG}. \tag{3.50}$$

Using Eqs. (3.50) and (3.39), Eqs. (3.37) and (3.38) can be rewritten as

$$v_2(x) = \frac{1}{EI}\left(-\frac{T_1 x^2}{2} + \frac{Px^3}{6}\right) - \frac{T_1 L_1 x}{KG}; \tag{3.51}$$

$$\theta_2(x) = \frac{1}{EI}\left(-T_1 x + \frac{Px^2}{2}\right) - \frac{T_1 L_1}{KG}. \tag{3.52}$$

To find T_1, the boundary condition for the guided end is used, which can be stated as

$$\theta_2(L_2) = 0. \tag{3.53}$$

Combining Eqs. (3.53) and (3.52) yields

$$T_1 = \frac{PL_2^2}{2L_2 + \frac{2EIL_1}{KG}}. \tag{3.54}$$

Finally, substituting EI with $E_{Poly2}I_{comp}$, the total deflection of the arm, v_{tot} can be written as a summation of $v_1(L_1)$ and $v_2(L_2)$ as

$$v_{tot} = \frac{1}{E_{Poly2}I_{comp}}\left(\frac{(T_2 - PL_1)L_1^2}{2} + \frac{PL_1^3}{6} - \frac{T_1 L_2^2}{2} + \frac{PL_2^3}{6}\right) - \frac{T_1 L_1 L_2}{KG}. \tag{3.55}$$

Finally, the spring constant of the arm is found by dividing the external load P to the absolute value of deflection ($-v_{tot}$), which yields

$$k = -P/v_{tot}. \tag{3.56}$$

Similar to design T120, k is multiplied by two, in order to find k_{eq}, the equivalent spring constant.

$$k_{eq} = -2P/v_{tot}. \tag{3.57}$$

To find the torsional stiffness KG, the beam section is simplified by assuming that the width of the upper section (gold) is equal to that of the lower section (polysilicon), which makes the section a two-layer composite bar (see Fig. 3.6). The torsional stiffness of a laminated k-layer composite bar was found previously by Swanson as [52]

$$KG = \frac{(2a)(2b)^3}{4} \sum_{k=1}^{2} G_k \times \left[\frac{A_k(h_k - h_{k-1})}{b} - \frac{B_k(h_k^2 - h_{k-1}^2)}{2b^2} - \frac{h_k^3 - h_{k-1}^3}{3b^3} \right], \tag{3.58}$$

where $2a$ and $2b$ are the width and thickness of the simplified section, respectively.

$$a = w_{Poly2}/2 \tag{3.59}$$

$$b = (t_{Poly2} + t_{gold})/2 \tag{3.60}$$

Taking the index of the lower section (polysilicon) 1, and the index of the upper section (gold) 2, the coefficients h_k in Eq. (3.58) are found as

$$h_0 = -b \tag{3.61}$$

$$h_1 = t_{Poly2} - b \tag{3.62}$$

$$h_2 = b, \tag{3.63}$$

and the torsional modulus of rigidity (G_1 and G_2) are found as

$$G_1 = E_{Poly2}/2(1 + \nu_{Poly2}) \tag{3.64}$$

$$G_2 = E_{gold}/2(1 + \nu_{gold}). \tag{3.65}$$

To find the coefficients A_k and B_k ($k = 1, 2$), one must employ the boundary conditions, which are stated below.

$$\frac{1}{G_2} \left.\frac{\partial \Psi_2}{\partial y}\right|_{y=h_1} = \frac{1}{G_1} \left.\frac{\partial \Psi_1}{\partial y}\right|_{y=h_1} \tag{3.66}$$

$$\Psi_2|_{y=h_1} = \Psi_1|_{y=h_1} \tag{3.67}$$

$$\Psi_1|_{y=-b} = 0 \tag{3.68}$$

$$\Psi_2|_{y=b} = 0, \tag{3.69}$$

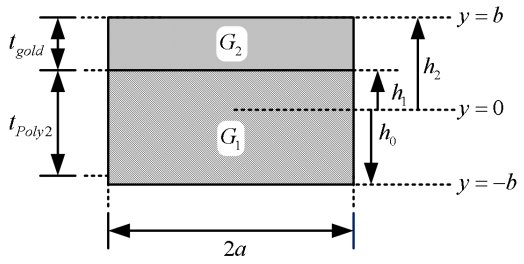

Figure 3.6: Figure showing the geometry of the simplified section, used in the calculation of the torsional stiffness.

where Ψ_k is the stress function, defined as

$$\Psi_k = \theta G_k b^2 \left(A_k - B_k \frac{y}{b} - \frac{y^2}{b^2} \right). \tag{3.70}$$

The first two boundary conditions (Eqs. (3.66) and (3.67)) are the continuity conditions at the interface, and the last two boundary conditions (Eqs. (3.68) and (3.69)) suggest that the outer surfaces ($y = \pm b$) are stress free. Using the boundary conditions, the coefficients A_1, A_2, B_1 and B_2 are found as

$$A_1 = 1 - B_1 \tag{3.71}$$

$$A_2 = 1 + B_2 \tag{3.72}$$

$$B_1 = \frac{(\Gamma - 1)^2}{2} + \frac{2\Gamma - 1}{2\Lambda} \tag{3.73}$$

$$B_2 = \Lambda(B_1 + 2\Gamma) - 2\Gamma, \tag{3.74}$$

where

$$\Gamma = h_1/b \tag{3.75}$$

$$\Lambda = G_1/G_2. \tag{3.76}$$

The values of these coefficients can be found by replacing Γ and Λ with their values, which can be found by using the geometric design parameters and material properties of gold and polysilicon. Using A_1, A_2, B_1 and B_2 in Eq. (3.58), KG is found.

3.1.3 Calculation of the Contact Voltage

The structural part of the electrostatic-structural model is completed by determining k_{eq}, the equivalent spring constant. To find the contact voltage, the electrostatic

force should be calculated as well. Fig. 3.7 shows the diagram of a basic movable plate capacitor. The movable plate, which corresponds to the microplate of the microbolometer, is attached to a spring having a spring constant of k_{eq}. The spring in Fig. 3.7 is the equivalent model for the microbolometer arms, and the spring constant k_{eq} is equal to the equivalent spring constant of the arms, calculated in the previous section. The gap between the base plate and the movable plate in the unactuated state ($V_{act} = 0$) is g_0, and the gap at equilibrium is g. The area of the microplate and the base plate is A_{mp}.

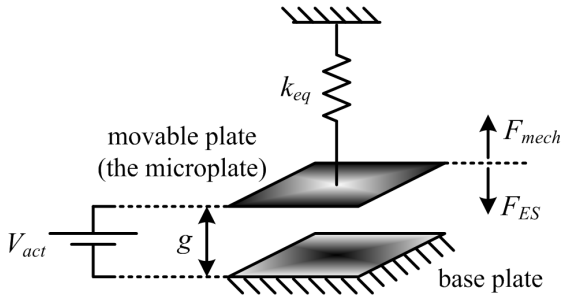

Figure 3.7: Schematic of a movable plate capacitor. The movable plate and the spring represent the microplate and the microbolometer arms, respectively.

The energy stored in a parallel plate capacitor in terms of the voltage V_{act} and the electrical capacitance C_{el} can be expressed as

$$W = \frac{1}{2} C_{el} V_{act}^2, \tag{3.77}$$

where the capacitance is given by

$$C_{el} = \frac{\epsilon_0 A_{mp}}{g}. \tag{3.78}$$

The electrostatic force generated on the movable plate by V_{act} can be found by

$$F_{ES} = -\frac{\partial W\left(V_{act}, g\right)}{\partial g}\bigg|_{V_{act}} = -\left[-\frac{\epsilon_0 A_{mp} V_{act}^2}{2g^2}\right] = \frac{\epsilon_0 A_{mp} V_{act}^2}{2g^2}. \tag{3.79}$$

The displacement of the movable plate $(g_0 - g)$ is equal to the elongation of the spring. The mechanical force (F_{mech}), which is due to the elongation of the spring, tries to restore the movable plate back to its original position, and it is given by

$$F_{mech} = k_{eq}(g_0 - g). \tag{3.80}$$

To find the contact voltage $V_{contact}$, the net force on the microplate (F_{net}) is expressed first.

$$F_{net} = F_{mech} - F_{ES} \tag{3.81}$$

$$\Rightarrow F_{net} = k_{eq}(g_0 - g) - \frac{\epsilon_0 A_{mp} V_{act}^2}{2g^2}. \tag{3.82}$$

At $V_{contact}$, both F_{net} and the derivative of F_{net} with respect to g equals zero, which gives

$$V_{contact} = \sqrt{\frac{8k_{eq}g_0^3}{27\epsilon_0 A_{mp}}}. \tag{3.83}$$

Finding the contact voltage completes the electrostatic structural model. The Matlab script that calculates the contact voltage of the test structures is given in Appendix A. To validate the electrostatic-structural model, a finite element model is constructed in Section 3.5.2. The contact voltages found by both the model explained here and the finite element model are compared to the experimental results in Section 4.2.

3.2 Infrared Absorption Model

In this section, modeling of the coupling efficiency η is introduced. Determining η is important for determining the main performance parameters of a microbolometer, such as responsivity and detectivity. It also determines the spectral response of the microbolometer, namely how the responsivity changes with the wavelength of the incident radiation. The wavelength dependency of η is based on the fact that the thicknesses of the pixel layers are comparable to the infrared wavelength. Therefore, the absorption depends not only on the absorption characteristics of the top layer of the microplate, but also on the interference effects between the thin film layers forming the pixel.

The coupling efficiency, which is defined as the ratio and the absorbed power to the incident power, can be found by solving the transverse electromagnetic (TEM) wave equations[1]. Fig. 3.8 shows an N-layer medium, where the leftmost boundary corresponds to the top layer of the microbolometer and the rightmost boundary

[1]Instead of TEM wave equations, the microbolometer can be modeled as a transmission line network as well [53].

corresponds to the micromirror. The TEM wave is assumed to propagate in the z direction, which is perpendicular to the layer surfaces. The total number of layers, including the air gap and the thin film layers forming the microbolometer pixel, is N. For an arbitrary layer n, the wave admittance (Y_n) is given by

$$Y_n = \sqrt{\frac{\epsilon_n}{\mu_n}} = Y_0\sqrt{\frac{\epsilon_{r_n}}{\mu_{r_n}}}, \tag{3.84}$$

where μ_{r_n} and ϵ_{r_n} are the relative permeability and permittivity of layer n and Y_0 is the admittance of free space. The propagation constant for layer n at a given wavelength λ is defined as

$$k_n = j\frac{2\pi}{\lambda}\sqrt{\epsilon_{r_n}\mu_{r_n}} \tag{3.85}$$

For lossy media, complex relative permittivity is used instead of relative permittivity, given by [54]

$$\hat{\epsilon_r} = \epsilon_{r_n} + j\frac{\sigma_n}{\omega\epsilon_0} \tag{3.86}$$

where ω is the wave frequency (rad/sec), ϵ_0 is the permittivity of free space, σ_n is the conductivity of layer n, and j is the imaginary unit. For free space, both the relative permittivity and permeability are equal to one ($\mu_{r_n} = \epsilon_{r_n} = 1$), giving

$$Y_n = Y_0 = \frac{1}{377}\,\Omega^{-1} \tag{3.87}$$

as the free space admittance. Generally, magnetic materials are not used in a microbolometer, (i.e. $\mu_{r_n} = 1$) and so the equations for Y_n and k_n can be simplified as

$$Y_n = Y_0\sqrt{\epsilon_{r_n}} \tag{3.88}$$

$$k_n = j\frac{2\pi}{\lambda}\sqrt{\epsilon_{r_n}}. \tag{3.89}$$

The electric field (E-field) vector for layer n at position z ($z_{n-1} \leq z \leq z_n$) can be written as a summation of two vectors.

$$\vec{E}_n(z) = \vec{E}_{n,r}(z) + \vec{E}_{n,l}(z) \tag{3.90}$$

In the above equation, the E-field vectors $\vec{E}_{n,r}(z)$ and $\vec{E}_{n,l}(z)$ correspond to the waves that propagate to the right (positive-z direction) and left (negative-z direction), respectively. Similar to Eq. (3.90), the magnetic field (H-field) for layer n

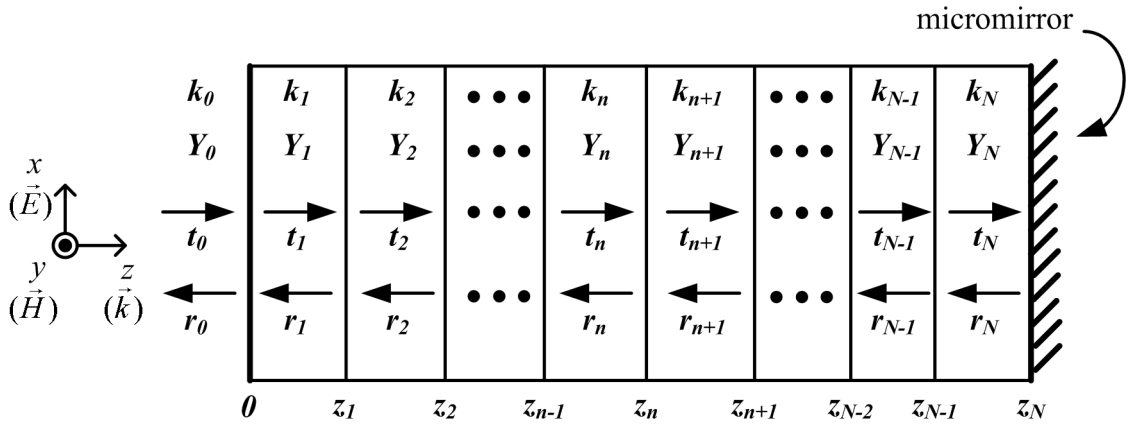

Figure 3.8: Schematic showing a multilayer structure, where the TEM wave propagates in the z direction. The leftmost layer corresponds to the air interface, and the rightmost interface corresponds to the micromirror. The parameters k_n, Y_n, t_n and r_n are the propagation constant, wave admittance, transmission coefficient and reflection coefficient of layer n, respectively.

at position z can be written as a summation of the right-propagating and left-propagating vectors.

$$\vec{H}_n(z) = \vec{H}_{n,r}(z) + \vec{H}_{n,l}(z). \tag{3.91}$$

In Eq. (3.90), $\vec{E}_{n,r}(z)$ and $\vec{E}_{n,l}(z)$ can be expressed as

$$\vec{E}_{n,r}(z) = \hat{x}\, t_n E_0 e^{-jk_n z} \tag{3.92}$$

$$\vec{E}_{n,l}(z) = \hat{x}\, r_n E_0 e^{jk_n z}, \tag{3.93}$$

where t_n and r_n are the transmission and reflection coefficients for layer n, respectively (see Fig. 3.8). In a TEM wave, the electric field $\vec{E}$, magnetic field $\vec{H}$ and the propagation direction $\vec{k}$ obey the right hand rule. Therefore, the magnetic field (H-field) of a TEM wave that propagates in the k-direction is given by [54]

$$\vec{H} = \hat{k} \times Y\vec{E}, \tag{3.94}$$

where $\vec{H}$ is the H-field, $\vec{E}$ is the E-field, Y is the wave admittance and $\vec{k}$ is the unit vector in the propagation direction. Therefore, the H-field of the wave that propagates to right ($\vec{H}_{n,r}(z)$) and to left ($\vec{H}_{n,l}(z)$) can be found as follows

$$\vec{H}_{n,r}(z) = \hat{z} \times Y_n \vec{E}_{n,r}(z) = \hat{y}\, Y_n t_n E_0 e^{-jk_n z} \tag{3.95}$$

$$\vec{H}_{n,l}(z) = -\hat{z} \times Y_n \vec{E}_{n,l}(z) = -\hat{y}\, Y_n r_n E_0 e^{jk_n z}. \tag{3.96}$$

Similarly, the E-field and H-field vectors at layer $n+1$ can be expressed as

$$\vec{E}_{n+1,r}(z) = \hat{x}\, t_{n+1} E_0 e^{-jk_{n+1}z} \tag{3.97}$$

$$\vec{E}_{n+1,l}(z) = \hat{x}\, r_{n+1} E_0 e^{jk_{n+1}z} \tag{3.98}$$

$$\vec{H}_{n+1,r}(z) = \hat{y}\, Y_{n+1} t_{n+1} E_0 e^{-jk_{n+1}z} \tag{3.99}$$

$$\vec{H}_{n+1,l}(z) = -\hat{y}\, Y_{n+1} r_{n+1} E_0 e^{jk_{n+1}z}, \tag{3.100}$$

where $z_n \leq z \leq z_{n+1}$.

To determine the unknowns t_n and r_n, the boundary conditions should be employed. Both the E-field and the H-field satisfy the continuity condition at the boundaries. At the boundary $z = z_n$, the continuity in the E-field and the H-field can be stated as

$$\vec{E}_n(z_n) = \vec{E}_{n+1}(z_n) \tag{3.101}$$

$$\vec{H}_n(z_n) = \vec{H}_{n+1}(z_n) \tag{3.102}$$

Using Eqs. (3.90) and (3.91), the boundary conditions at $z = z_n$ (Eqs. (3.101) and (3.102)) can be rewritten as

$$\vec{E}_{n,l}(z_n) + \vec{E}_{n,r}(z_n) = \vec{E}_{n+1,l}(z_n) + \vec{E}_{n+1,r}(z_n) \tag{3.103}$$

$$\vec{H}_{n,l}(z_n) + \vec{H}_{n,r}(z_n) = \vec{H}_{n+1,l}(z_n) + \vec{H}_{n+1,r}(z_n). \tag{3.104}$$

By using Eqs. (3.93), (3.92), (3.98) and (3.97), Eq. (3.103) can be rewritten as

$$t_n e^{-jk_n z_n} + r_n e^{jk_n z_n} = t_{n+1} e^{-jk_{n+1} z_n} + r_{n+1} e^{jk_{n+1} z_n}. \tag{3.105}$$

Similarly, by using Eqs. (3.96), (3.95), (3.100) and (3.99), Eq. (3.104) can be rewritten as

$$Y_n t_n e^{-jk_n z_n} - Y_n r_n e^{jk_n z_n} = Y_{n+1} t_{n+1} e^{-jk_{n+1} z_n} - Y_{n+1} r_{n+1} e^{jk_{n+1} z_n} \tag{3.106}$$

From Eqs. (3.105) and (3.106), the coefficients t_n and r_n can be found in terms of t_{n+1} and r_{n+1}.

$$t_n = \frac{1}{2e^{-jk_n z_n}} \left(t_{n+1} e^{-jk_{n+1} z_n} \left(1 + \frac{Y_{n+1}}{Y_n} \right) + r_{n+1} e^{jk_{n+1} z_n} \left(1 - \frac{Y_{n+1}}{Y_n} \right) \right) \tag{3.107}$$

$$r_n = \frac{1}{2e^{jk_n z_n}} \left(t_{n+1} e^{-jk_{n+1} z_n} \left(1 - \frac{Y_{n+1}}{Y_n} \right) + r_{n+1} e^{jk_{n+1} z_n} \left(1 + \frac{Y_{n+1}}{Y_n} \right) \right). \tag{3.108}$$

Eqs. (3.107) and (3.108) can be used in a recursive manner to find the coefficients t_n and r_n. However, in order to start the iterations, the transmission and reflection coefficients of layer-N, t_N and r_N, need to be found by using the boundary condition at the micromirror surface ($z = z_N$). The micromirror acts as a perfect electric conductor (PEC), leading to the following boundary condition at its surface.

$$\vec{E}_N(z_N) = \vec{E}_{N,l}(z_N) + \vec{E}_{N,r}(z_N) = 0, \tag{3.109}$$

which gives

$$t_N E_0 e^{-jk_N z_N} + r_N E_0 e^{jk_N z_N} = 0. \tag{3.110}$$

From the above equation, t_N can be expressed in terms of r_N as

$$t_N = -r_N e^{2jk_N z_N}. \tag{3.111}$$

Taking t_N as the initial point, one can recursively find t_n and r_n in terms of r_N, where n equals $N-1$ at the first iteration and $n = 0$ at the last iteration. The iterations end as r_0 and t_0 are found. The coupling efficiency η is found by using the coefficients t_0 and r_0. The overall reflection coefficient, which is defined as the ratio of the amplitude of the reflected wave to the amplitude of the incident wave at $z = 0$, is given by

$$\Gamma = \frac{r_0}{t_0}. \tag{3.112}$$

The ratio of the reflected power to the incident power is equal to $|\Gamma|^2$. Finally, since the ratio of the absorbed power and the ratio of the reflected power sums to 1, the ratio of the absorbed power to the incident power (η) can be expressed as

$$\eta = 1 - |\Gamma|^2 = 1 - \left|\frac{r_0}{t_0}\right|^2 \tag{3.113}$$

The model explained above is applicable to microbolometers having a micromirror that acts as a PEC, i.e. it reflects back all the radiation incident on it. A micromirror used in a microbolometer pixel is a metal with good reflective properties in the infrared region, such as aluminum or gold. However, the test structures fabricated in this study do not have a micromirror deposited on the substrate, due to the limitations of the PolyMUMPs process. Instead, the backside of the substrate was painted with silver paste. Hence, the back of the substrate acts as a micromirror and there is no micromirror on top of the substrate.

The layers that form a test structure (design T80 or T120) are shown in Fig. 3.9. In a test structure, the infrared power is absorbed not only by the microplate, but also by the substrate and the Poly 0 layer. Since Eq. (3.113) calculates the ratio of the absorbed power by all the layers prior to the micromirror, it does not give the correct coupling efficiency. In order to find η, the power absorbed only by the Poly 2 layer needs to be calculated.

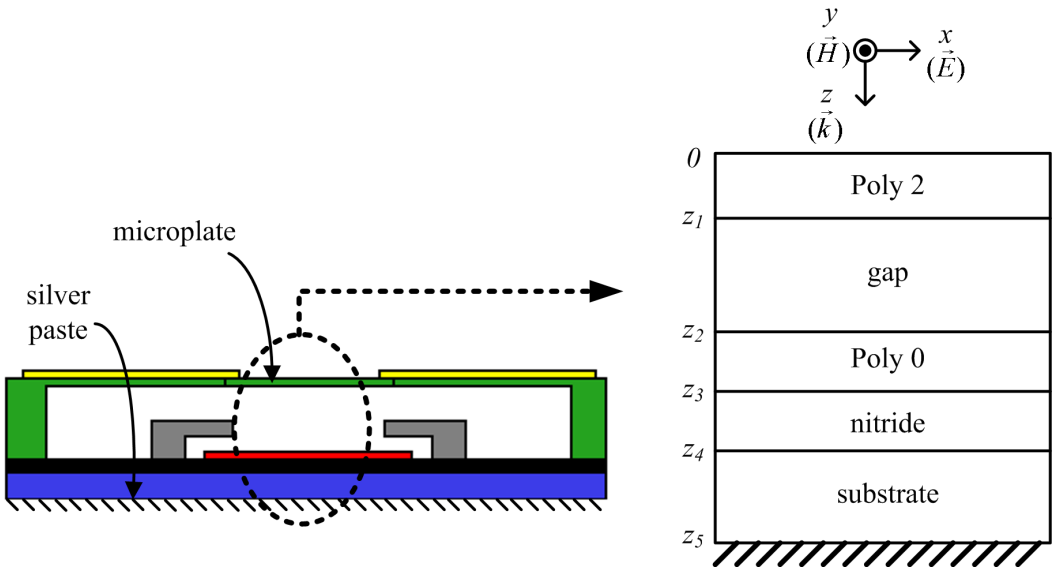

Figure 3.9: Schematic showing the layers of the fabricated test structures.

To find the absorbed power at the Poly 2 layer, the complex Poynting vector is used. For a wave that propagates in the z direction, the average power per unit area at position z is given by [55]

$$P_{avg}(z) = Re\left(S(z)\right), \tag{3.114}$$

where $S(z)$ is the complex Poynting vector at z, given by [55]

$$S(z) = \frac{1}{2}\vec{E}(z) \times \vec{H}^{*}(z). \tag{3.115}$$

For the case shown in Fig. 3.9, the power absorbed at the microplate (layer 1) is equal to the difference in the average power at position $z = 0$ and $z = z_1$, which can be expressed as

$$\begin{aligned} P_{abs} &= P_{avg}(0) - P_{avg}(z_1) && (3.116)\\ &= Re\{S(0)\} - Re\{S(z_1)\} && (3.117)\\ &= \frac{1}{2}Re\{\vec{E}_1(0) \times \vec{H}_1^{*}(0)\} - \frac{1}{2}Re\{\vec{E}_1(z_1) \times \vec{H}_1^{*}(z_1)\} && (3.118) \end{aligned}$$

The incident radiation power P_{in} can be calculated by the complex Poynting vector as well. It should be noted that the incident radiation propagates towards the microplate (positive-z direction), therefore only the right propagating components of $\vec{E}_0(0)$ and $\vec{E}_0(0)$ should be taken into account when P_{in} is calculated. The E-field and the H-field of the wave propagating in the negative-z direction ($\vec{E}_{0,l}(0)$ and $\vec{H}_{0,l}(0)$) should not be used. The complex Poynting vector for the incident radiation at $z = 0$ is stated as

$$S_{in}(0) = \frac{1}{2}\vec{E}_{0,r}(0) \times \vec{H}^*_{0,r}(0) \tag{3.119}$$

and the input power is found as

$$P_{in} = Re\{S_{in}(0)\} = \frac{1}{2}Re\{\vec{E}_{0,r}(0) \times \vec{H}^*_{0,r}(0)\} \tag{3.120}$$

Finally, the coupling efficiency for the test structures (η') can be stated as

$$\eta' = \frac{P_{abs}}{P_{in}} \tag{3.121}$$

$$= \frac{Re\{S(0)\} - Re\{S(z_1)\}}{Re\{S_{in}(0)\}} \tag{3.122}$$

$$= \frac{Re\{\vec{E}_1(0) \times \vec{H}^*_1(0)\} - Re\{\vec{E}_1(z_1) \times \vec{H}^*_1(z_1)\}}{Re\{\vec{E}_{0,r}(0) \times \vec{H}^*_{0,r}(0)\}}, \tag{3.123}$$

which finalizes the extension of the spectral absorption model for the test structures. It should be noted that the coupling efficiency of the test structures is denoted by η', to distinguish it from the η calculated in Eq. (3.113).

The spectral absorption model explained above was implemented in MATLAB. The corresponding MATLAB code, which calculates the IR absorption of the fabricated test structures for a user-defined range of wavelengths, is given in Appendix B. To validate the model, a finite element model is constructed, the details of which are given in Section 3.5.3. The comparison of the results of the model with finite element simulations is given in Section 4.3.

3.3 Composite Region Thermal Model

In this section, a thermal model is presented for conventional microbolometers and for tunable thermal conductance microbolometers in their unactuated state, and

called a composite region thermal model. The main heat transfer mechanism of these devices is the heat conduction to the substrate through the microbolometer arms, whereas in the actuated state i.e. at contact state, the heat conduction through the new heat links formed by the actuation becomes the main heat transfer mechanism. Therefore, the model presented here cannot be used in tunable thermal conductance microbolometers in their actuated state.

The composite region thermal model is developed for two basic microbolometer shapes, shape-A and shape-B, which are shown in Fig. 3.10. The only difference between shape-A and shape-B is that in shape-A, the arms are connected to the mid-edges of the microplate and in shape-B, the arms are connected to the corners of the microplate. While the model is developed for shape-A and shape-B only, it can be readily modified to account for many other different shapes.

The thermal model presented here starts with the approximation of the microbolometer pixel as a one-dimensional (1D) "composite slab" consisting of two parallel regions of the same width (Section 3.3.1). The constriction resistance is calculated and added as a contact resistance between the two regions (Section 3.3.2). The thermal parameters are then estimated solving the heat conduction problem for a composite slab (Sections 3.3.3, 3.3.4 and 3.3.5). The extension of the model for the actuated state is given in Section 3.4.

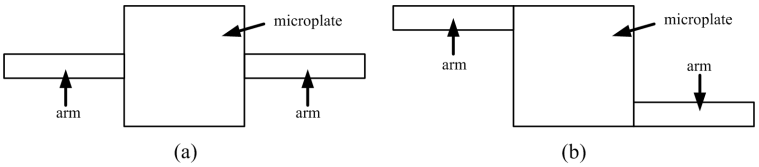

Figure 3.10: Schematic of the microbolometer shapes modeled: (a) Shape-A (b) Shape-B.

3.3.1 Composite Region Approximation

The composite region approximation presented here can be divided into three steps. The first step uses the symmetry of the microbolometer through the middle of the microplate to obtain what we have called here a "half-microbolometer". As shown schematically in Fig. 3.11, each half-microbolometer is composed of two regions, i.e. Region 1 (the half-microplate, or simply the half-plate) and Region 2 (the arm).

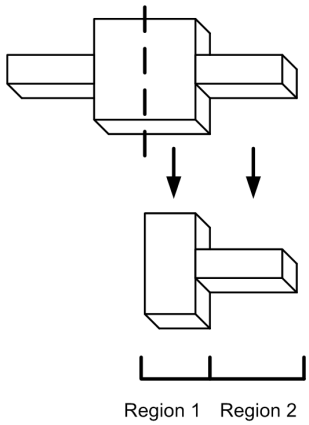

Figure 3.11: Schematic showing the use of symmetry to reduce the complexity of the analysis. The Shape-A microbolometer has been reduced to a half-microbolometer composed of two regions (1 and 2).

In a typical microbolometer pixel, both the arms and the microplate are composed of a stack of multiple thin film layers of different widths and thicknesses, resulting in three-dimensional (3D) heat flow. The aim of the second step is to transfer the half-microbolometer into a simpler shape, where heat flows in-plane only. This is done by finding the equivalent thermal parameters for each region, and replacing the thin-film layers with a single layer, having the equivalent thermal parameters (see Fig. 3.12). Since the heat flows in 2D in the resulting structure, this step can be considered as a 3D to 2D transformation. It should be noted that for the purpose of this part of the analysis, we are only considering Shape-A microbolometers. For Shape-B microbolometers, the validity of the model will be extended later.

In general, the equivalent thermal conductance of parallel layers can be expressed as the summation of their individual thermal conductances. Hence, for both region 1 ($r = 1$) and region 2 ($r = 2$), the equivalent thermal conductance G_r is given by

$$G_r = \sum_{i=1}^{M} k_{ri} \frac{Z_{ri} W_{ri}}{L_r} \quad (r = 1, 2), \tag{3.124}$$

where

k_{ri} thermal conductivity of i^{th} layer of region r;

Z_{ri} thickness of i^{th} layer of region r;

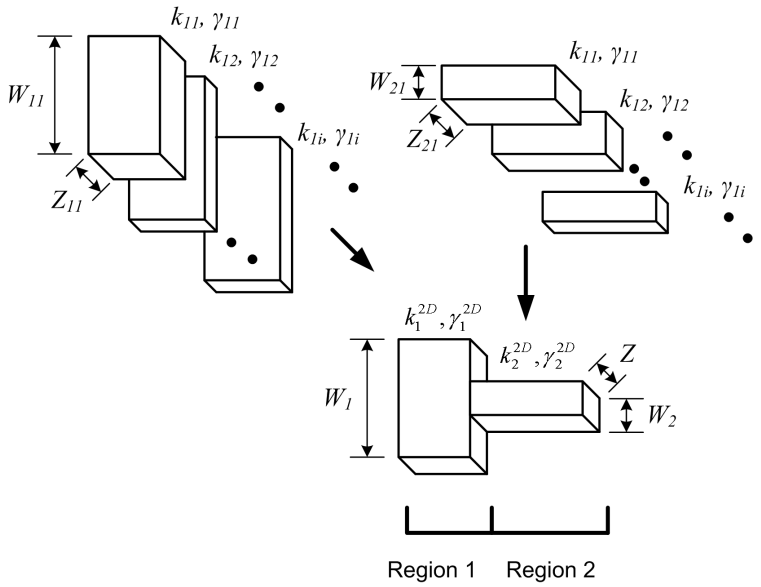

Figure 3.12: Schematic showing a simplified Shape-A half-microbolometer obtained by using one-layer equivalents for each region. Notice that the resulting shape has two uniform regions with the same thickness Z.

W_{ri} width of i^{th} layer of region r;
M number of parallel layers forming region r.

To find the equivalent thermal conductivity, Eq. (3.124) is equated to the thermal conductance of the transformed structure for both regions, which gives

$$k_r^{2D} \frac{ZW_r}{L_r} = \sum_{i=1}^{M} k_{ri} \frac{Z_{ri} W_{ri}}{L_r} \quad (r = 1, 2), \tag{3.125}$$

where

k_r^{2D} equivalent thermal conductivity of region r;
W_r width of region r;
L_r length of region r;
Z total thickness.

From the above expression, k_r^{2D} can be found as

$$k_r^{2D} = \frac{1}{ZW_r} \sum_{i=1}^{M} k_{ri} Z_{ri} W_{ri} \quad (r = 1, 2). \tag{3.126}$$

Similarly, the equivalent thermal capacitance for region r (C_r) is given by

$$C_r = \sum_{i=1}^{M} \gamma_{ri} Z_{ri} W_{ri} L_r, \tag{3.127}$$

where γ_{ri} is the volumetric heat capacity of i^{th} layer of region r. Eq. (3.127) is equated to the thermal capacitance of the transformed structure as

$$\gamma_r^{2D} Z W_r L_r = \sum_{i=1}^{M} \gamma_{ri} Z_{ri} W_{ri} L_r \quad (r = 1, 2), \tag{3.128}$$

where γ_r^{2D} is the equivalent volumetric heat capacity of region r, found as

$$\gamma_r^{2D} = \frac{1}{Z W_r} \sum_{i=1}^{M} \gamma_{ri} Z_{ri} W_{ri} \quad (r = 1, 2). \tag{3.129}$$

Eqs. (3.126) and (3.129) enable the multilayered three-dimensional structure of the microbolometer to be represented as a structure composed of two homogenous regions, having k_r^{2D} and γ_r^{2D} as their thermal parameters (see Fig. 3.12).

The model obtained at the end of the second step has two regions having widths W_1 and W_2. This prevents the application of a composite region solution, which requires that both regions have the same width. Hence, as a third step, the width of region 2 is transformed to be of equal width to region 1, by updating the thermal parameters of region 2. Figure 3.13 shows the application of the third step to microbolometer pixels of shape-A. In the resulting structure, heat flows only in one-direction (1D), so the thermal parameters of this structure are denoted with the superscript 1D.

The thermal conductance and thermal capacitance of region 2 should remain the same after the transformation, while the width is changed from W_2 to W_1. Equating the thermal conductance of the initial structure to that of the transformed structure, we have

$$k_2^{1D} \frac{Z W_1}{L_2} = k_2^{2D} \frac{Z W_2}{L_2} \tag{3.130}$$

resulting in

$$k_2^{1D} = k_2^{2D} \frac{W_2}{W_1}, \tag{3.131}$$

where k_2^{2D} is the thermal conductivity of region 2 before transformation, and k_2^{1D} after transformation. Similarly,

$$\gamma_2^{1D} Z W_1 L_2 = \gamma_2^{2D} Z W_2 L_2 \tag{3.132}$$

$$\Rightarrow \gamma_2^{1D} = \gamma_2^{2D} \frac{W_2}{W_1}, \tag{3.133}$$

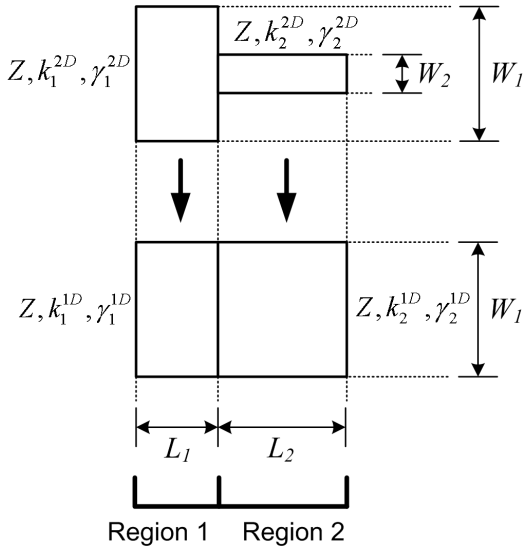

Figure 3.13: The schematic demonstrating the 2D to 1D transformation of the half-microbolometer.

where γ_2^{2D} and γ_2^{1D} are the volumetric heat capacities of region 2 before and after transformation. Since the width of region 1 does not change, the thermal conductivity and the volumetric heat capacity of region 1 remains unchanged. Hence,

$$k_1^{1D} = k_1^{2D} \tag{3.134}$$

$$\gamma_1^{1D} = \gamma_1^{2D}. \tag{3.135}$$

The final structure obtained after the transformations is a two-region structure with contact resistance R_c at the interface, where the contact resistance stands for the constriction resistance between the half-plate and the arm. The estimation of the constriction resistance is presented next.

3.3.2 Constriction Resistance Estimation

In this section, the constriction resistance is calculated for the two basic microbolometer shapes (shape A and B). Opposite to constriction resistance, where the heat flows from a wider area to a narrower area, we have a spreading resistance. Although their flow directions are opposite, the same formulae can be used for calculating both the spreading and constriction resistances.

Spreading and constriction resistances have been analyzed and formulated for various geometries and boundary conditions in [46]. For the half-microbolometer

of shape-A, the thermal conduction is similar to the case of heat flowing in a 2D channel, whose width decreases abruptly (see Fig. 3.14(a)). Hence, the constriction resistance can be expressed as [46]

$$R_{shape-A} = \frac{1}{2\pi Z k}\left[\left(\epsilon + \frac{1}{\epsilon}\right)\ln\frac{1+\epsilon}{1-\epsilon} + 2\ln\frac{1-\epsilon^2}{4\epsilon}\right], \tag{3.136}$$

where Z is the thickness, k is the thermal conductivity, and ϵ is the ratio of widths, expressed as

$$\epsilon = \frac{W_1}{W_2}. \tag{3.137}$$

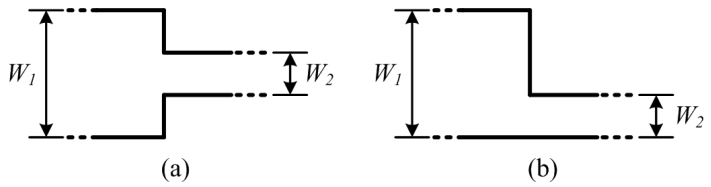

Figure 3.14: A two-dimensional channel approximation for (a) shape-A and (b) shape-B half-microbolometer. The width of the channel decreases abruptly from W_1 to W_2.

For shape-B half-microbolometers (Fig. 3.10(b)), since the arms are connected to the corners of the microplate, the two regions are not concentric, which makes the solution above not directly applicable to the shape-B half-microbolometer. To overcome this problem, the half-microbolometer shape-B is mirrored in the y-direction, as shown in Fig. 3.15. This new half-microbolometer resembles a half-microbolometer shape-A and its total constriction resistance is the equivalent of two half-microbolometer shape-B resistances in parallel. Therefore, the total constriction resistance of the half-microbolometer shape-B can be calculated from

$$\frac{1}{2}R_{shape-B} = R_{shape-A} = \frac{1}{2\pi Z k}\left[\left(\epsilon + \frac{1}{\epsilon}\right)\ln\frac{1+\epsilon}{1-\epsilon} + 2\ln\frac{1-\epsilon^2}{4\epsilon}\right]. \tag{3.138}$$

Now that we have found the constriction resistance for shapes A and B, they can be added to the composite region model as contact resistances.

3.3.3 Solution of the Composite Region Model

The half microbolometer shape-A pixel was previously reduced to a two-region structure with a contact resistance at the interface. The remaining step is to solve

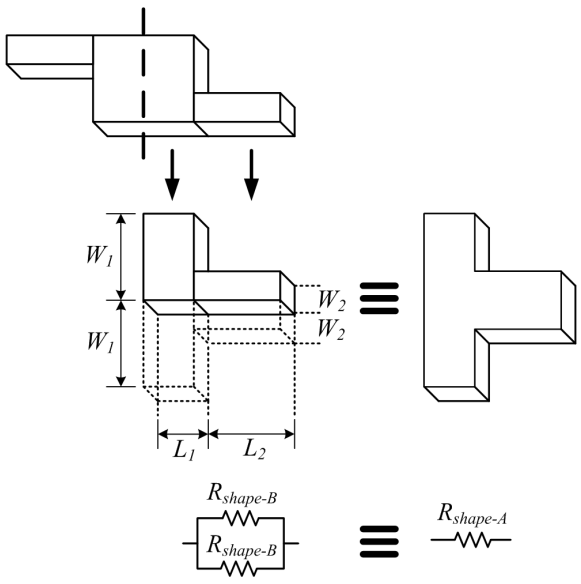

Figure 3.15: Schematic showing the procedure to calculate the constriction resistance of the half-microbolometer shape-B.

the heat conduction boundary problem for the system shown in Fig. 3.16, which can be expressed as

$$\alpha_r \nabla^2 \theta_r(x,t) + \frac{\alpha_r}{k_r^{1D}} g_r(x,t) = \frac{d\theta_r(x,t)}{dt}, \tag{3.139}$$

for $x_r \leq x \leq x_{r+1}$, $t > 0$ and $r = 1, 2$. In Eq. (3.139), α_r is the thermal diffusivity, defined as

$$\alpha_r = \frac{k_r^{1D}}{\gamma_r^{1D}} \quad (\mathrm{m}^2/\sec) \tag{3.140}$$

The term $g_r(x,t)$ stands for the heat generation rate per unit volume ($\mathrm{W/m^3}$) in region r. The source of the generated heat can be either the IR radiation or Joule heating by electrical biasing. Since the whole structure is initially at the substrate temperature T_s, Eq. (3.139) is stated in terms of the excess temperature, $\theta_r(x,t)$, which is defined as

$$\theta_r(x,t) = T_r(x,t) - T_s. \tag{3.141}$$

In Fig. 3.16, the leftmost boundary corresponds to the line of symmetry through the microplate. Since there is zero heat flow across this boundary, we can assume that it is thermally insulated.

$$\frac{d\theta_1(x_1,t)}{dx} = 0 \tag{3.142}$$

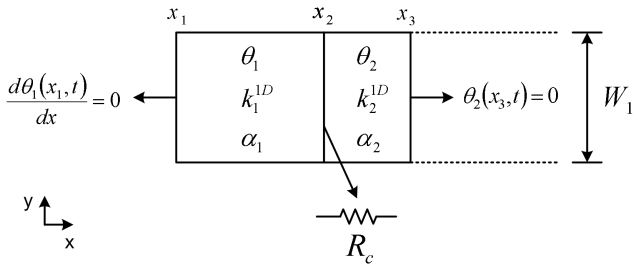

Figure 3.16: One dimensional heat conduction problem with two parallel regions.

The rightmost boundary corresponds to the connection of the arm to the substrate. Since the substrate is assumed to behave as a perfect heat sink, the temperature at this boundary should be constant.

$$\theta_2(x_3, t) = 0. \tag{3.143}$$

The interface between region 1 and 2 is assumed to have a constant contact resistance, which means that the heat flow is continuous but the temperature is discontinuous. The boundary conditions for the interface can be written as

$$k_1^{1D} \frac{d\theta_1(x_2, t)}{dx} = k_2^{1D} \frac{d\theta_2(x_2, t)}{dx} \tag{3.144}$$

and

$$-k_1^{1D} \frac{d\theta_1(x_2, t)}{dx} = h_c(\theta_1(x_2, t) - \theta_2(x_2, t)). \tag{3.145}$$

In Eq. (3.145), h_c is the contact conductance, which can be written in terms of contact resistance R_c as

$$h_c = \frac{1}{R_c Z W_1}. \tag{3.146}$$

The contact resistance R_c is equal to the constriction resistance calculated in the previous section for both shapes. At $t = 0$, the whole system is at the substrate temperature, which can be written as

$$\theta_r(x, 0) = 0, \tag{3.147}$$

for $x_r \leq x \leq x_{r+1}$ and $r = 1, 2$.

The solution of the transient heat conduction problem for composite regions has been solved by Bulavin and Kashfeev [56], using the orthogonal-expansion technique. This method extends the orthogonality of eigenfunctions that form the temperature function to the case of multilayer regions. The excess temperature

$\theta_r(x,t)$ can be expressed in the form of an infinite series, where each term is the product of space and time variables.

$$\theta_r(x,t) = \sum_{n=1}^{\infty} X_{rn}(x)\Gamma_n(t) \quad (r = 1, 2) \tag{3.148}$$

In Eq. (3.148), $\Gamma_n(t)$ is the n^{th} time-dependent term and $X_{rn}(x)$ is the n^{th} eigenfunction for region r that satisfy the following eigenvalue problem.

$$\alpha_r \nabla^2 X_{rn}(x) + \beta_n^2 X_{rn}(x) = 0, \tag{3.149}$$

where β_n is the nth eigenvalue. The boundary conditions for Eq. (3.149) are stated below.

$$\frac{dX_{1n}(x_1)}{dx} = 0 \tag{3.150}$$

$$-k_1^{1D}\frac{dX_{1n}(x_2)}{dx} = h(X_{1n}(x_2) - X_{2n}(x_2)) \tag{3.151}$$

$$k_1^{1D}\frac{dX_{1n}(x_2)}{dx} = k_2^{1D}\frac{dX_{2n}(x_2)}{dx} \tag{3.152}$$

$$X_{2n}(x_3) = 0 \tag{3.153}$$

The solution of Eq. (3.149) has the following form

$$X_{rn}(x) = C_{rn}\phi_{rn}(x) + D_{rn}\psi_{rn}(x), \tag{3.154}$$

where $\phi_{rn}(x)$ and $\psi_{rn}(x)$ are the linearly independent solutions of Eq. (3.149), and C_{rn} and D_{rn} are constants that can be found by applying the boundary conditions. The solutions for $\phi_{rn}(x)$ and $\psi_{rn}(x)$ are different in cartesian, cylindrical and spherical coordinates. In cartesian coordinates, they are defined as

$$\phi_{rn}(x) = \cos\left(\frac{\beta_n}{\sqrt{\alpha_r}}x\right) \tag{3.155}$$

$$\psi_{rn}(x) = \sin\left(\frac{\beta_n}{\sqrt{\alpha_r}}x\right). \tag{3.156}$$

In order to find the constants C_{rn} and D_{rn}, the boundary conditions (Eqs. (3.150)-

(3.153)) are rewritten by using Eq. (3.154) as

$$C_{1n}\phi_{1n}^{'}(x_1) + D_{1n}\psi_{1n}^{'}(x_1) = 0 \quad (3.157)$$

$$C_{1n}\left(\frac{-k_1^{1D}}{h}\phi_{1n}^{'}(x_2) - \phi_{1n}(x_2)\right) + D_{1n}\left(\frac{-k_1^{1D}}{h}\psi_{1n}^{'}(x_2) - \psi_{1n}(x_2)\right) + C_{2n}\phi_{2n}(x_2) + D_{2n}\psi_{2n}(x_2) = 0 \quad (3.158)$$

$$\frac{k_1^{1D}}{k_2^{1D}}\left(C_{1n}\phi_{1n}^{'}(x_2) + D_{1n}\psi_{1n}^{'}(x_2)\right) - C_{2n}\phi_{2n}^{'}(x_2) - D_{2n}\psi_{2n}^{'}(x_2) = 0 \quad (3.159)$$

$$C_{2n}\phi_{2n}(x_3) + D_{2n}\psi_{2n}(x_3) = 0, \quad (3.160)$$

where

$$\phi_{rn}^{'}(x) = \frac{d\phi_{rn}(x)}{dx} = -\frac{\beta_n}{\sqrt{\alpha_r}}\sin\left(\frac{\beta_n}{\sqrt{\alpha_r}}x\right) \quad (3.161)$$

$$\psi_{rn}^{'}(x) = \frac{d\psi_{rn}(x)}{dx} = \frac{\beta_n}{\sqrt{\alpha_r}}\cos\left(\frac{\beta_n}{\sqrt{\alpha_r}}x\right). \quad (3.162)$$

Eqs. (3.157)-(3.160) can be collected in matrix form.

$$\begin{bmatrix} \phi_{1n}^{'}(x_1) & \psi_{1n}^{'}(x_1) & 0 & 0 \\ \frac{-k_1^{1D}}{h}\phi_{1n}^{'}(x_2) - \phi_{1n}(x_2) & \frac{-k_1^{1D}}{h}\psi_{1n}^{'}(x_2) - \psi_{1n}(x_2) & \phi_{2n}(x_2) & \psi_{2n}(x_2) \\ \frac{k_1^{1D}}{k_2^{1D}}\phi_{1n}^{'}(x_2) & \frac{k_1^{1D}}{k_2^{1D}}\psi_{1n}^{'}(x_2) & -\phi_{2n}^{'}(x_2) & -\psi_{2n}^{'}(x_2) \\ 0 & 0 & \phi_{2n}(x_3) & \psi_{2n}(x_3) \end{bmatrix} \begin{bmatrix} C_{1n} \\ D_{1n} \\ C_{2n} \\ D_{2n} \end{bmatrix} = \begin{bmatrix} 0 \\ 0 \\ 0 \\ 0 \end{bmatrix} \quad (3.163)$$

In order for the solution to be non-trivial, the determinant of the matrix in Eq. (3.163) should be zero. By equating the determinant of the matrix to zero, the eigenvalues β_n are determined.

The coefficients C_{rn} and D_{rn} are found in terms of one of them. A simple method to find the coefficients is presented here. First, D_{1n} is expressed using Eq. (3.157) as

$$D_{1n} = -\frac{C_{1n}\phi_{1n}^{'}(x_1)}{\psi_{1n}^{'}(x_1)}. \quad (3.164)$$

Taking the leftmost boundary x_1 as the origin ($x_1 = 0$), D_{1n} simplifies to

$$D_{1n} = 0. \quad (3.165)$$

In this case, C_{2n} and D_{2n} can be found from Eqs. (3.159) and (3.160) as

$$C_{2n} = \frac{C_{1n}\left(k_1^{1D}/k_2^{1D}\right)\phi'_{1n}(x_2)\psi_{2n}(x_3)}{\phi'_{2n}(x_2) - \psi'_{2n}(x_2)\phi_{2n}(x_3)} \tag{3.166}$$

$$D_{2n} = \frac{C_{1n}\left(k_1^{1D}/k_2^{1D}\right)\phi'_{1n}(x_2)}{\psi'_{2n}(x_2) - \frac{\psi_{2n}(x_3)}{\phi_{2n}(x_3)}\phi'_{2n}(x_2)}. \tag{3.167}$$

Substituting the expressions for ϕ, ψ, ϕ' and ψ' from Eqs. (3.155), (3.156), (3.161) and (3.162), respectively, the following simplified expressions for C_{2n} and D_{2n} are obtained:

$$C_{2n} = \frac{C_{1n}\left(k_1^{1D}/k_2^{1D}\right)\left(\sqrt{\alpha_2/\alpha_1}\right)\sin\left(\xi_{1n}x_2\right)}{\cos\left(\xi_{2n}x_2\right) + \sec\left(\xi_{2n}x_3\right)\sin\left(\xi_{2n}x_2\right)} \tag{3.168}$$

$$D_{2n} = \frac{-C_{1n}\left(k_1^{1D}/k_2^{1D}\right)\left(\sqrt{\alpha_2/\alpha_1}\right)\sin\left(\xi_{1n}x_2\right)}{\cos\left(\xi_{2n}x_2\right) + \cot\left(\xi_{2n}x_3\right)\sin\left(\xi_{2n}x_2\right)} \tag{3.169}$$

Once the coefficients and the eigenvalues are found, as a next step, the following expression is obtained by using Eqs. (3.148) and (3.149) in Eq. (3.139).

$$\sum_{n=1}^{\infty} -\beta_n^2 X_{rn}(x)\Gamma_n(t) + \frac{\alpha_r}{k_r^{1D}} g_r(x,t) = \sum_{n=1}^{\infty} \frac{d\Gamma_n(t)}{dt} X_{rn}(x) \tag{3.170}$$

In order to solve Eq. (3.170) for the time-dependent function $\Gamma_n(t)$, the heat generation function $g_r(x,t)$ is expanded in infinite series of eigenfunctions.

$$\frac{\alpha_r}{k_r^{1D}} g_r(x,t) = \sum_{n=1}^{\infty} g_n^*(t) X_{rn}(x) \tag{3.171}$$

In order to find $g_n^*(t)$, the orthogonality property is used [57]. The orthogonality property for the time-dependent heat conduction problems can be expressed as

$$\sum_{r=1}^{2} \frac{k_r^{1D}}{\alpha_r} \int_{x_r}^{x_{r+1}} X_{rn}(x) X_{rm}(x) dx = \begin{cases} 0 & \text{for } n \neq m \\ N & \text{for } n = m \end{cases} \tag{3.172}$$

where

$$N = \sum_{r=1}^{2} \frac{k_r^{1D}}{\alpha_r} \int_{x_r}^{x_{r+1}} X_{rn}^2(x) dx. \tag{3.173}$$

By using this property, $g_n^*(t)$ is found as follows.

$$\sum_{r=1}^{2}\int_{x_r}^{x_{r+1}} g_r(x,t)X_{rn}(x)dx = \sum_{r=1}^{2}\frac{k_r^{1D}}{\alpha_r}\int_{x_r}^{x_{r+1}}\frac{\alpha_r}{k_r^{1D}}g_r(x,t)X_{rn}(x)dx \tag{3.174}$$

$$\sum_{r=1}^{2}\frac{k_r^{1D}}{\alpha_r}\int_{x_r}^{x_{r+1}}\left(\sum_{m=1}^{\infty}g_m^*X_{rm}(x)\right)X_{rn}(x)dx = \sum_{m=1}^{\infty}g_m^*\sum_{r=1}^{2}\frac{k_r^{1D}}{\alpha_r}\int_{x_r}^{x_{r+1}}X_{rm}(x)X_{rn}(x)dx = g_n^*(t)\sum_{r=1}^{2}\frac{k_r^{1D}}{\alpha_r}\int_{x_r}^{x_{r+1}}X_{rn}^2(x)dx, \tag{3.175}$$

which gives

$$g_n^*(t) = \frac{\sum_{r=1}^{2}\int_{x_r}^{x_{r+1}} g_r(x,t)X_{rn}(x)dx}{\sum_{r=1}^{2}\frac{k_r^{1D}}{\alpha_r}\int_{x_r}^{x_{r+1}}X_{rn}^2(x)dx}. \tag{3.176}$$

As the heat is generated solely on the microplate, it is customary to assume constant heat generation in region 1 and no heat generation in region 2, which yields

$$g_1(x,t) = g_1 \tag{3.177}$$

$$g_2(x,t) = 0, \tag{3.178}$$

leading to a simplification in Eq. (3.176) as

$$g_n^* = \frac{g_1\int_{x_1}^{x_2}X_{1n}(x)dx}{\sum_{r=1}^{2}\frac{k_r^{1D}}{\alpha_r}\int_{x_r}^{x_{r+1}}X_{rn}^2(x)dx}. \tag{3.179}$$

If we rewrite Eq. (3.170) by using Eq. (3.171), we obtain:

$$\sum_{n=1}^{\infty}\beta_n^2X_{rn}(x)\Gamma_n(t) + \sum_{n=1}^{\infty}g_n^*(t)X_{rn}(x) = \sum_{n=1}^{\infty}\frac{d\Gamma_n(t)}{dt}X_{rn}(x), \tag{3.180}$$

which can be simplified to the following ordinary differential equation

$$\frac{d\Gamma_n(t)}{dt} + \beta_n^2\Gamma_n(t) - g_n^*(t) = 0, \tag{3.181}$$

with the initial condition

$$\Gamma_n(0) = 0. \tag{3.182}$$

The solution of Eq. (3.181) is given by

$$\Gamma_n(t) = \frac{g_n^*}{\beta_n^2}\left(1 - \exp\left(-\beta_n^2t\right)\right). \tag{3.183}$$

Finally, by using Eq. (3.183) in Eq. (3.148), the closed form solution of $\theta_r(x,t)$ can be written as follows

$$\theta_r(x,t) = \sum_{n=1}^{\infty} \frac{X_{rn}(x) g_n^*}{\beta_n^2} \left(1 - \exp\left(-\beta_n^2 t\right)\right) \quad (r = 1, 2). \tag{3.184}$$

3.3.4 Calculation of Thermal Conductance

To calculate the thermal conductance, let us recall Eq. (2.25). In this equation, the thermal conductance G is defined as the total heat flow rate to the system (i.e. input power) divided by the area-averaged steady-state temperature difference on the microplate. The total heat flow rate is equal to the total heat generation rate in the microplate, and can be calculated from

$$Q = 2 g_1 L_1 W_1 Z. \tag{3.185}$$

Since in our model we assume that the temperature changes only in the x-direction, the area-averaged steady state temperature difference θ_{avg}^{SS} is equivalent to the length-averaged temperature difference.

$$T_{avg}^{SS} - T_s = \theta_{avg}^{SS} = \frac{\int_0^{L_1} \theta_1(x,\infty) dx}{L_1}, \tag{3.186}$$

and $\theta_1(x,\infty)$ can be found from Eq. (3.184) as

$$\theta_1(x,\infty) = \sum_{n=1}^{\infty} \frac{X_{1n}(x) g_n^*}{\beta_n^2}. \tag{3.187}$$

Therefore, θ_{avg}^{SS} can be found as

$$\theta_{avg}^{SS} = \frac{\sum_{n=1}^{\infty} \left(g_n^*/\beta_n^2\right) \int_0^{L_1} X_{1n}(x) dx}{L_1}. \tag{3.188}$$

Finally, using Eqs. (3.185), (3.186) and (3.187) in Eq. (2.25), the thermal conductance can then be expressed as follows

$$G = \frac{Q}{\theta_{avg}} = \frac{2 g_1 L_1^2 W_1 Z}{\sum_{n=1}^{\infty} (g_n^*/\beta_n^2) \int_0^{L_1} X_{1n}(x) dx}. \tag{3.189}$$

It should be noted that Eq. (3.189) is applicable to both shape-A and shape-B microbolometers. Since the composite region approximation does not depend on the position of the arm with respect to the microplate, the analysis developed in

Section 3.3.1 can be used indistinctively for both shapes. However, depending on the shape, the denominator of Eq. (3.189) will vary for each particular constriction resistance value. As shown in Section 3.3.2, the constriction resistances for the two shapes presented in this paper can be easily calculated from Eq. (3.138).

3.3.5 Calculation of Thermal Capacitance

According to Eq. (2.5), the thermal capacitance C can be expressed in terms of τ and G as

$$C = \tau G \tag{3.190}$$

In order to find C, the area-averaged temperature difference in the microplate as a function of time ($\theta_{avg}(t)$) should be determined. Similar to what was done in Eq. (3.186), $\theta_{avg}(t)$ can be found as

$$\theta_{avg}(t) = \frac{\int_0^{L_1} \theta_1(x,t)dx}{L_1}, \tag{3.191}$$

where $\theta_1(x,t)$ can be found from Eq. (3.184) ($r = 1$) as

$$\theta_1(x,t) = \sum_{n=1}^{\infty} \frac{X_{1n}(x) g_n^*}{\beta_n^2} \left(1 - \exp\left(-\beta_n^2 t\right)\right). \tag{3.192}$$

Substituting Eq (3.192) in Eq. (3.191), we obtain

$$\theta_{avg}(t) = \frac{\sum_{n=1}^{\infty} \left(g_n^*/\beta_n^2\right) \int_0^{L_1} X_{1n}(x)dx}{L_1} \left(1 - \exp\left(-\beta_n^2 t\right)\right). \tag{3.193}$$

The thermal time constant τ is the t value where $\theta_{avg}(t)$ reaches $\sim 63\,\%$ of its final value, therefore τ can be found from the plot of Eq. (3.193).

The exponential term in Eq. (3.193) is a summation of β_n^2 terms, which increase with increasing n, that is [57]

$$\beta_1 < \beta_2 < \beta_3 < \cdots < \beta_n < \ldots \tag{3.194}$$

It is therefore convenient to neglect the exponential component other than $\exp\left(-\beta_1^2 t\right)$, which simplifies Eq. (3.193) as

$$\theta_{avg}(t) = \left(1 - \exp\left(-\beta_1^2 t\right)\right) \frac{\sum_{n=1}^{\infty} \left(g_n^*/\beta_n^2\right) \int_0^{L_1} X_{1n}(x)dx}{L_1} \tag{3.195}$$

From Eq. (3.195), τ can be simply extracted as

$$\tau = 1/\beta_1^2 \tag{3.196}$$

Eq. (3.196) is a simpler way to find τ than plotting Eq. (3.193). Finally, C can be expressed as

$$C = G\tau = G/\beta_1^2, \tag{3.197}$$

which completes the calculation of thermal capacitance. The corresponding Matlab script that calculates the thermal conductance and capacitance using the proposed method is given in Appendix C.

3.4 Thermal Model for the Actuated State

In a tunable thermal conductance microbolometer, the values of the thermal parameters significantly change in the actuated state. This change stems from the new heat link formed by the contact of the microplate to the stoppers or the substrate. This new heat link becomes the dominant heat conduction mechanism, and its effect increases as the contact pressure increases by increasing the actuation voltage. The thermal conductance at the actuated state is mainly determined by the thermal contact conductance between the stoppers and the microplate. In this section, a thermal contact conductance model is utilized in order to estimate the thermal conductance at the actuated state.

When two solid bodies are put into contact, an imperfect joint is formed between them, which stems from the fact that the contacting surfaces are not perfectly smooth and flat. Therefore, as two solids contact, they touch only at a portion of the apparent contact area, forming microgaps between them. When heat is transferred across that contact, there is a temperature drop across it, which is called the joint resistance (R_j). The joint resistance is equal to three thermal resistances in parallel, given by

$$\frac{1}{R_j} = \frac{1}{R_c} + \frac{1}{R_g} + \frac{1}{R_r}, \tag{3.198}$$

where R_c is the contact resistance as the result of the heat conduction through the solid-solid microcontacts at the interface, R_g is the thermal resistance of the interstitial substance at the contact, and R_r is the resistance due to the radiation

across the microgaps. The heat conduction due to radiation is important only at interface temperatures higher than 600 K [46], and the thermal conduction through the gap is negligible in vacuum operation. Therefore for the test devices, both R_g and R_r approach infinity ($R_g \to \infty$ and $R_r \to \infty$), which makes the joint resistance equal to the contact resistance.

$$R_j = R_c \tag{3.199}$$

The thermal contact conductance h_c can be written in terms of R_c as

$$h_c = \frac{1}{R_c A_a}, \tag{3.200}$$

where A_a is the apparent contact area.

The thermal contact has been modeled for conforming (nominally flat) and nonconforming rough surfaces. Assuming that the microplate and the stoppers are horizontal upon contact, a conforming-rough contact model is implemented for the test structures. Various models have been developed for the contact between conforming-rough surfaces. Since it is not feasible to construct a general model based on the actual surface profile of the contact interface, statistical based approaches have been generally employed.

In most of the models available in the open literature, it is assumed that the surface asperities are distributed randomly over the contact area, and they have Gaussian height distributions about some mean plane passing through each of them. It is also assumed that the contact spots are approximately circular in shape. Due to the assumption that the asperities follow the Gaussian height distribution, these models are called fully Gaussian (FG) models. Fig. 3.17 shows an arbitrary cross-section of a contact, formed between two conforming rough surfaces. Each surface has a mean plane, and the distance between the mean planes is denoted by Y. The surface roughness and the absolute mean asperity slope are defined by σ and m, respectively, both of which can be determined from the surface profile data as

$$\sigma = \sqrt{\frac{1}{L}\int_0^L y^2(x)dx} \tag{3.201}$$

$$m = \frac{1}{L}\int_0^L \left|\frac{dy}{dx}\right| dx, \tag{3.202}$$

where $y(x)$ is the distance of the points on the surface from the mean plane, and L is the length of a trace. The contact between the rough surfaces can be transformed into a flat surface and a rough surface, where the effective roughness and

the effective absolute mean asperity slope are defined as

$$\sigma = \sqrt{\sigma_1^2 + \sigma_2^2} \tag{3.203}$$

$$m = \sqrt{m_1^2 + m_2^2}. \tag{3.204}$$

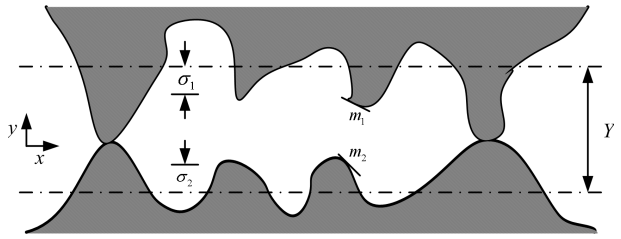

Figure 3.17: Schematic showing a small portion of a contact formed between two conforming rough surfaces.

Assuming the conforming rough surfaces are isotropic, the thermal contact conductance h_c between these contacting surfaces is given by [58]

$$h_c = \frac{2nak_s}{\left(1 - \sqrt{A_r/A_a}\right)^{1.5}}, \tag{3.205}$$

where

n	contact spot density;
a	contact spot radius;
A_r	real contact area;
A_a	apparent contact area;
k_s	the effective thermal conductivity of the joint.

When two different materials come into contact, k_s equals the harmonic mean of the thermal conductivities of the contacting materials. Since both the stopper and microplate material are polysilicon in our case,

$$k_s = k_{PolySi}. \tag{3.206}$$

The contact parameters n, a and A_r depend on the relative mean plane separation, which is defined as

$$\lambda = Y/\sigma. \tag{3.207}$$

To calculate λ, one should know how the asperities deform. The three modes of deformation of the contacting asperities are:

- Plastic deformation of the softer contacting asperities,
- Elastic deformation of all contacting asperities,
- Elastic and plastic deformation of the softer contacting asperities.

It has been reported that for surfaces that exhibit low σ/m, elastic deformation is dominant [59]. Since the test structures are fabricated by microfabrication systems that can produce films with very high smoothness, they are expected to show very low σ/m values. In addition, the contact pressure is expected to be very low. The contact geometric parameters in the case of elastic deformation of contacting asperities, according to the fully Gaussian model developed by Mikic are [60]

$$\frac{A_r}{A_a} = \frac{1}{4}\text{erfc}\left(\frac{\lambda}{\sqrt{2}}\right) \tag{3.208}$$

$$n = \frac{1}{16}\left(\frac{m}{\sigma}\right)^2 \frac{\exp\left(-\lambda^2\right)}{\text{erfc}\left(\lambda/\sqrt{2}\right)} \tag{3.209}$$

$$a = \frac{2}{\sqrt{\pi}}\frac{\sigma}{m} exp\left(\frac{\lambda^2}{2}\right)\text{erfc}\left(\lambda/\sqrt{2}\right) \tag{3.210}$$

and the relative mean plane separation is given by

$$\lambda = \sqrt{2}\text{erfc}^{-1}\left(4\text{P}/\text{H}_\text{e}\right). \tag{3.211}$$

In Eq. (3.211), P is the contact pressure and H_e is the elastic microhardness, defined as [60]

$$H_e = mE'/\sqrt{2} \tag{3.212}$$

and E' is the effective Young's modulus of the contacting asperities.

$$E' = \left(\frac{1-\nu_1^2}{E_1} + \frac{1-\nu_2^2}{E_2}\right)^{-1}, \tag{3.213}$$

where

E_1 and E_2	Young's modulus of contacting surfaces 1 and 2;
ν_1 and ν_2	Poisson's ratio of contacting surfaces 1 and 2.

For the test structures, both of the contacting surfaces are polysilicon, which yields

$$E' = \frac{E_{PolySi}}{2(1-\nu_{PolySi}^2)}. \tag{3.214}$$

In order to employ the contact conductance model explained above to the test devices, the surface roughness parameters (σ and m), and the contact pressure should be determined. σ and m can be found from the surface profile data, whereas an analytical expression should be employed for determining the contact pressure P, by using the electrostatic-structural model. The net force F_{net} acting on the microplate upon contact was previously given in Eq. (3.82) as

$$F_{net} = k_{eq}(g_0 - g) - \frac{\epsilon_0 A_{mp} V_{act}^2}{2g^2}, \tag{3.215}$$

where k_{eq} is the equivalent spring constant, g_0 is the initial gap thickness, and g is the final gap thickness. The contact pressure is found by dividing F_{net} by the apparent contact area A_a, which equals 272 μm^2 for design T80 and 408 μm^2 for design T120.

The thermal contact conductance h_c can be found if the surface roughness parameters (σ and m), and the contact pressure P is known. However, it was reported that at low contact pressures, the fully Gaussian models systematically underestimate the thermal contact conductance [59]. An explanation for this inaccuracy at low contact pressures is proposed by Milanez et al [61]. It was reported that the real surfaces may have Gaussian surface distribution up to around 4.5σ, however they generally do not have asperities whose height is above 4.5σ [61]. Therefore, the relative mean plane separation λ at low contact pressures is shorter than expected, and the contact conductance is greater than expected. As the contact pressure increases, more shorter asperities come into contact, which explains the accuracy of the fully Gaussian model at higher pressures.

As a solution to the inaccuracy of the fully Gaussian (FG) model, a truncated gaussian (TG) model was developed [61]. This model assumes that the heights of the surface asperities follow the Gaussian distribution up to a defined value of $z_{tr}\sigma$, where z_{tr} is the relative truncation level. The truncation level can be determined from the surface profile data. The asperity height distributions according to the FG model and the TG model are shown in Fig. 3.18(a) and (b), respectively. Based on this new distribution, the contact spot radius a and the relative mean plane

separation λ are given by [61]

$$a = \sqrt{1 - \frac{\operatorname{erfc}\left(\mathrm{z_{tr}}/\sqrt{2}\right)}{\operatorname{erfc}\left(\lambda/\sqrt{2}\right)}} \frac{2}{\sqrt{\pi}} \frac{\sigma}{m} exp\left(\frac{\lambda^2}{2}\right) \operatorname{erfc}\left(\lambda/\sqrt{2}\right), \tag{3.216}$$

$$\lambda = \sqrt{2}\, \operatorname{erfc}^{-1}\left(4\mathrm{P}/\mathrm{H_e} + \operatorname{erfc}\left(\mathrm{z_{tr}}/\sqrt{2}\right)\right). \tag{3.217}$$

The expressions for n and A_r/A_a are the same for both the FG and TG model. The expression for n does not change because according to the TG model, the surface asperities with relative heights below z_{tr} follow the Gaussian distribution, and there are no asperities higher than z_{tr}. The relative contact area A_r/A_a depends on the relative contact pressure, not on the geometry of the surface. Therefore, the expression for A_r/A_a does not require any change either.

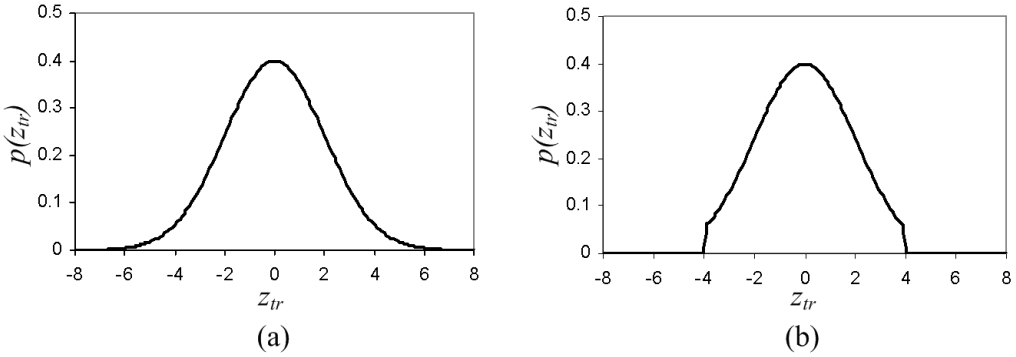

Figure 3.18: The surface asperity height distribution over the contact area, according to the (a) fully Gaussian and (b) truncated Gaussian model. The relative truncation level z_{tr} for the truncated Gaussian model is 4.

When Eq. (3.216), (3.217), (3.209) and (3.208) are substituted into Eq. (3.205), a final expression for h_c can be found. Since the final expression is difficult to manipulate, a simple correlation was developed [62]. For the elastic mode of deformation, the correlation can be expressed as

$$h_c = 1.25(m/\sigma)k_s(P/H_e)^{0.95}[1 + 1/f]^{0.9289}\sqrt{1 - 1/(1+f)}, \tag{3.218}$$

where

$$f = (P/H_e)\sqrt{2\pi}\, z_{tr} exp\left(z_{tr}^2/2\right). \tag{3.219}$$

Finally, the overall thermal conductance at the actuated state (G_{act}) is equal to the summation of the thermal conductance of the unactuated state (G_{unact}) and the

thermal contact conductance, which yields

$$G_{act} = G_{unact} + A_a h_c, \tag{3.220}$$

where G_{unact} can be found by using the composite region thermal model, given in Section 3.3. The thermal model for the actuated state is completed by Eq. (3.220). The validity of the model is verified with experimental data in Section 4.4.2.

3.5 Finite Element Modeling

The finite element model (FEM) of the fabricated devices was constructed using the commercial finite element analysis (FEA) software ANSYS, COMSOL and HFSS (High-Frequency Structural Simulator). The finite element analysis was undertaken to check the validity of the electrostatic-structural model, thermal model and infrared absorption model. Three finite element models were constructed: the actuator FEM, the thermal FEM and the infrared absorption FEM.

3.5.1 Actuator Finite Element Model

The actuator FEM models the movable microbolometer structure with the three-dimensional (3D) 20-node structural SOLID 95 element, and models the air/vacuum surrounding the structure with 3D electrostatic SOLID 122 element. The total number of elements is ∼70000 for design T80 and ∼110000 for design T120. Fig. 3.19 shows the finite element model for design T120 after meshing. The ESSOLV macro is used to perform a coupled electrostatic-structural solution. First, the electrostatic solver calculates the electric field in air, which depends on the potential difference between the microplate and the base plate. The electric field distribution is then postprocessed to find the nodal forces acting on the microbolometer. Then, the structural solver uses the force distribution as input and performs a structural solution to calculate the deflection of the microbolometer. By using the deflection data, the net force acting on the microbolometer is calculated. If the net force is greater than a predefined convergence value, the deflection data is updated and the net force is recalculated. This step continues until convergence is reached. Fig. 3.20 shows the deflection of design T120, when the actuation voltage is 9 V. In Fig. 3.20(a), the deflection contour intervals are auto-calculated by the finite

element analysis software, whereas in Fig. 3.20(b), the contour intervals are user specified, to check the uniformity of the detector plate. The ANSYS Parametric Design Language (APDL) code for the actuator FEM can be seen in Appendix D.

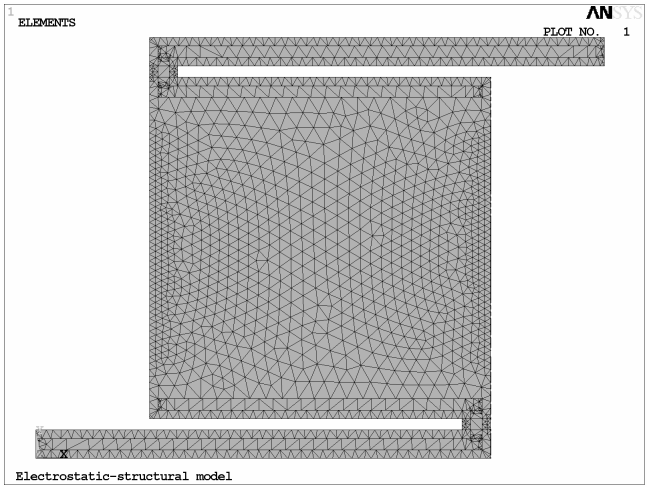

Figure 3.19: Graphic showing a model of design T120 for finite element simulation in ANSYS software, after meshing. The meshing of the surrounding air is not shown.

3.5.2 Thermal Finite Element Model

The aim of the thermal FEM is to find the temperature distribution on the microbolometer, based on the bias current. This way, two important tasks can be done:

- Calculation of thermal conductance and thermal capacitance,
- Calculation of the maximum bias current that can be applied safely without burning the device.

The thermal FEM is constructed using COMSOL Multiphysics. The analysis starts with the calculation of the potential distribution and the resistive heating, using the bias current value and resistivity of the elements. The resistive heating is then used to calculate the temperature distribution. Once the temperature distribution is found, the steady-state area-averaged temperature increase of the

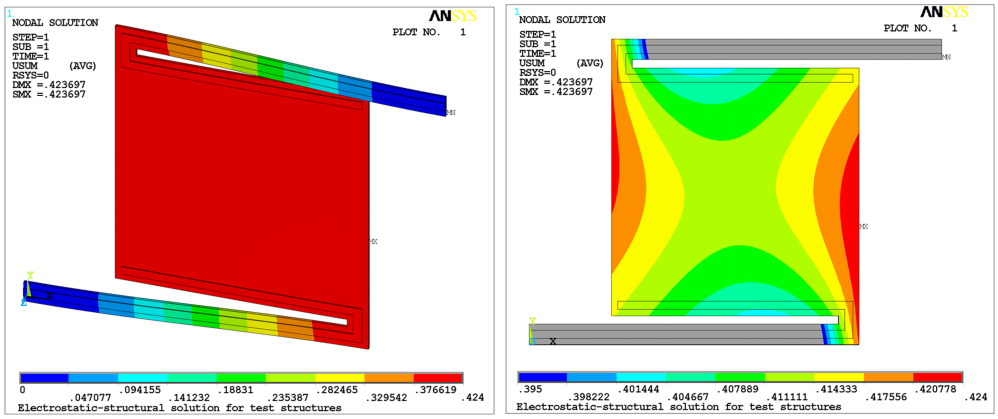

(a) (b)

Figure 3.20: The result of the finite element analysis, showing the deflection of design T120 structure, when the actuation voltage is 9 Volts. The deflection contour intervals are modified in (b), in order to observe the deflection within the microplate in more detail.

microplate (θ_{avg}^{SS}) is found, and the thermal conductance G is found by dividing the total generated heat to θ_{avg}^{SS} (recall Eq. (2.25)).

To find the thermal capacitance, the transient solver is employed, and $\theta_{avg}(t)$ is plotted as a function of time. From this plot, the thermal time constant τ is found and thermal capacitance is then determined by multiplying τ with G.

Determination of the safe bias currents is crucial to prevent burning of the devices due to overheating. A good example is shown in Fig. 3.21 where the temperature distribution of design T120 is plotted when the bias current is 10mA and 18mA. Since the melting point of gold is around 1300 K, the maximum safe bias current for this structure is around 18 mA.

3.5.3 Infrared Absorption Finite Element Model

The aim of constructing the IR absorption FEM is to validate the infrared absorption analytical model given in Section 3.2, and to observe how the layer properties and thicknesses affect the absorption of incident radiation of a specific wavelength.

The spectral response finite element analysis was made with the High Frequency Structural Simulator (HFSS), a commercial finite element method solver for electromagnetic structures, which is widely used for antenna design and radio fre-

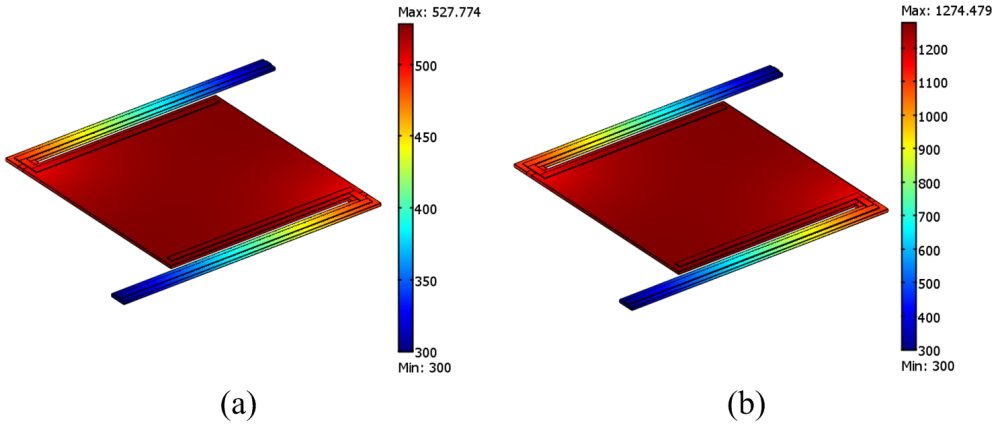

Figure 3.21: The temperature distribution of design T120, when the bias current is (a) 10 mA and (b) 18 mA.

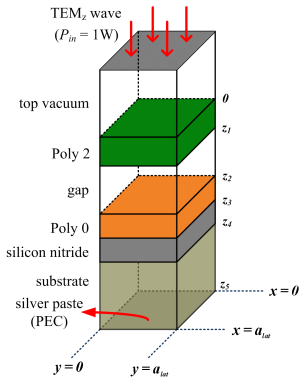

Figure 3.22: Schematic showing the geometry of the HFSS finite element model. Not drawn to scale.

quency (RF) electronic circuit design [63]. The geometry of the FEM is depicted in Fig. 3.22. A composite slab with a lateral length (a_{lat}) of 4 μm was constructed. On top of the microbolometer layers, an extra layer of vacuum was added (see top vacuum layer in Fig. 3.22). The thickness of this layer was chosen as 10 μm, but the thickness value does not have any effect on the results. This vacuum layer on top of the microbolometer is necessary in order to apply the incident infrared radiation properly from the top.

As shown in Section 3.2, the E-field, H-field and the propagation direction are perpendicular to each other. A TEM$_z$ wave (transmission electromagnetic wave propagating in z direction) with an average power of 1 W is applied to the top surface of the top vacuum layer. In order for our geometric model to support

a TEM_z wave, the boundaries perpendicular to the H-field direction should be perfect magnetic conductor (PMC), and the boundaries perpendicular to the E-field direction should be perfect electric conductor (PEC). Therefore, taking a_{lat} as the lateral length, the PMC condition is applied to the boundary planes $y = 0$ and $y = a_{lat}$, and, the PEC condition is applied to the boundary planes $x = 0$ and $x = a_{lat}$. The PEC condition is also applied to the bottom of the slab, which corresponds to the bottom of the substrate, painted with silver paste.

After prescribing the boundary conditions, the final geometry was meshed automatically by the software. Around 50000 tetrahedron elements were used for meshing the geometry. The simulations were then made using a parametric solver, by computing the field distribution as λ is varied. The results of the simulations, together with the results of the IR absorption model are presented in Section 4.3.

Chapter 4

Results and Discussion

In the previous chapter, an analytical model and a finite element model (FEM) for tunable thermal conductance microbolometers was presented. In this chapter, the analytical model is validated by experimental results and FEM simulations.

The chapter starts with the results of the optical profiler measurements (Section 4.1), which is crucial in determining the actual thin-film thicknesses, gap thicknesses and the surface roughness parameters. In Section 4.2, the results of the electrostatic-structural model are compared to the results of the actuator finite element model simulations and the electrical capacitance measurements. In Section 4.3, the infrared absorption model is compared to the results of the relevant finite element model previously described in Section 3.5.3. Based on the results, the effect of the microplate thickness and the gap thickness on the spectral absorption is discussed, which forms a basis for Chapter 5. In Section 4.4.1, the composite region thermal model is analyzed by comparing its results with the FEM simulations and the thermal conductance measurements of shape-A and shape-B devices having different microplate and arm dimensions. In Section 4.4.2, the results of the thermal conductance measurements of design T80 and T120 in the actuated and unactuated state are presented, and compared to the thermal contact model in order to analyze the thermal model for the actuated state. Finally in Section 4.5, the thermal capacitances of different shape-A and shape-B microbolometers calculated by the composite region thermal model are compared to the FEM simulations, to validate the thermal capacitance calculation method presented in Section 3.3.5. Concluding remarks are given at the end of the chapter.

4.1 Optical Profiler Measurements

An optical profiler is a non-contact measuring instrument that is used to measure a surface's profile. Compared to a contact profiler, an optical profiler is advantageous due to its high scan speed, reliability and small spot size [64]. The surface profiles of the test structures were captured by a WYKO NT100 Optical profiler, manufactured by Veeco Metrology, Inc [65].

The surface profiles of the test structures were used in determining the following parameters:

- The actual thin-film thicknesses of the test structures (Poly 0, Poly 1, Poly 2, and gold)
- The gap between the microplate and the base plate in the unactuated state (g_0) and the actuated state ($g_{contact}$)
- The effective surface roughness parameters (σ and m)
- The surface truncation parameter (z_{tr})

Fig. 4.1 shows the 3D profile of design T80 and design T120, for visual purposes. The gap and the thickness measurements were made by analyzing the X and Y profile data. The X and Y directions for design T80 and design T120 can be seen in the 3D profile images (Fig. 4.1(a) and (b)).

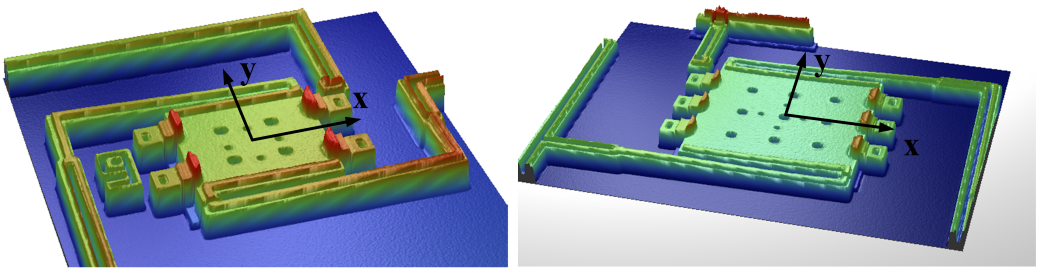

(a) (b)

Figure 4.1: 3D image of (a) design T80 and (b) design T120, created by WYKO NT100 Optical Profiler.

The X and Y profiles of design T80 and design T120 in the unactuated state are shown in Fig. 4.2. The average vertical distance between the top of the microplate

and the top of the silicon nitride layer was measured as 4.6 μm for both designs, in both X and Y directions. This distance is equal to the summation of three terms:

$$4.6\,\mu m = Z_{Poly0} + g_0 + Z_{Poly2}, \tag{4.1}$$

where Z_{Poly0}, g_0 and Z_{Poly2} are the Poly 0 (base plate), gap, and the Poly 2 (microplate) thicknesses, respectively. The Poly 0 and Poly 2 thicknesses are measured as 0.6 μm and 1.3 μm, which gives

$$g_0 = 2.7\,\mu m. \tag{4.2}$$

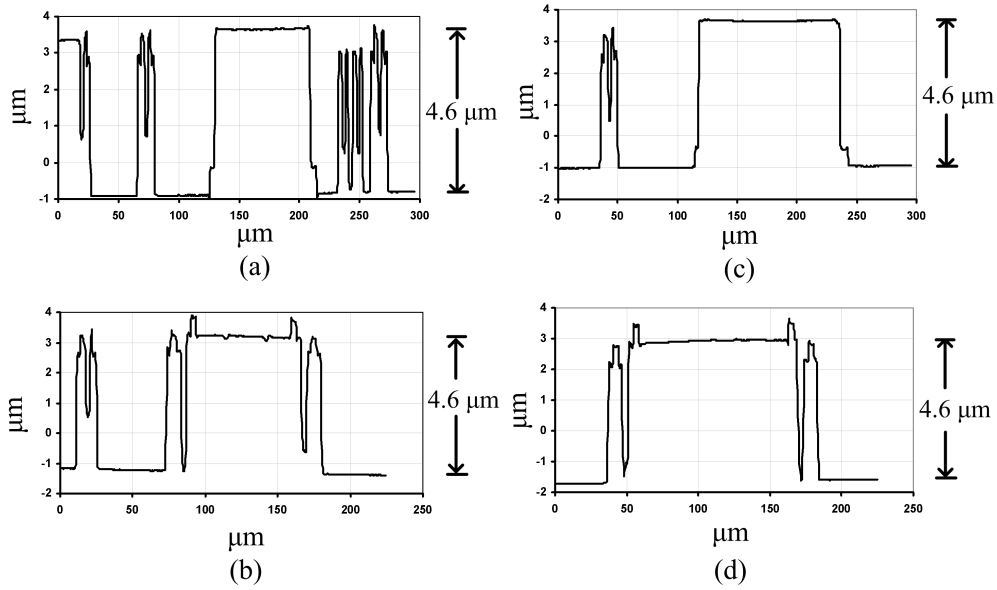

Figure 4.2: Profile of the design T80 and design T120 in the unactuated state: (a) X profile of design T80, (b) Y profile of design T80, (c) X profile of design T120, (d) Y profile of design T120

In Fig. 4.3, the X and Y profile of design T80 and design T120 are plotted at contact state. The height difference between the top of the microplate and the top of the nitride layer is measured as 3.6 μm. Similarly to Eq. (4.1), this height difference is equal to the summation of three terms:

$$3.6\,\mu m = Z_{Poly0} + g_{contact} + Z_{Poly2}. \tag{4.3}$$

Using the values $Z_{Poly0} = 0.6\,\mu m$ and $Z_{Poly2} = 1.3\,\mu m$, $g_{contact}$ can be found as

$$g_{contact} = 1.7\,\mu m. \tag{4.4}$$

Compared to the gap thickness in the unactuated state (2.7 μm), Eq. (4.4) shows that there is a clear decrease in the gap, which validates that the microplate is properly actuated. As the actuation voltage is increased further, the gap thickness does not decrease significantly (1.6 μm at 35 V), showing that the stoppers successfully prevent the microplate from deflecting further.

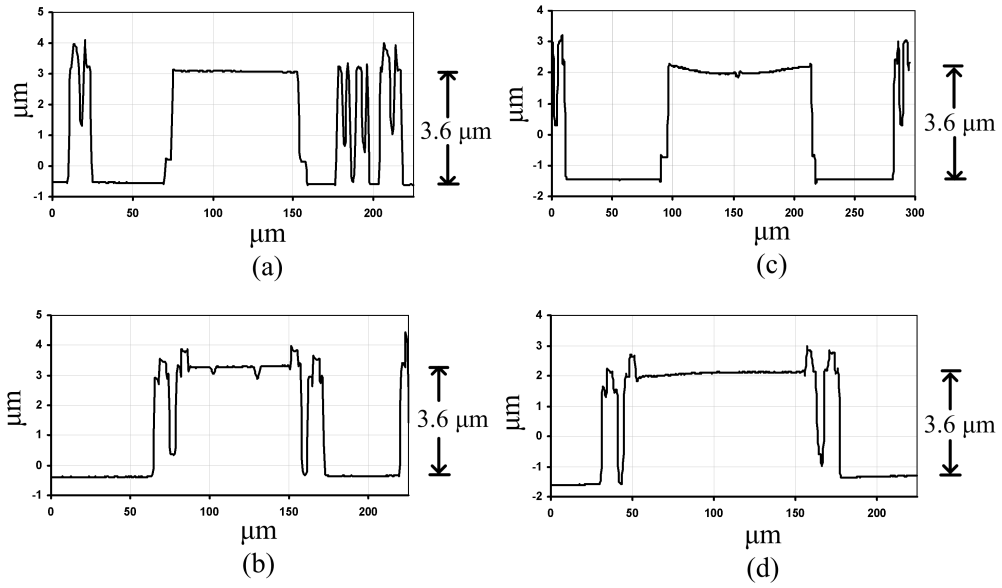

Figure 4.3: Profile of the design T80 and design T120 in the actuated state: (a) X profile of design T80, (b) Y profile of design T80, (c) X profile of design T120, (d) Y profile of design T120

Another method of showing the deflection of the microplate is to compare the arm profile in the unactuated state and in the actuated (contact) state. In Fig. 4.4, an arm profile of design T80 is plotted. In the unactuated state (Fig. 4.4(a)), the arm is slightly bent up (<100 nm), whereas at contact state (Fig. 4.4(b)) the arm is bent down (>800 nm), clearly showing the deflection of the microplate.

Finally, to calculate σ and m, the surface roughness of the contacting surfaces should be determined. taking the top surface of the stoppers (Poly 1) as surface 1, σ_1 and m_1 are calculated from the optical profiler data as $\sigma_1 = 12.14$ nm and $m_1 = 0.042$. The surface roughness parameters of the other contacting surface (σ_2 and m_2), which is the bottom surface of the Poly 2 microplate, cannot be directly measured by the optical profiler. In [66], the profile of the bottom surfaces of PolyMUMPs layers were captured with the help of microhinged flaps, and the

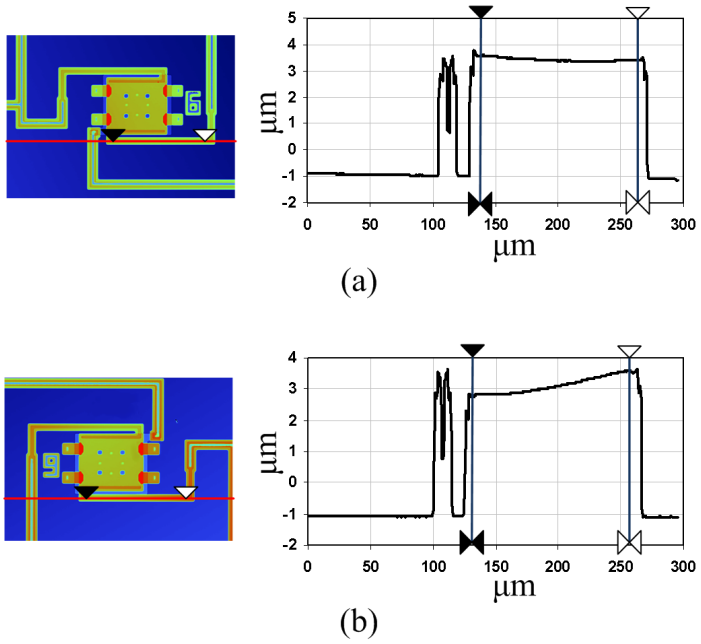

Figure 4.4: Profile of a design T80 arm at the (a) unactuated and (b) contact state. For both profiles, the profile is taken along the red lines on the left, between the white and black arrow.

roughness of the bottom surface of Poly 2 was found as 2.06 nm. Assuming $\sigma_2 =$ 2.06 nm, m_2 is estimated according to the intuitive formula $m_2 = m_1\,(\sigma_2/\sigma_1)$. Using these values, σ and m can be found using Eqs. (3.203) and (3.204) ($\sigma = 12.31$ nm, $m = 0.043$). The truncation level z_{tr} is determined by extracting the height of the highest asperity from the surface profile data and dividing it to the surface roughness, which yields $z_{tr} = 2.44$. The thicknesses and roughness parameters extracted from the optical profiler data are tabulated in Table 4.1.

The values in Table 4.1 are important, as they are used in all of the finite element models and the analytical models that calculate the contact voltage and the coupling efficiency η. In addition, the surface roughness parameters are required to calculate the thermal conductance in the actuated state.

4.2 Electrostatic-Structural Results

The validation of the electrostatic-structural model involves experimental measurement of the contact voltage of the test structures, design T80 and design T120. The

Table 4.1: The thicknesses and surface roughness parameters extracted from the optical profiler data.

Thicknesses (μm)		Roughness Parameters	
Poly 0	0.6	σ_1	12.14 nm
Poly 1	2.0	m_1	0.042
Poly 2	1.3	σ_2	2.06 nm [66]
Gold	0.5	m_2	0.007
Initial gap (g_0)	2.7	z_{tr}	2.44
Gap at contact ($g_{contact}$)	1.7		

measurement of the electrical capacitance C_{el} in terms of actuation voltage V_{act} (i.e. obtaining the C-V response) is a common and reliable method for determining the contact voltage [67]. The electrical capacitance of a parallel plate capacitor is given by [68]

$$C_{el} = \frac{\epsilon A_{mp}}{g}, \tag{4.5}$$

where ϵ is the permittivity of the medium between the parallel plates, A_{mp} is the plate area, and g is the thickness of the gap between the parallel plates. It is expected that g will decrease and C_{el} will gradually increase as the voltage between the parallel plates (V_{act}) is increased, At contact state, a sharp increase in C_{el} is expected due to the snap-down of the microplate onto the stoppers.

To obtain the C-V response, an Agilent E4890A Precision LCR meter was used. The LCR meter was connected to the test structures as shown in Fig. 4.5. To increase the accuracy of the measurement, the sample averaging mode was activated, so that each capacitance reading is the average of 32 samples, automatically calculated by the LCR meter. The sense voltage of the LCR meter is set to a sinusoid with a peak magnitude of 100 mV and a frequency of 1 MHz.

The C-V responses of the T80 and T120 designs are plotted in Fig. 4.6 and Fig. 4.7, respectively. When a number of C-V responses are recorded, the average contact voltage for design T80 is found as 10.8 V. Similarly, it is found that design T120 exhibits an average contact voltage of 10.2 V. As expected, for both devices, C_{el} increases gradually prior to the contact voltage, and a sudden increase is observed at contact state. As the actuation voltage is increased further, the increase in the capacitance becomes negligible, since the gap g does not change consider-

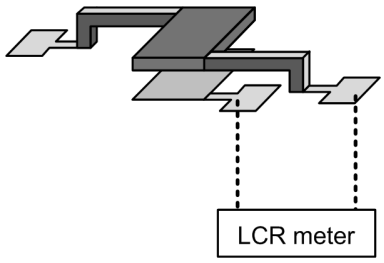

Figure 4.5: Experimental setup for electrical capacitance measurement.

ably after contact. This notion was also verified by the results of the optical profiler measurements in the previous section, where it was shown that for both designs, g changes only 0.1 μm as V_{act} is increased from the corresponding contact voltage to 35 V. The actuation voltage was not increased to above 35 V, to prevent failure due to overheating.

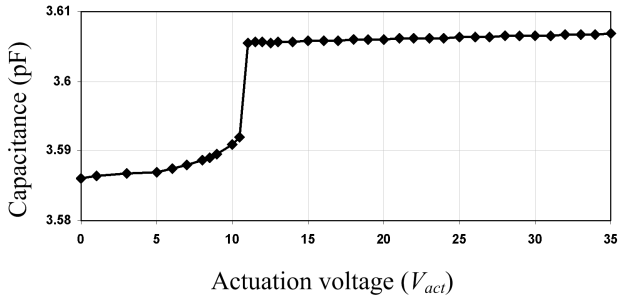

Figure 4.6: C-V response of a design T80 structure, measured by the LCR meter.

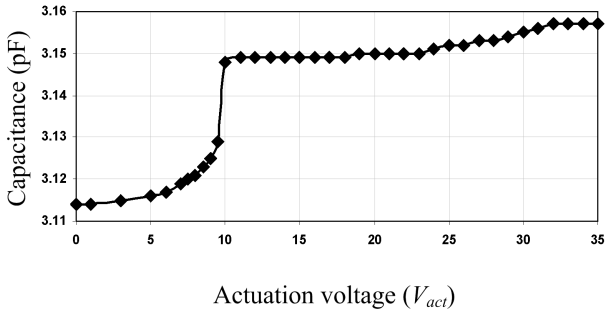

Figure 4.7: C-V response of a design T120 structure, measured by the LCR meter.

The contact voltages found by the electrostatic-structural model and the actuator finite element model are tabulated together with the measured contact voltages in Table 4.2. The Young's modulus and Poisson's ratio of polysilicon and gold used

Table 4.2: The contact voltages of design T80 and design T120.

	Design T120	Design T80
Model	10.5 V	14.5 V
FEM	11 V	13.4 V
Measured	10.2 V	10.8 V

Table 4.3: The mechanical properties of gold and polysilicon, used by the electrostatic-structural model and the actuator FEM.

Parameter	Value
E_{gold} (GPa)	77.2 [69]
E_{Poly2}(GPa)	158 [2]
ν_{gold}	0.42 [69]
ν_{Poly2}	0.22 [2]

by the analytical and finite element model are tabulated in Table 4.3. From the tabulated results, it can be inferred that the finite element model calculates the contact voltage with a discrepancy of 7.8 % for design T120 and 24.1 % for design T80, and the theoretical model calculates the contact voltage with a discrepancy of 2.9 % for design T120 and 34.3 % for design T80. The other parameters used in the calculation of contact voltage by the electrostatic-structural model are presented in Appendix E.

As can be seen from the results, both the electrostatic-structural model and the FEM overestimate the contact voltage for both structures. The possible reasons of this overestimation are stated below:

- The effect of the stoppers on the electrostatic force are not considered in the analytical and the finite element (FE) models. The stoppers are conducting structures, located between the base plate and the microplate. As can be seen from Fig. 4.8, the presence of stoppers decreases the effective gap distance between the microplate and the base plate, which therefore increases the electrostatic force acting on the microplate, resulting in a lower contact voltage than expected.

- The molecular adhesion forces between the stoppers and the microplate are not taken into account. As the gap between the stoppers and the microplate

decreases, the molecular attraction forces become more effective, and these forces may result in a lower contact voltage than expected.

- Underetching of the sacrificial oxide can be another reason for the inaccuracy. Since there is no direct method of determining the actual gap between the microplate and the base plate/stoppers, it is assumed that the oxide layer in between is completely etched. However, there may be residual oxide between the microplate and the base plate, which may decrease the effective gap size.

- Inaccuracies in the spring constant calculation also affect the calculated contact voltage. In both the analytical and the FE models, it is assumed that the arms are straight, i.e. they are neither curved down nor curved up. However, it was found from the optical profiler data that the arms are slightly curved up due to the residual stresses, so that the arm-microplate connection is around 100 nm higher than the arm-substrate connection. In addition, it is assumed that the stress strain relationship is completely linear, and the nonlinear effects are not taken into account. All these reasons lead to inaccuracies in the mechanical stiffness of the microbolometer arms.

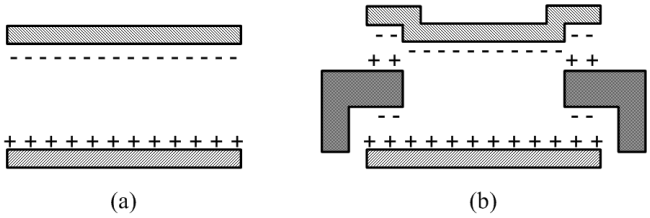

Figure 4.8: The effect of stoppers on charge distribution: (a) the device without stoppers (the analytical and FE models), (b) the actual device.

In order to observe the effect of the stoppers on the contact voltage, the C-V response of a device without stoppers is measured and plotted in Fig. 4.9. The device has been fabricated in the same batch using PolyMUMPs, and has the same geometry as design T80, except for the stoppers. As can be seen from Fig. 4.9, the contact voltage of the device without stoppers is roughly 13 V, which is significantly higher than that of design T80 and design T120, clearly showing the effect of stoppers on contact voltage. From the optical profiler measurements, it was found that the thin-film and initial gap thicknesses does not change without the presence of stoppers. Therefore, the above mentioned effects, such as the molecular adhesion

forces and the effect of stoppers on electrostatic forces are the main reasons of the discrepancy between the measured and calculated contact voltages.

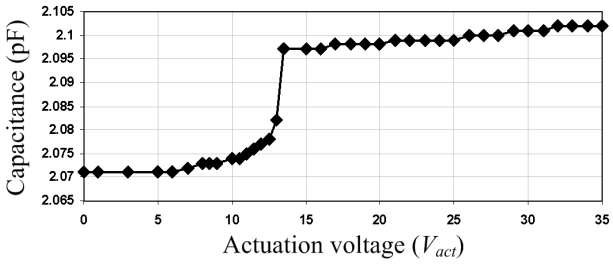

Figure 4.9: C-V response of a device that does not have stoppers.

Finally, it should be noted that the capacitance values in the C-V responses do not correspond to the net capacitance between the parallel plates, which is due to the parasitic capacitances present in the system. However, the parasitic capacitance does not change considerably with the applied voltage, therefore the contact voltage can still be measured accurately.

4.3 Infrared Absorption Results

In this section, the infrared absorption model presented in Section 3.2 is validated by the finite element model explained in Section 3.5.3, and the effect of the microplate thickness and the gap thickness on coupling efficiency η is investigated. The relative permittivity (ϵ_{r_n}), conductivity (σ_n) and the thickness values used in the calculations and simulations are tabulated in Table 4.4.

As can be recalled from Section 3.2, two analytical models are constructed for estimating the coupling efficiency. The first model, given by Eq. (3.113), is based on the assumption that the IR power is absorbed only by the microplate, and calculates η from the overall reflection coefficient. On the other hand, the second model, given by Eq. (3.123), calculates the power absorbed by the microplate using the complex Poynting vector.

These two absorption models (η and η') are compared to the FEM results (η_{FEM}), by plotting these at four different values of microplate (Poly 2) thickness in Fig. 4.10. In Fig. 4.10(a), the thickness of Poly 2 layer is at its actual value (1.3 μm), and the difference between η, η' and η_{FEM} is very small. As the microplate

Table 4.4: The relative permittivities (ϵ_{r_n}) and conductivities (σ_n) of the thin film layers of the fabricated PolyMUMPs test structures. These material properties are used by the infrared absorption model and the FEM to calculate the coupling efficiency.

n	Layer name	Thickness (μm)	ϵ_{r_n}	σ_n ($\Omega^{-1}\text{m}^{-1}$)
1	Poly 2	1.3	11.8 [70]	3.34×10^4 [2]
2	Gap	2.7	1	0
3	Poly 0	0.6	11.8 [70]	6.67×10^4 [2]
4	Si_3N_4	0.6	4 [45]	0
5	Substrate	500	11.8 [70]	100 [2]

Table 4.5: The average relative error of η and η' (ϵ_η and $\epsilon_{\eta'}$), with respect to the simulation results. The thickness of the Poly 2 layer is decreased from its actual value (1.3 μm) to 0.3 μm.

Z_{Poly2} (μm)	1.3	1.0	0.7	0.3
ϵ_η (%)	1.12	1.38	3.83	23.93
$\epsilon_{\eta'}$ (%)	1.53	1.28	0.91	4.99

thickness is decreased from 1.3 μm (Fig. 4.10(a)) to 0.3 μm (Fig. 4.10(d)), the difference between η and η_{FEM} increases. It is intuitive that the power absorbed at a lossy layer decreases as that layer gets thinner. Thus, the power absorbed in the Poly 2 layer decreases as its thickness Z_{Poly2} is decreased. In addition, more power is transmitted through the Poly 2 layer, resulting in a higher power absorption within other lossy layers, such as the substrate and the Poly 0 layer. Therefore, as the Poly 2 layer gets thinner, Eq. (3.113), which calculates η using the power absorbed by all lossy media, starts deviating from Eq. (3.123), which calculates η using the power absorbed by Poly 2 only. In Table 4.5, the average relative error of η and η' (ϵ_η and $\epsilon_{\eta'}$), with respect to η_{FEM} are tabulated, for four different Z_{Poly2} values, clearly showing the good agreement between η' and η_{FEM}.

Furthermore, to visually verify the absorption of the incoming IR radiation by the other layers as the Poly 2 layer gets thinner, the E-field distribution on the plane $x = a_{lat}$, computed by FEM simulations, is plotted for two different Poly 2 thickness: $Z_{Poly2} = 1.3\,\mu$m (Fig. 4.11) and $Z_{Poly2} = 0.7\,\mu$m (Fig. 4.12). In both of these cases, the E-field within the top vacuum portion of the slab is periodic,

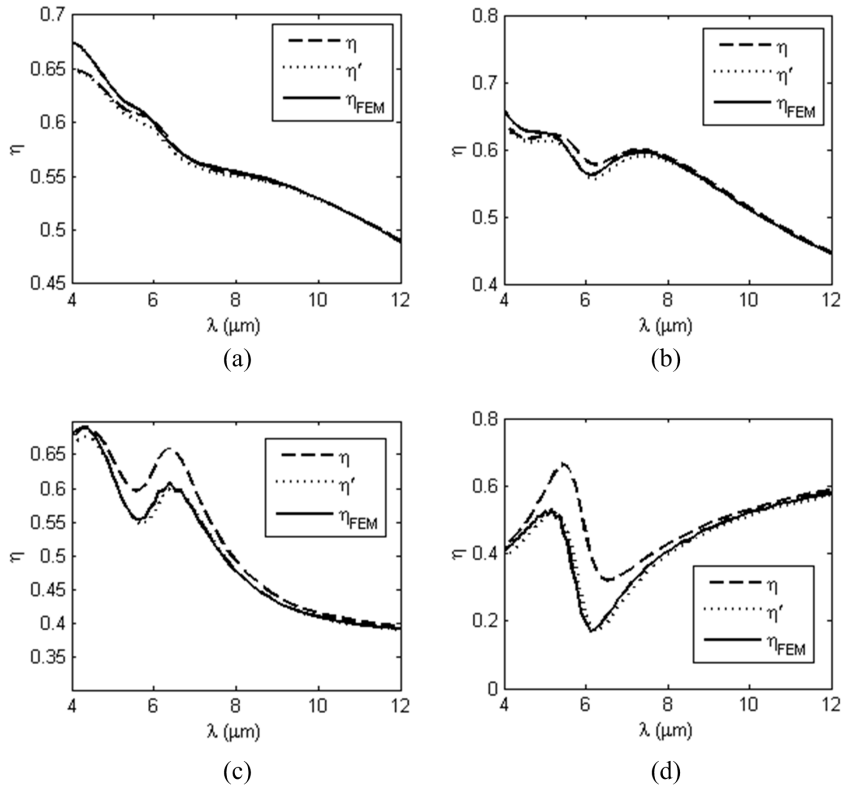

Figure 4.10: The plot of η (Eq. (3.113)), η' (Eq. (3.123)) and η_{FEM}, as the Poly 2 layer thickness Z_{Poly2} is taken as (a) 1.3 μm, (b) 1.0 μm, (c) 0.7 μm and (d) 0.3 μm.

which shows that the incident wave is partly reflected back from the Poly 2 surface, resulting in a standing wave within the top vacuum layer. In Fig. 4.11, the E-field penetrating into the Poly 2 layer attenuates to its lowest value within this layer, which means the wave is totally absorbed in the Poly 2 layer. On the other hand, in Fig. 4.12, the wave penetrating into Poly 2 layer is not totally absorbed within that layer, which can be inferred from the non-zero value of the E-field within the gap. Therefore, Eq. (3.123) is a better estimate for coupling efficiency as Z_{Poly2} is decreased.

Finally, the effect of actuation on the spectral response is analyzed. Taking g as the gap thickness, FEM simulations were made when the microbolometer is in its unactuated state ($g = g_0 = 2.7\,\mu$m) and when it is actuated ($g = g_{contact} = 1.7\,\mu$m)[1]. The FEM results comparing these two cases are plotted in Fig. 4.13. The average

[1]The g values are taken from the optical profiler results, given in Section 4.1

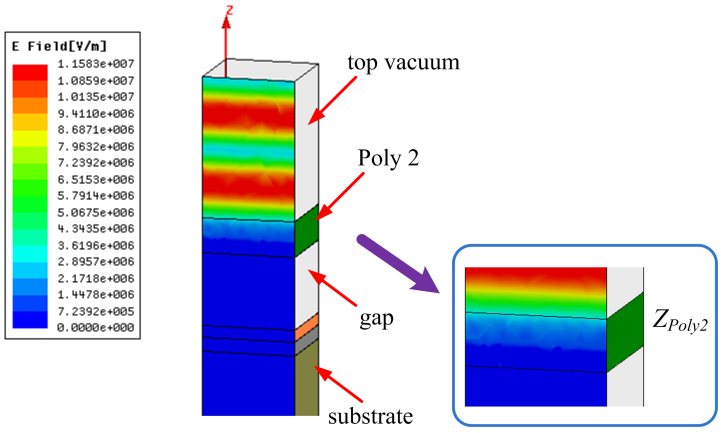

Figure 4.11: Schematic showing the magnitude of the complex E-field vector at $x = a_{lat}$ plane, when $\lambda = 6\,\mu$m and $Z_{Poly2} = 1.3\,\mu$m. The absorption can be observed from the decay of the E-field at the microplate layer.

absolute discrepancy between the solid curve and the dashed curve in Fig. 4.13 is calculated as 0.317 %, which leads us to the conclusion that the change of g due to thermal conductance tuning has a negligible effect on the absorption spectrum. However, if a state-of-art microbolometer is considered instead of a PolyMUMPs test structure, the deflection of the microplate can considerably affect the absorption spectrum. This situation is analyzed in Chapter 5.

4.4 Thermal Conductance Results

In this section, the thermal conductance results found using the thermal model are compared to the existing thermal models, finite element model simulations and experiments. This section is divided into two sections. In Section 4.4.1, the thermal conductance in the unactuated state is analyzed, and the effect of geometry (the microplate and the arm dimensions) and the pixel shape (shape-A and shape-B) are discussed (to recall shape-A and shape-B, refer to Fig. 3.10). In Section 4.4.2, the thermal conductance at the actuated state is analyzed, and the effect of the stopper mechanism on thermal conductance is discussed.

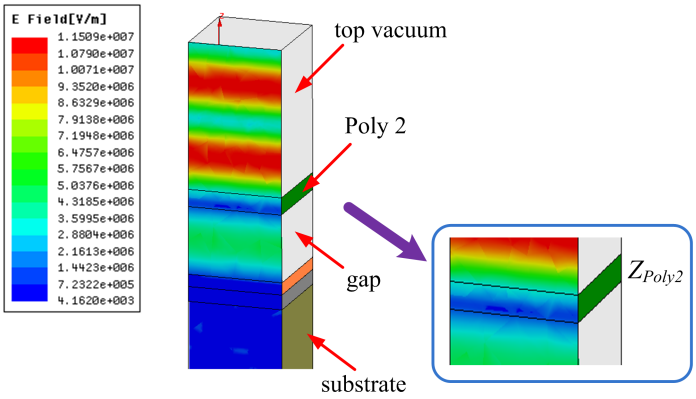

Figure 4.12: Schematic showing the magnitude of the complex E-field vector at the plane $x = a_{lat}$, when $\lambda = 6\,\mu$m and $Z_{Poly2} = 0.7\,\mu$m. The TEM wave is partly transmitted through the microplate, as can be observed from the non-zero value of the E-field within the gap.

4.4.1 Effect of Geometry

This section discusses the effect of microbolometer geometry on thermal conductance and compares the composite region thermal model presented in Section 3.3 to the experimental results, FEM results, and the conventional model given in Section 2.2.2.

In order to analyze the effect of geometry, various sizes of shape-A and shape-B structures are fabricated at MEMSCAP Inc. using PolyMUMPs run 78 [2]. Similar to design T80 and T120, the Poly 2 structural layer is used to form the arms and the microplate. The 0.5 μm thick gold layer is used to form the contact pads, electrical connections and the electrodes. The width of the Poly 2 layer that forms the arms is 10 μm, and the gold layer deposited on top of the Poly 2 layer is 4 μm. The microplate size varies from 40×40 μm^2 to 120×40 μm^2, the arm width varies from 10 μm to 16 μm, and the arm length varies from 40 μm to 80 μm, for shape-B structures. For shape-A structures, the arm width varies from 10 μm to 12 μm, while the microplate size and the arm length is kept constant. Unlike designs T80 and T120, the shape-A and shape-B structures do not include the stoppers and the base plate, since analyzing the effect of actuation is not the purpose of this analysis. The Scanning Electron Microscope (SEM) photo included in Fig. 4.14 shows two of the fabricated test pixels. It should be noted that these test structures are not expected to show good bolometric response and high infrared absorption, as they

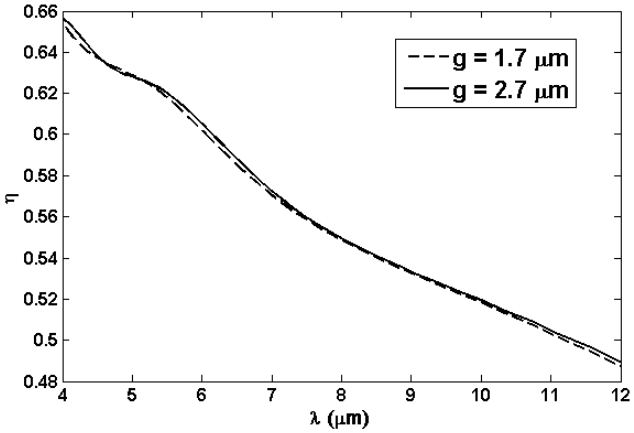

Figure 4.13: The spectral absorption at the unactuated state ($g = 2.7\,\mu$m) and at contact ($g = 1.7\,\mu$m), calculated by finite element analysis.

have been specifically fabricated to investigate the effect of geometry on thermal conductance.

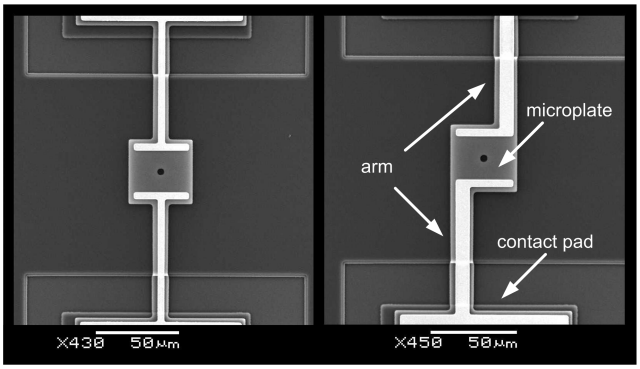

Figure 4.14: SEM image of a (a) shape-A and a (b) shape-B pixel. The microplates are 40 μm $\times$ 40μm and the arm lengths are 40 μm, for both of the structures. The arm widths are 10 μm and 16 μm for shape-A and shape-B pixels, respectively.

The experimental procedure is divided into two steps:

1. Measurement of the temperature coefficient of resistance (α)
2. Measurement of the thermal conductance (G)

The first step involves the measurement of electrical resistance R as a function of temperature T, and extraction of α from the T-R plot. For this test, a Poly 2

slab, anchored to the substrate, is placed in a temperature controlled environment. At each temperature step, the resistance is calculated using Ohm's Law. The T-R curve of this slab is plotted in Fig. 4.15. From the plot, α is found according to

$$\alpha = \frac{1}{R_0}\frac{dR(T)}{dT}, \tag{4.6}$$

which yields $-5.8 \times 10^{-4}\, K^{-1}$.

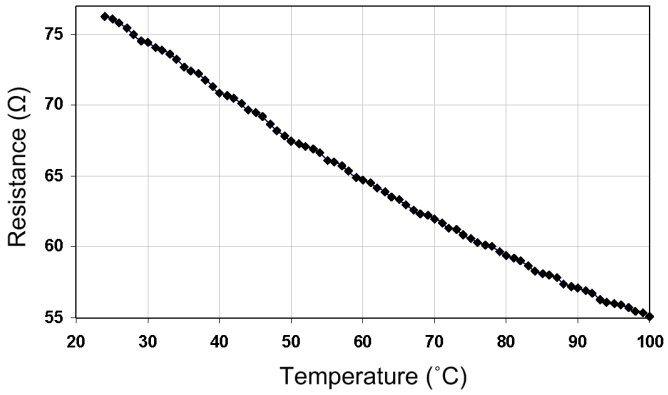

Figure 4.15: The T-R plot of a Poly 2 slab anchored to the substrate. α is estimated as $-5.8 \times 10^{-4}\, K^{-1}$, from this plot.

Once α is found, the thermal conductance is measured using the Joule heating method [44]. In this method, heat is generated by biasing the microplate with a voltage or current source under vacuum (<4 mTorr). By measuring the current at each voltage step, a plot of dissipated power versus resistance is obtained. For this measurement, a Keithley 2612 System Sourcemeter is used. The thermal conductance G is calculated from the slope of this curve, according to the following formula [71]

$$R = R_0 + \frac{1}{G} R_0 \alpha I^2 R, \tag{4.7}$$

where R_0 is the resistance at 300 K, and I is the current. Since α is negative, constant current biasing is used, in order to make the system stable. The results of the model are compared to the results of the composite region thermal model, the FEM and the conventional thermal conductance formula (Eq. (2.29)). The material properties for the polysilicon and gold films used in the analysis are listed in Table 4.6. The results, together with the geometric parameters of each test structure are tabulated in Table 4.7. The table shows the results for 10 structures, two of which

Table 4.6: Material properties of polysilicon and gold used for the analytical calculations and simulations.

Property	Value	Unit
Thermal conductivity of polysilicon	41 [72]	W/K
Thermal conductivity of gold	320	W/K
Specific heat capacity of polysilicon	753 [73]	$\mathrm{J\,kg^{-1}K^{-1}}$
Specific heat capacity of gold	129	$\mathrm{J\,kg^{-1}K^{-1}}$
Density of polysilicon	2330 [74]	$\mathrm{kg/m^3}$
Density of gold	19300	$\mathrm{kg/m^3}$
Resistivity of polysilicon	1.5×10^{-5}	$\Omega\,\mathrm{m}$
TCR (α) of polysilicon	-0.0058	$\mathrm{K^{-1}}$

are for shape-A and the rest are for shape-B. Emphasis is given to shape-B, as this shape is a more commonly used microbolometer pixel shape. It should be noted that in Table 4.7, W_2 pertains to the width of the polysilicon layer of the arm. The microplate width W_1 is 40 μm for all devices. The experimental results and the results of the composite region thermal model (Eq. (3.189)) are denoted by G_{exp} and G_{model}, respectively. Thermal conductances calculated by the finite element simulations are shown by G_{sim}, and the calculations using Eq. (2.29) are denoted as G_{conv}. The parameters ϵ_{model}, ϵ_{sim} and ϵ_{conv} are the percentage discrepancies of G_{model}, G_{sim} and G_{conv}, respectively, from the experimental results (G_{exp}).

As can be inferred from Table 4.7, for both shape-A and shape-B pixels, we can see that the proposed model matches well with the experimental data, whereas the conventional formula is close to the experimental data only for device 8, for which the arms are the longest. The greatest discrepancy between the conventional formulation and the experiments was found to be 43.1 % for the case in which the microplate length is 120 μm (device 10). This shows that the effect of the microplate on the thermal conductance becomes more important as the microplate becomes larger.

Table 4.7: Table showing the geometrical parameters of the test devices and results of the experiments (G_{exp}), proposed method (G_{model}), simulations (G_{sim}) and the conventional model (G_{conv}); and the percentage errors (ϵ_{model}, ϵ_{sim} and ϵ_{conv}). W_2 stands for the width of the polysilicon arm. The width of the gold layer on the arm is 6 μm less than the corresponding W_2.

Device no	shape	$2L_1$ (μm)	L_2 (μm)	W_2 (μm)	G_{exp} (W/K)	G_{model} (W/K)	G_{sim} (W/K)	G_{conv} (W/K)	ϵ_{model} (%)	ϵ_{sim} (%)	ϵ_{conv} (%)
1	A	40	40	10	5.22e-5	5.02e-5	5.43e-5	6.28e-5	-3.8	4	20.3
2	A	40	40	12	6.96e-5	6.53e-5	7.13e-5	8.49e-5	-6.2	2.4	22
3	B	40	40	10	4.72e-5	4.43e-5	5.03e-5	6.28e-5	-6.1	6.7	33.1
4	B	40	40	12	6.13e-5	5.71e-5	6.59e-5	8.49e-5	-6.9	7.5	38.5
5	B	40	40	14	7.66e-5	6.97e-5	8.12e-5	1.07e-4	-9	6.0	39.7
6	B	40	40	16	9.25e-5	8.25e-5	9.65e-5	1.29e-4	-10.8	4.3	39.5
7	B	40	60	10	3.42e-5	3.28e-5	3.62e-5	4.18e-5	-4.1	5.8	22.2
8	B	40	80	10	2.88e-5	2.60e-5	2.83e-5	3.14e-5	-9.7	-1.7	9.0
9	B	80	40	10	4.54e-5	4.18e-5	4.65e-5	6.28e-5	-7.9	2.4	38.3
10	B	120	40	10	4.39e-5	3.96e-5	4.38e-5	6.28e-5	-9.8	-2.3	43.1

For pixels of shape-B, the maximum discrepancy of the proposed model with respect to the experiments is observed for device 6 (around $-10.8\,\%$), which has the widest arms. One possible reason for this deviation is the decrease in the constriction resistance as the ratio of the arm width to the microplate width (W_2/W_1) increases. A similar behavior is observed for shape-A devices with the same microplate size (devices 1 and 2), for which wider arms result in higher discrepancies between the experiments and the composite region thermal model.

In addition to the thermal conductance analysis and for completeness, we have also compared the effect of the inclusion of constriction resistance estimation in the accuracy of the thermal conductance calculation. The results are shown in Figs. 4.16 and 4.17. In both figures, the solid lines show the results of the composite region approximation model, including the contact resistance R_c. The dashed lines show the composite region approximation model with a contact resistance equal to zero ($R_c = 0$), and the dotted lines show the thermal conductance calculated with the more conventional formula (Eq. (2.29)). Experimental and simulation results have also been included. From these two figures, it can be observed that the thermal conductance is overestimated when using Eq. (2.29) and when the proposed model does not take into consideration the constriction resistance. Thus, taking the constriction resistance estimation into account provides the closest match to the experimental results, both for shape-A and shape-B pixels.

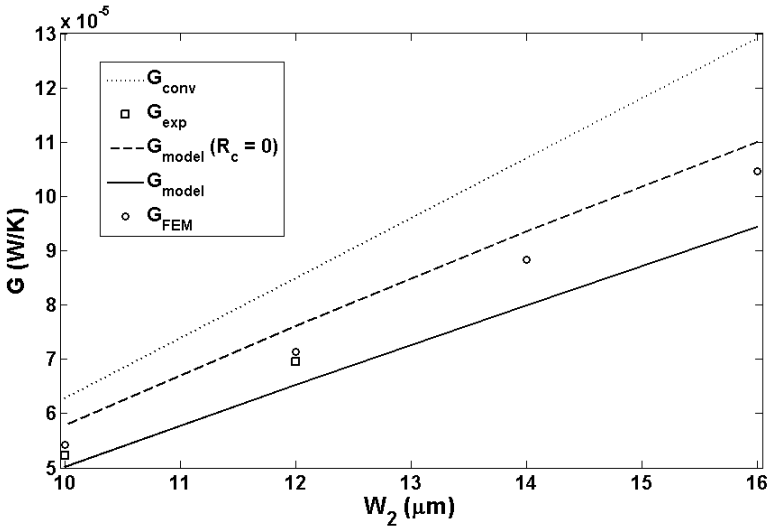

Figure 4.16: Plot showing the effect of constriction resistance for shape-A pixels.

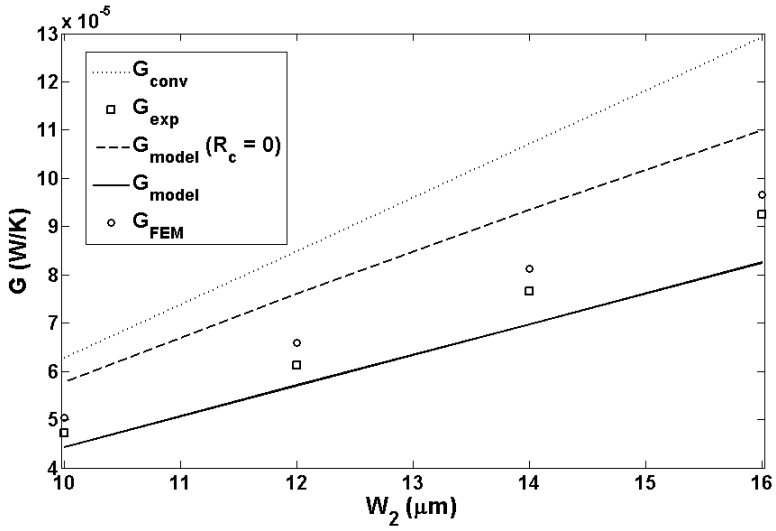

Figure 4.17: Plot showing the effect of constriction resistance for shape-B pixels.

4.4.2 Effect of Actuation

In this section, the proposed thermal conductance tuning mechanism is verified by measuring the thermal conductance of designs T80 and T120, as the actuation voltage is varied. The results are compared to the contact thermal resistance model, which was given in Section 3.4. The effect of stoppers on the operation and performance of the mechanism is also analyzed, by comparing the results of design T80 with a device that does not have stoppers.

The experimental procedure can be divided into two steps. In the first step, the temperature coefficient of resistance α is found. Similar to the previous section, the resistance of a Poly 2 slab, anchored to the substrate is measured in a temperature controlled environment. The T-R curve of this slab is plotted in Fig. 4.18. From this curve, α is estimated as $5.2 \times 10^{-4}\, K^{-1}$.

As the second step, the thermal conductance is found using the Joule heating method. The experimental setup is shown in Fig. 4.19. The bias voltage V_b is applied through the microbolometer arms, whereas the actuation voltage V_{act} is applied between the microplate and the Poly 0 base plate. At each value of V_{act}, V_b is gradually increased from zero to a final value, and a plot of dissipated power vs. resistance is obtained. Thermal conductance is then calculated from the slope of this curve, according to Eq. (4.7).

The power vs. resistance plot for designs T120 and T80 are shown in Figs. 4.20

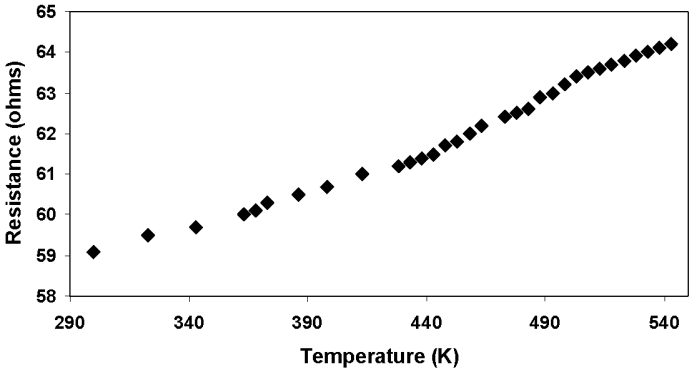

Figure 4.18: The T-R plot of a Poly 2 slab anchored to the substrate.

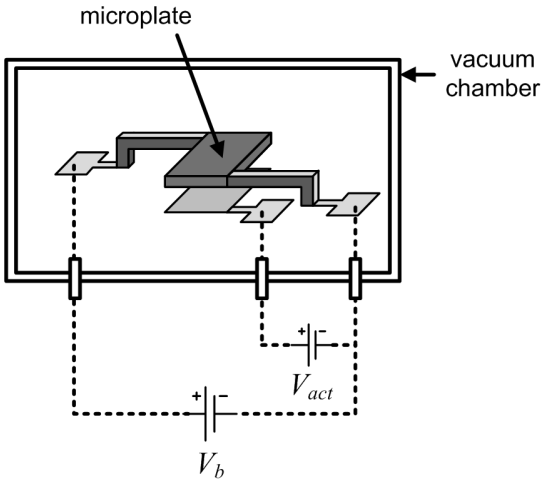

Figure 4.19: Experimental setup for thermal conductance measurement.

and 4.21, respectively. In the unactuated state of design T120, G is found to be 1.42×10^{-5} W/K. With an actuation voltage of 11 V, the thermal conductance increases to 3.36×10^{-5} W/K. As discussed previously, this increase in G is expected, due to the new heat links formed by the contact of the microplate to the stoppers. As the actuation voltage is further increased, the pressure of the microplate on the stoppers increases, resulting in higher thermal contact conductance (TCC). This explains the increase in thermal conductance to 4.85×10^{-5} W/K, with an actuation voltage of 35 V. The thermal conductance of design T80 shows a similar behavior to design T120. In the unactuated state, G is found to be 1.29×10^{-5} W/K. The contact state starts roughly occurs at 11 V, and at this voltage, G increases to 2.44×10^{-5} W/K. As the actuation voltage is further increased, the thermal

conductance increases as well (3.71×10^{-5} W/K at 35 V). After 35 V, both design T80 and T120 devices mostly failed by overheating.

In Figs. 4.22 and 4.23, the measured thermal conductance is plotted as a function of actuation voltage, together with the thermal model explained in Section 3.4. Let us rewrite Eq. (3.220) of the thermal model, the expression for thermal conductance in the actuated state:

$$G_{act} = G_{unact} + A_a h_c. \tag{4.8}$$

In Eq. (4.8), h_c is the thermal contact conductance and G_{unact} is the thermal conductance calculated by the composite thermal model given in Section 3.3. The parameters used in the calculation of h_c are given in tabular form in Table 4.8.

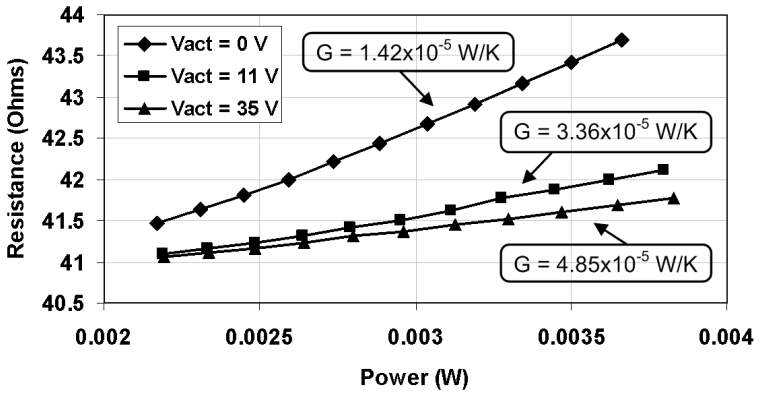

Figure 4.20: The power versus resistance plot of design T120. The top curve corresponds to the unactuated state ($V_{act} = 0$).

Table 4.8: The parameters of the thermal model for the actuated state.

Parameter	Unit	T80	T120
Thermal conductance before contact state (G_{unact})	W/K	1.29×10^{-5}	1.42×10^{-5}
Contact voltage ($V_{contact}$)	V	14.5	10.5
Equivalent spring constant (k_{eq})	N/m	1.5	2.4
Apparent contact area (A_a)	μm^2	272	408

As can be seen from Figs. 4.22 and 4.23, the thermal model shows a similar trend with the experiments, both in the unactuated state and after contact. However, it underestimates the measured thermal conductance, for both of the designs. The maximum discrepancy mostly occurs at the onset of contact, roughly at 11 V.

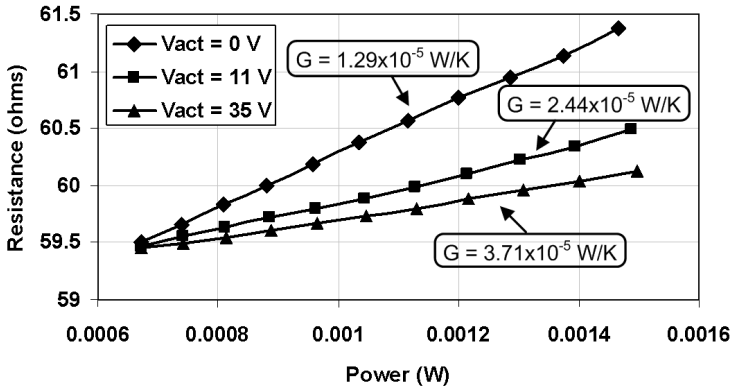

Figure 4.21: The power versus resistance plot of design T80. The top curve corresponds to the unactuated state ($V_{act} = 0$).

The underestimation of thermal conductance is mainly the result of the discrepancy between the calculated and measured contact voltage. As can be inferred from Table 4.2, both the analytical and finite element models overestimate the contact voltage. The overestimation of the contact voltage shows that there is an underestimation in contact pressure, which results in an underestimation in thermal conductance. In addition, the contact pressure calculation used in the thermal model does not consider the adhesion forces, which also contributes to the underestimation of contact pressure. In Fig. 4.24, the results for design T80 are compared to the thermal model, where the contact pressure is multiplied by a factor of two. The effect of contact pressure on thermal conductance is clearly seen in this plot. Another important reason for the discrepancy is the inaccuracy in the surface truncation parameter z_{tr}. As explained previously in Section 4.1, there is no way to record the surface profile of the actual contact area, i.e. the bottom of the Poly 2 microplate and the top of the Poly 1 stoppers. Therefore, the roughness parameters and the truncation parameter z_{tr} are found by profiling arbitrary chip surfaces. Since the overall contact area is very small, the actual roughness parameters of the contacting surfaces can be very different from the estimated values. In order to observe the effect of the roughness parameters and z_{tr} on surface roughness, the experimental results for design T80 are compared to the results of the model where z_{tr} is varied, in Fig. 4.25. As can be seen from this figure, even a small inaccuracy in roughness parameters may result in a significant change in G. Another reason for inaccuracy can be thermal radiation from the microplate. It was shown that at

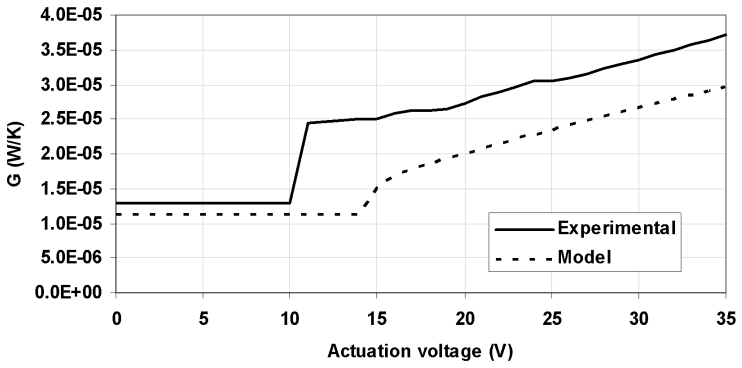

Figure 4.22: Thermal conductance versus actuation voltage plot of design T80. The solid curve corresponds to the experimental data and the dashed curve corresponds to the thermal contact model.

high microplate temperatures, radiation can be an important source of heat loss, and can considerably contribute to thermal conductance. From the experiments, it was found that most of the devices fail due to overheating, in the range 35-40 V, which means as V_{act} approaches 35 V, the increase in the microplate temperature may result in a raise in the measured thermal conductance, due to radiation. Since this effect is not considered in the thermal model, radiation based losses may be an important reason of inaccuracy in thermal conductance modeling, especially when V_{act} approaches 35 V. In addition, high temperature results in elongation of the microbolometer arms, and due to the mismatch in the thermal coefficient of expansion (TCE) of gold and polysilicon, this elongation results in an additional increase in the contact pressure, which further increases the thermal conductance.

In order to observe the effect of the stoppers on contact voltage and thermal conductance, we have plotted in Fig. 4.26 the thermal conductance (G) versus actuation voltage of design T80 compared to one that has the same geometry and has been fabricated in the same batch using PolyMUMPs, but does not have the stoppers. To avoid the electrical contact between the actuation terminals, the second structure is actuated by biasing the substrate, which is isolated from the surface structures by a 600 nm silicon nitride layer. Before contact state, both of the structures exhibit a constant thermal conductance (1.29×10^{-5} W/K for design T80 and 1.25×10^{-5} W/K for the device without stoppers). At the contact voltage, the thermal conductance of the structure without the stoppers jumps to 9.51×10^{-5}

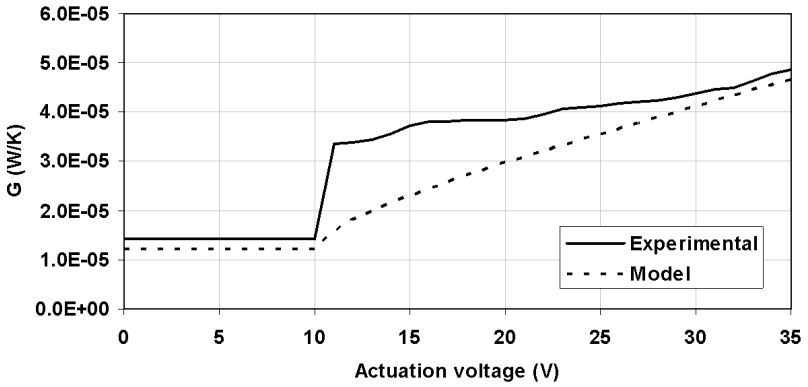

Figure 4.23: Thermal conductance versus actuation voltage plot of design T120. The solid curve corresponds to the experimental data and the dashed curve corresponds to the thermal contact model.

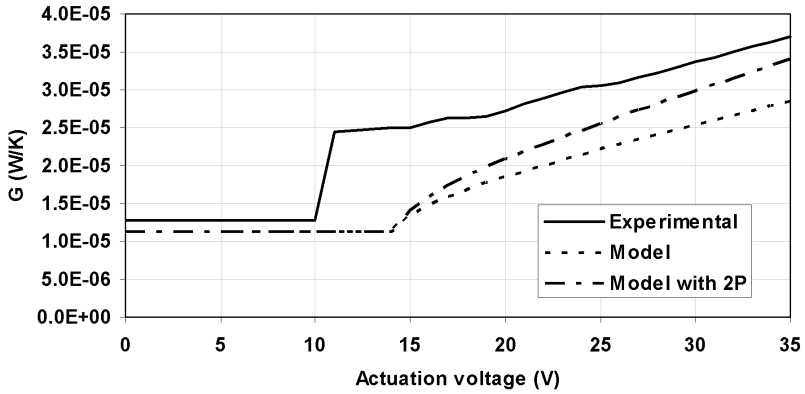

Figure 4.24: Plot showing the effect of contact pressure P on G. The solid curve corresponds to the experimental data, the dashed curve corresponds to the thermal contact model, and the dash-dotted curve corresponds to the thermal contact model where P is doubled.

W/K, whereas the thermal conductance of the other structure becomes 2.44×10^{-5} W/K. This is expected since at contact state the microplate of the structure with no stoppers snaps down to the substrate, resulting in a higher contact area than that of the structure with stoppers at the same voltage. In addition, at this same voltage and when the structure has no stoppers, the gap between the microplate and the substrate is smaller ($\sim 1.2\,\mu$m corresponding to the nitride and Poly 0 layers), resulting in a higher electrostatic attraction.

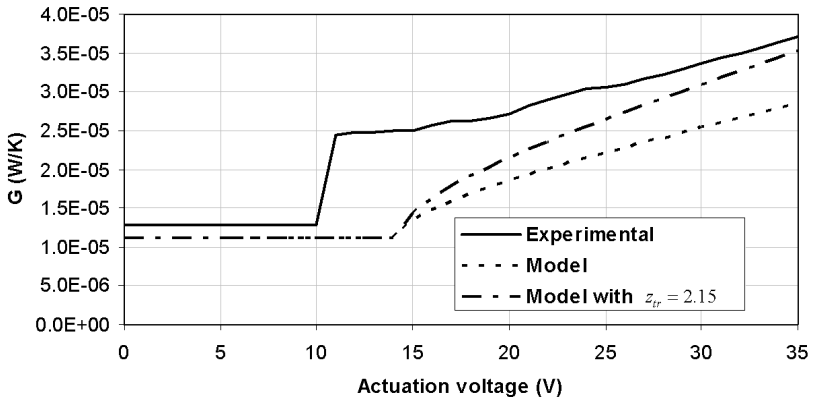

Figure 4.25: Plot showing the effect of z_{tr} on G. The solid curve corresponds to the experimental data, the dashed curve corresponds to the thermal contact model ($z_{tr} = 2.44$), and the dash-dotted curve corresponds to the thermal contact model with z_{tr} taken as 2.15.

From Fig. 4.26, we can also see that for the structure without stoppers, as the actuation voltage is increased, there is a small change in G of the structure without the stoppers (less than 0.3 %). Therefore, the thermal conductance can only be tuned to two different values, the one before, and the one after contact. In comparison, the G of the structure with stoppers increases linearly with increasing voltage, due to the increase in thermal contact conductance (TCC) between the stoppers and the microplate. This linear response gives a continuous tunability range and the ability to control the thermal conductance precisely. It should be also inferred from Fig. 4.26 that the contact voltage of the structure without the stoppers is measured to be higher than the one with the stoppers, which is evidence of the adhesion force between the stoppers and the microplate, resulting in a lower contact voltage.

As was mentioned before, a common problem that may arise during electrostatic actuation is the in-use stiction. Although the devices with stoppers are expected to exhibit low adhesion force due to their smaller contact area, in-use stiction is observed in the structures with stoppers (design T80 and T120), whereas no evidence of in-use stiction was observed in the structures without the stoppers. This is due to the fact that the stoppers limit the deflection of the microplate, which results in a restoring force less than the adhesion force, when the actuation voltage is removed. We believe that in order to avoid stiction, the stoppers need to

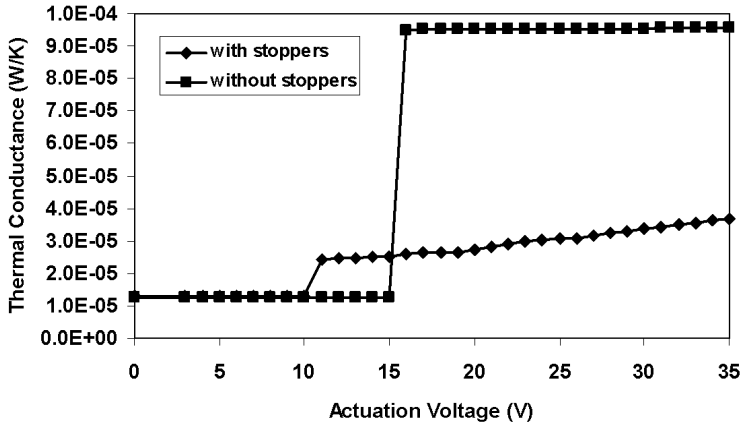

Figure 4.26: Plot comparing the thermal conductance of design T80 and a structure without stoppers, as a function of V_{act}.

be fabricated closer to the substrate. This way, the microplate will need to deflect more before contacting the stoppers, which in turn will increase the restoring force and easily bring the microplate to its original position as the actuation voltage is removed. Although this is not possible in PolyMUMPs, the stoppers can be fabricated closer to the base plate, by using a custom fabrication process.

4.5 Discussion on Thermal Capacitance

In this dissertation, emphasis is given to thermal conductance, and the thermal capacitance of the devices is not measured. However, the composite region thermal model, given in Section 3.3.5 provides a solution to the transient heat conductance equation, and therefore by calculating the thermal time constant, the thermal capacitance can be estimated (recall Eq. (3.197)). In this section, the thermal capacitance calculation by this equation is compared to the FEM simulations, and the two conventional formulas given in Section 2.2.1 (Eqs. (2.23) and (2.24)).

In Figs. 4.27, the percent error of the composite region thermal model (Eq. (3.197)) and two conventional models (Eqs. (2.23) and (2.24)) are plotted, as the arm width (W_2), arm length (L_2) and microplate length (L_1) are varied, respectively. The percent error ϵ is calculated based on the FEM simulation results.

As can be seen from the results, the composite region thermal model and the

modified conventional model (Eq. (3.197) and Eq. (2.24)) are in good agreement with the simulation results, whereas the conventional model (Eq. (2.23)) significantly deviates from the simulations. Both Eq. (3.197) and Eq. (2.24) estimate the thermal capacitance with very small error; therefore, both can be used for thermal capacitance estimation during the design stage. Another option can be using the arithmetic mean of Eq. (3.197) and Eq. (2.24), to estimate thermal capacitance.

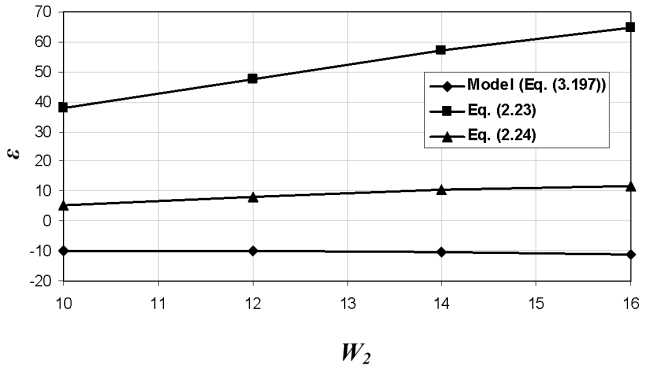

Figure 4.27: Plot showing the percentage error of Eqs. (2.23), (2.24) and (3.197), as W_2 is varied.

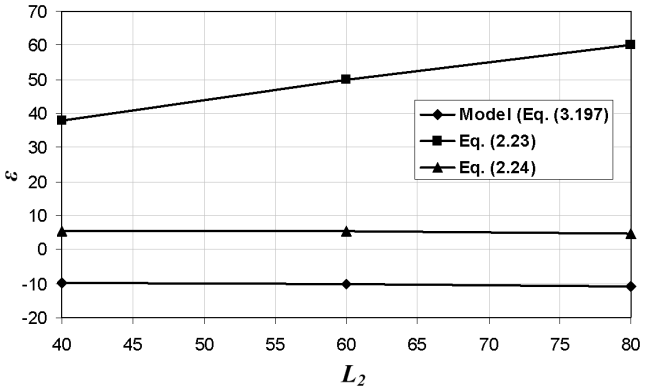

Figure 4.28: Plot showing the percentage error of Eqs. (2.23), (2.24) and (3.197), as L_2 is varied.

4.6 Conclusions

In this chapter, the microbolometer analytical models constructed for designs T80 and T120 are validated with the FEM simulations and experiments, which include

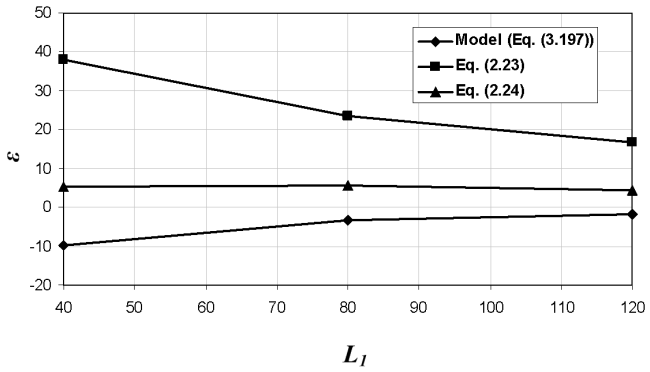

Figure 4.29: Plot showing the percentage error of Eqs. (2.23), (2.24) and (3.197), as L_1 is varied.

optical profiler, electrical capacitance and thermal conductance measurements.

As a result of the optical profiler measurements, the after-fabrication thicknesses and the surface roughnesses of the thin-film layers forming the test structures were found. In addition, by calculating the gap thickness before and after actuation, the operation of the actuation mechanism was verified.

The electrical capacitance measurements were beneficial for the validation of the contact voltages estimated by the electrostatic-structural model. It was found that the electrostatic-structural model estimates the contact voltage with a discrepancy of 2.9% for design T120 and 34.3% for design T80.

The spectral absorption models given in Section 3.2 are compared to the FEM simulations, and it was concluded that if there is no micromirror below the IR sensitive microplate, Eq. (3.123) gives more accurate results than Eq. (3.113). However, since the Poly 2 layer thickness is enough to absorb most of the IR radiation incident on it, both Eq. (3.123) and Eq. (3.113) estimate the coupling efficiency η with a discrepancy lower than 2%.

To validate the expected change in G as the microplate is actuated, thermal conductance measurements were made in the actuated and unactuated state. In Section 4.4.1, test structures with various microplate and arm dimensions were compared to the proposed thermal conductance model, and in Section 4.4.2, the thermal conductance of designs T80 and T120 were compared to the thermal contact model, previously given in Section 3.4. It was concluded that the results of the thermal model for the unactuated state are in good agreement with the experimen-

tal results, whereas the thermal contact model underestimates G at the actuated state, due to inaccuracies in contact pressure calculations and surface roughness.

Finally, the thermal capacitance calculated by two conventional models (Eq. (2.23) and Eq. (2.24)) and the proposed model (Eq. (3.197)) are compared to the FEM results. It was found that both Eq. (2.24) and Eq. (3.197) are in good agreement with the simulation results, whereas Eq. (2.23) deviates significantly from the simulation results.

As the result of the experiments, the operation of the proposed thermal conductance tuning mechanism was demonstrated, and it was shown that the mechanism is successfully modeled using the spectral absorption, electrostatic-structural and thermal models developed in Chapter 3. It was shown that by using the proposed mechanism, the thermal conductance of the microbolometer can be increased with a high range of linear tunability. Because of its linear performance and capability of pixel-by-pixel tuning, the method can be used as a technology to produce adaptive IR detectors with high dynamic range.

Chapter 5

Adaptive Microbolometer with Constant Spectral Response

In the previous chapter, the concept of tunable thermal conductance was analyzed and a complete microbolometer model was presented, which estimates the thermal conductance, the spectral response and the gap (cavity) thickness as a function of the actuation voltage.

Previously, it was shown that deflecting the microplate of the test structures (designs T80 and T120) has negligible effect on their spectral response (recall Fig. 4.13). However, in an actual microbolometer, where the microplate is thinner (a few hundred nanometers), changing the gap thickness might result in a change in the spectral response. Unless changed on purpose, such as the two-color microbolometers [45, 48], the change in the spectral response might lead to various problems, such as distortion and nonlinearity in the resulting image, depending on the application. In this chapter, this problem associated with the tunable thermal conductance microbolometers is addressed, and as a solution, a new pixel architecture is offered. It is proposed that by actuating the micromirror and the microplate together as a whole structure, the thickness of the gap between them can be kept constant.

The background matter and the problem definition with an example application is given in Section 5.1. A new microbolometer pixel design as a solution to the addressed problem is proposed in Section 5.2. In Section 5.3, the geometry of the proposed design is explained in detail and for realization of the proposed mi-

crobolometer, a fabrication process is offered. Finally, the performance parameters found by finite element analysis (FEA) are presented together with a discussion of the results and possible challenges in Section 5.4.

5.1 Background

Recently, there has been a significant increase in the performance of uncooled microbolometers, together with a decrease in their size and cost, which widens the application range of microbolometric thermal imagers. As new applications are conceived, the performance and the dynamic range requirements of the detector change, depending on the type of application. For instance, conventional microbolometers, which are mainly used for night vision and security purposes are not expected to have a high dynamic range, whereas the recent employment of uncooled microbolometers on high temperature process imaging requires the microbolometer FPAs to withstand high temperatures, i.e. requires microbolometers with a high dynamic range. High temperature process imaging includes the analysis of combustion processes, analysis of emissions from hot gases (such as jet exhausts) [75] and inspection of high temperature containers (such as boilers for preventative maintenance). Most space applications also require microbolometers with high dynamic range [76].

The spectral response of the microbolometers becomes an important design requirement as well, as high temperature process imaging with uncooled microbolometers becomes more popular. Unlike conventional microbolometers, which mostly operate in the long-wave IR (LWIR) band (8-12 μm), the high temperature process imaging usually requires operation in the medium-wave IR (MWIR) band, which is 3-5 μm [77]. This is because of Wien's Displacement Law, which states that there is an inverse relationship between the wavelength of the peak emission of a black body (λ_{peak}) and its temperature. Using Wien's Displacement Law, it can be found that λ_{peak} of a black body at 300 K is $\sim$9.7 μm, and λ_{peak} decreases to $\sim$4.8 μm when the temperature of the microbolometer increases to 500 K. A good example of the effect of the absorption spectrum on microbolometer performance is shown in Fig. 5.1, where two images of a soldering iron are given [16]. A detector working in the 8-12 μm range is more suitable for general usage, however the resulting image saturates when a hot object like a soldering iron is imaged (Fig. 5.1(a)). On

the other hand, the same object can be imaged without any saturation by using a detector operating in the 3-5 μm range (Fig. 5.1(b)).

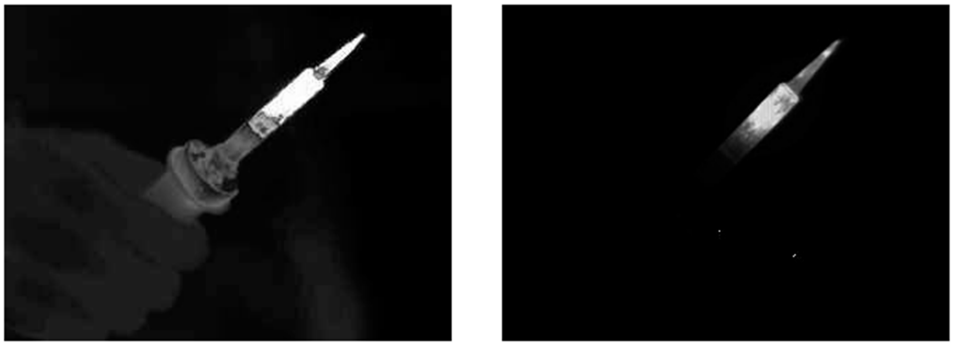

(a) (b)

Figure 5.1: The thermal image of a soldering iron, imaged by an IR camera operating at (a) 8-12 μm range, (b) 3-5 μm range. Reprinted from [16]

The spectral response of the microbolometer is a crucial design issue, when the microbolometer is used in combustion analysis and gas detection. As an example, the infrared emission of most rocket plumes is in the spectral region of 1-5 μm, therefore a microbolometer that is used in the analysis of a rocket plume should be able to operate in the 1-5 μm range. In gas detection, the gas that is to be detected emits infrared radiation in a specific band, depending on its molecular structure. Hence, the spectral response of the gas detecting microbolometer should be adjusted so that the IR radiation emitted by that specific gas is detectable.

As the microplate of a tunable G microbolometer deflects towards the micromirror, the gap thickness between the microplate and the micromirror changes, which alters the spectral response of the device. If a tunable G microbolometer is used in an application where the absorption spectrum is critical, the proper operation of the device will be affected as G is tuned. A microbolometer, which has a spectral response that does not change as G is tuned, will solve this problem. In the next section, a novel tunable G microbolometer with constant spectral response is proposed, and its design details are given.

5.2 Microbolometer Design

In this section, a tunable thermal conductance microbolometer with constant spectral response is presented. The aim of this section is to describe a new mechanism that tunes the thermal conductance electrostatically without affecting the spectral response; and to show that this mechanism can be employed to build a high performance microbolometer, capable of imaging high temperature processes. As an initial point, it is assumed that the following design requirements are given:

1. Changing the thermal conductance should not affect the spectral response.
2. To realize high temperature process imaging, the microbolometer should be able to detect signals in medium-wave IR band (3-5 μm).
3. The thermal conductance in the unactuated state should be less than 1×10^{-6} W/K.
4. The minimum imaging frame-rate should be 30 frame per second (fps).
5. The pixel size should be comparable to that of state-of-art microbolometers ($\leq$80 μm).
6. The actuation voltage should be less than 15 V.

The first design requirement is also the aim of the research presented in this chapter, whereas the rest are mostly typical design requirements of a high-performance microbolometer. In order to fulfill the first design requirement, the gap thickness should remain constant, as the thermal conductance is tuned electrostatically. As a solution to this problem, a new double-level pixel is proposed, which is schematically shown in Fig. 5.2. The upper microplate is connected to the lower microplate, which is a micromirror deposited on top of a support layer. In between the upper and the lower microplate, there is a gap, and there is another gap between the lower microplate and the substrate. The connection between the upper and the lower microplate is rigid, therefore as an actuation voltage is applied (see Fig. 5.2(b)), the upper and lower microplate move towards the stoppers together, and the thickness of the gap, i.e. the resonant cavity between them remains unchanged. The voltage is applied between the upper microplate (through the arms) and the actuation

electrode, located below the stoppers. No voltage is applied to the micromirror. In the unactuated state (see Fig. 5.2(a)), the heat loss is through the arms.

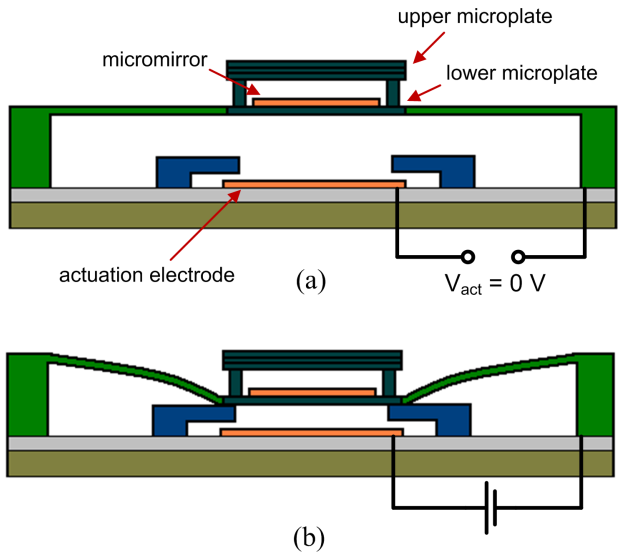

Figure 5.2: Cross-sectional schematic of the tunable thermal conductance microbolometer with constant spectral response, in the (a) unactuated state and (b) actuated (contact) state. Not drawn to scale.

The spectral response requirement (3-5 μm) can be satisfied by using the infrared absorption model given by Eq. (3.113). In Fig. 5.3, the layers that form the microbolometer pixel are shown. Layers 7 and 8 form the lower microplate and the arms. Layer 7 represents both the micromirror and the top layer of the bilayer arms, and layer 8 represents the structural layer of the lower microplate and the arms. The IR signal that reaches the micromirror (layer 7) reflects back from the top surface of the micromirror, therefore layers 7-12 are not used by the infrared absorption model. Layer 6 is the upper gap, i.e. the gap between the upper and lower microplate. The top layers (layers 1-5) form the upper microplate, i.e. the microplate that absorbs the IR power. Layer 5 is the support layer of the microplate. Layer 4 is the high TCR region, thus the material forming this layer should have a high temperature coefficient of resistance, such as Vanadium Oxide, semiconducting YBCO, amorphous silicon, etc. Layer 3 is the isolation layer, and it electrically isolates the high TCR layer from the absorber layer. The absorber layer is a thin metal layer, and it is deposited in order to increase the IR absorption. Finally, a protective layer is used on the top to passivate the absorber layer.

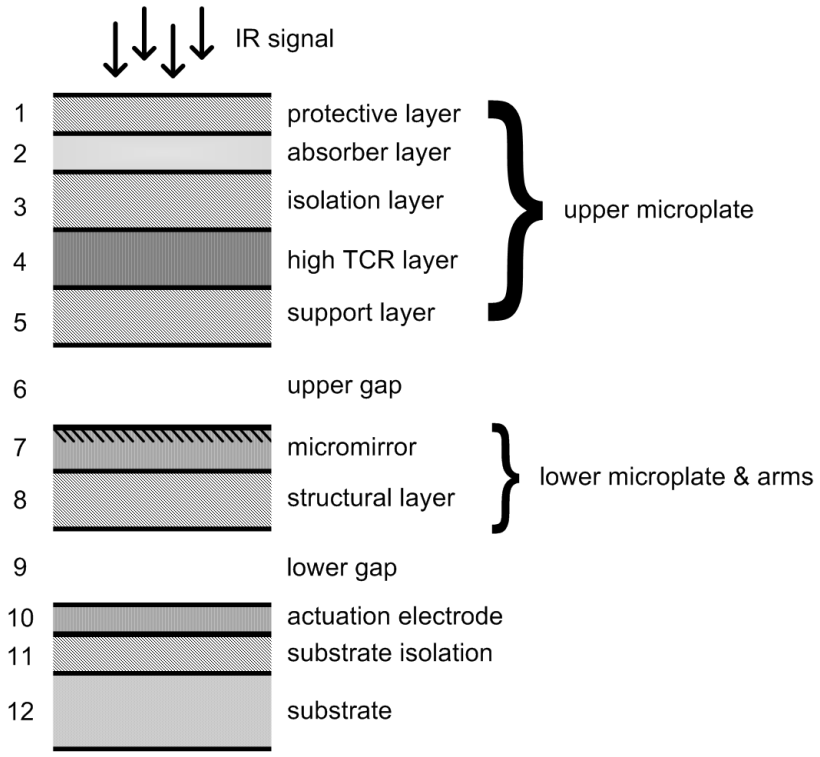

Figure 5.3: The layers that form the proposed microbolometer pixel.

By tailoring the upper microplate thin-film thicknesses (layer 1-5) and the upper gap thickness (layer 6), the desired spectral response can be obtained. However, the materials that form the pixel should be determined first. As for the protective, isolation, support, structural and substrate isolation layers (layers 1, 3, 5, 8 and 11), silicon nitride (SiN_x) is chosen, due to its good insulation characteristics, and its common use in microbolometers for support and isolation purposes [5, 35, 37]. For the high TCR layer, amorphous silicon (α-Si) is chosen, due to its high TCR, ease-of-fabrication and material properties that can be easily tailored by changing the processing conditions [34, 78]. In addition, α-Si is very suitable to be processed with SiN_x, as the thermal coefficient of expansion of α-Si and SiN_x are very close [79] (both are in the range 2-4 ppm/°C). In order to maximize the IR absorption, the sheet resistance of the absorber layer should be equal to the free space impedance, which is equal to 377 Ω [80]. Two commonly used absorber layer materials are nichrome (NiCr) and Titanium (Ti). By using the resistivities of NiCr and Ti (4.27×10^{-7} Ωm for Ti and 11×10^{-7} Ωm for NiCr), the optimum absorber thicknesses are found as 1.1 nm for Ti, and 3 nm for NiCr. Since it is easier to deposit a thin-film of 3 nm, NiCr is chosen as the absorber layer (layer 2). How-

ever, as for the arms, it is more convenient to use Titanium, due to its low thermal conductivity. In addition, Titanium shows good metallic properties, which makes it a suitable micromirror (layer 7) and actuation electrode (layer 10) material. The electrical, thermal and mechanical properties of silicon nitride, amorphous silicon, nickel-chrome and titanium are tabulated in Table 5.1.

The IR absorption depends on the thickness of the thin film layers. Therefore, by tailoring the thickness of the thin film layers, the absorption spectrum can be tuned according to the design requirements. However, the mechanical stability issues should be taken into account during the determination of thin-film thicknesses. If the microplate is not thick enough, the risk of failure at sacrificial release increases. Therefore, it will be safe to adjust the thickness of both of the microplates to at least 500 nm. On the other hand, increasing the microplate thickness increases the thermal time constant, which in turn decreases the upper limit on the imaging frame rate. Therefore, the design procedure followed here starts with assigning the thickness of each microplate layer, followed by adjusting the gap thickness by implementing the IR absorption model. The thickness of the support layer and the high TCR layer are chosen as 200 nm and the isolation layer is chosen as 150 nm. This way, the upper microplate thickness exceeds 500 nm. The absorber layer thickness is already found as 3 nm, and the protective layer thickness is taken arbitrarily as 5 nm.

Table 5.1: The electrical, thermal and mechanical properties of silicon nitride, nichrome, amorphous silicon and titanium.

Property	Unit	SiN_x	NiCr	α-Si	Ti
Resistivity (ρ)	Ωm	$1e^{13}$ [45]	$11e^{-7}$ [45]	$3.3e^{2}$ [81]	$4.3e^{-7}$ [82]
Relative permittivity (ϵ_r)	-	4 [45]	30 [45]	4.5 [83]	4.67 [84]
Thermal conductivity (k)	W/mK	3.2 [85]	90.7 [3]	2 [86]	21.9 [3]
Specific heat capacity (c)	J/kgK	333 [87]	440 [87]	810 [86]	530 [82]
Density (d)	kg/m^3	2440 [87]	8900 [87]	2330 [88]	4540 [82]
Young's modulus (E)	GPa	300 [87]	200 [87]	80 [89]	120.2 [82]
Poisson's ratio (ν)	-	0.26 [87]	0.312 [87]	0.22 [89]	0.32 [90]

The coupling efficiency η as a function of wavelength λ is calculated using the IR absorption model given by Eq. (3.113). In Fig. 5.4, the coupling efficiency is plotted

for three different values of gap thickness. From the figure, the most suitable gap thickness is chosen as 1.7 μm, since the microbolometer absorbs the 3-5 μm band in this case, and the maximum absorption occurs at 4 μm, the center of the band.

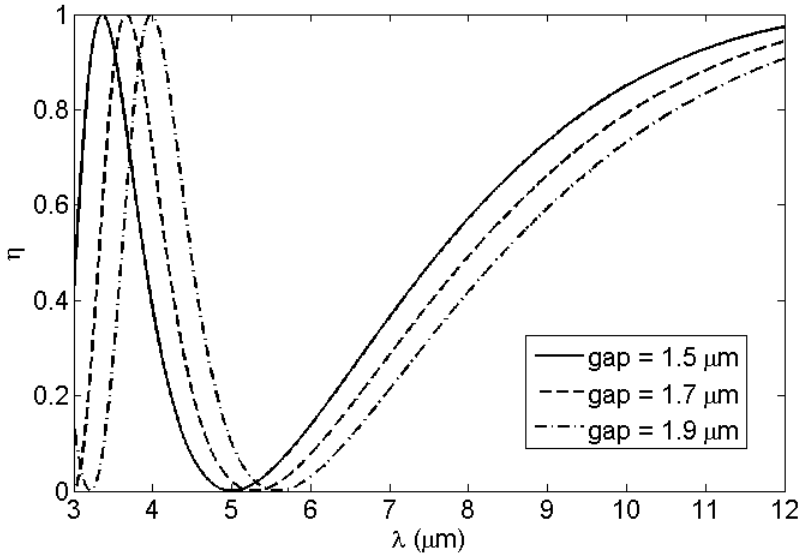

Figure 5.4: The plot of the coupling efficiency in the wavelength range of 3-12 μm, as the gap thickness is 1.5, 1.7 and 1.9 μm.

The third design requirement imposes that the thermal conductance should be less than 1×10^{-6} W/K. In addition, the fourth design requirement imposes that the minimum imaging frame rate should be 30 fps, which means the thermal time constant should be in the range of 10-15 msec [10]. According to Eq. (2.5), the thermal capacitance C of the pixel should be determined in order to check whether τ is within the limits.

In order to determine G and C, the dimensions of the upper and lower microplates and the arms should be determined. The thicknesses of the upper microplate layers have already been determined. In order for the micromirror (layer 7) to reflect back all of the IR radiation incident on it, it should act as a perfect electric conductor (PEC). This puts a minimum thickness requirement on the micromirror, which is calculated by the skin depth formula, given by [91]

$$\sigma_{sd} \approx 503\sqrt{\frac{\rho}{\mu_r f}}, \tag{5.1}$$

where σ_{sd} is the skin depth (i.e. the minimum thickness of layer 7), ρ is the resistivity, μ_r is the relative permeability and f is the frequency of the incident wave. The

wavelength range of interest is taken as 3-12 μm, which corresponds to a frequency range of 25-100 THz. Taking $f = 25$ THz, $\rho = 4.27 \times 10^{-7}\,\Omega\,\mathrm{m}$, and $\mu_r = 1$; σ_{sd} is found as ~ 66 nm. Noticing this minimum value for layer 7, the thicknesses of layer 7 and 8 are chosen as 200 nm and 400 nm, respectively. Layer 8 is thicker than layer 7, and the total thickness of layer 7 and 8 exceeds 500 nm, to improve mechanical stability. Since layer 7 and 8 also represent the arm layers, the thickness of the arm is also determined by determining the thicknesses of layers 7 and 8. The microplate size (i.e. the edge length of the square microplate) is taken as 70 μm, which fulfills the fifth design requirement. Increasing this dimension will increase the thermal capacitance, which in turn will decrease the frame-rate. On the other hand, decreasing the microplate size will increase the contact voltage.

Two methods are available to calculate the thermal conductance. The conventional method, which is based on the application of Fourier's law of heat conduction to the arms (Eq. (2.29)), can be expressed for the proposed microbolometer as

$$G = 2\frac{W_{arm}}{L_{arm}}\left(Z_{Ti}k_{Ti} + Z_{SiN_x}k_{SiN_x}\right), \tag{5.2}$$

where W_{arm} and L_{arm} are the arm width and length, respectively, and k and Z are the thermal conductivity and thickness of the corresponding material. Taking W_{arm} and L_{arm} as 6 and 100 μm, G is found as 6.79×10^{-7} W/K, which is within the required G range. As previously discussed in Section 2.2, the conventional method assumes that the temperature is uniform within the microplate. On the other hand, the composite region thermal model proposed in Section 3.3 considers the temperature variation within the microplate as well and calculates the G more accurately. Assuming that the upper microplate and the lower microplate are stacked together forming one microplate, and assuming that the arms are connected to the corners of the microplate, G is calculated as 5.54×10^{-7} W/K, which is again within the required range.

The thermal capacitance is estimated using the conventional method, given by Eq. (2.24). Taking 70 μm as the microplate size, C is estimated using Eq. (2.24) as 7.61×10^{-9} J/K. Using $\tau = C/G$, the thermal time constant τ is found as 11.2 msec. Alternatively, C can be estimated by the composite region thermal model (Eq. (3.197)) as 7.44×10^{-9} J/K, which gives $\tau = 13.6$ msec. Therefore, the thermal time constants found by the conventional method and the composite region thermal model show that the minimum frame-rate requirement can be fulfilled by using the

assigned pixel dimensions.

The last requirement to be satisfied is the contact voltage requirement. The contact voltage strongly depends on the pixel geometry as well as the thickness of layer 9, i.e. the thickness of the lower gap. Therefore, it is more convenient to estimate the contact voltage and design the lower gap thickness, after describing the pixel geometry in detail. Based on the design made in this section, the detailed microbolometer pixel structure is given, and a fabrication process flow is proposed in the next section.

5.3 Microbolometer Structure

The top view of the proposed microbolometer structure is shown in Fig. 5.5. Both the upper and the lower microplates are square, having a side length of d_{plate}. The arms are folded, in order to decrease the pixel footprint. The total length of an arm, L_{arm}, is equal to the summation of three arm portions, L_{arm1}, L_{arm2} and L_{offset}. The arms are connected to the corners of the microplate. Each Titanium arm layer forms a small square region of side length d_{sq} at the corresponding corner of the SiN_x supporting layer. At the center of these square regions, smaller square prisms are located, which have the height equal to the thickness of the upper gap (layer 6). These square prisms are called connectors, as they connect the lower microplate to the upper microplate. On top of the connectors, the upper microplate is located, and the side length of the upper microplate layers (layers 1-5) is equal to that of the lower microplate, d_{plate}. For visual purposes, the upper microplate layers are not shown in Fig. 5.5. Below the microplate, the stoppers and the actuation electrode are located. The area of the actuation electrode is taken to be equal to the area of microplate, 70×70 μm^2. The geometric parameters of the microbolometer together with the layer thicknesses are tabulated in Table 5.2.

As the geometry of the pixel is given in detail, the contact voltage can be determined using the model proposed in Section 3.1. First, the bending stiffness of the arm section is found. This is followed by the calculation of the equivalent spring constant, which is then used in the contact voltage calculation.

To calculate the bending stiffness, the method given in Section 3.1.1 is used. First, the width of the upper region (Ti) is scaled so that the composite section is

Table 5.2: The geometric parameters and layer thicknesses of the proposed microbolometer.

Dimensions (μm)		Layer thicknesses (nm)	
d_{plate}	70	Layer 1	5
L_{arm}	100	Layer 2	3
L_{arm1}	75	Layer 3	150
L_{arm2}	20	Layer 4	200
L_{offset}	5	Layer 5	200
d_{sq}	10	Layer 6	1700
d_{conn}	5	Layer 7	200
W_{arm}	6	Layer 8	400

simplified into a single material section. Then, the centroid location of the resulting section is found using Eq. (3.3), followed by the calculation of the moment of inertia of the composite section using the parallel axis theorem. Using the material properties in Table 5.1, the bending stiffness is found as 3.41×10^{-14} Nm^2.

To calculate the equivalent spring constant k_{eq}, the same methodology used to find k_{eq} of design T80 is followed, as both structures have folded bilayer arms. Using Swanson's method to calculate the torsional stiffness (Eq. (3.58)), k_{eq} is found as 0.85 N/m.

As the final step, the contact voltage is calculated using k_{eq}. In Fig. 5.6(a), the schematic view of the microbolometer pixel is depicted, showing the charges on the high TCR layer (layer 4), the micromirror layer (layer 7), and the base electrode layer (layer 10). There are also two silicon nitride dielectric layers in the structure, the support layer (layer 5) and the structural layer (layer 8). It is assumed that all plates have equal surface areas, so the electric fields are vertical. The micromirror has floating potential, i.e. it is not connected to any electrical source. As the micromirror is located between two plates connected to a voltage source (layer 4 and 10), the following two conditions should be met for this layer:

- The electric field inside the layer equals zero,
- The total charge of the layer equals zero.

These two conditions are met when the surface charge density of the micromirror is

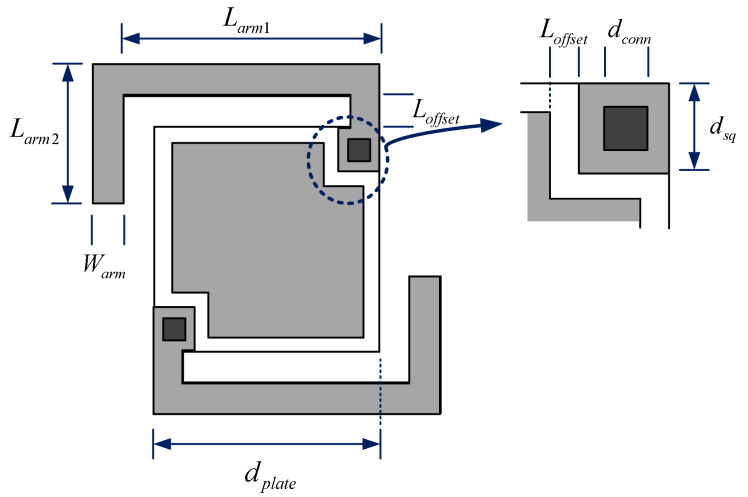

Figure 5.5: The top view of the proposed microbolometer.

equal to the surface charge density of the outer layers (layer 3 and layer 10). Since the surface areas of these layers are assumed to be equal, it can be concluded that all surfaces have the same amount of charge, as seen in Fig. 5.6(a).

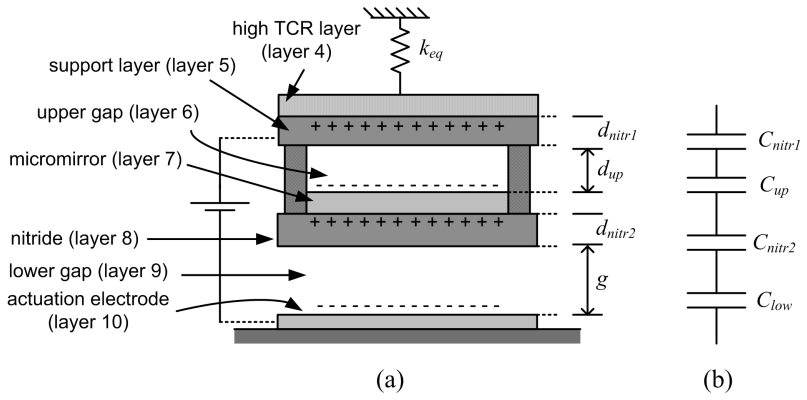

Figure 5.6: (a) The schematic view of the parallel plate capacitor representation of the proposed microbolometer; (b) the total capacitance of the parallel plate capacitor as a summation of four capacitances.

The energy stored in the capacitor, where the upper electrode is layer 4, and the lower electrode is layer 10, can be expressed as:

$$W = \frac{1}{2} C_{el} V_{act}^2, \tag{5.3}$$

where V_{act} is the voltage and C_{el} is the total capacitance of the capacitor. The total capacitance can be written as a summation of four capacitances in series (see

Fig. 5.6(b)), stated as

$$\frac{1}{C_{el}} = \frac{1}{C_{nitr1}} + \frac{1}{C_{up}} + \frac{1}{C_{nitr2}} + \frac{1}{C_{low}}, \tag{5.4}$$

where C_{nitr1} and C_{nitr2} are the capacitances of the nitride layers, C_{up} is the capacitance of the upper gap, and C_{low} is the capacitance of the lower gap. Using the formula for a parallel plate capacitor ($C_{el} = \kappa\epsilon_0 A_{mp}/d$) and taking κ_{nitr} as dielectric constant of nitride, C_{el} can be stated as

$$\frac{1}{C_{el}} = \frac{d_{nitr1}}{\kappa_{nitr}\epsilon_0 A_{mp}} + \frac{d_{up}}{\epsilon_0 A_{mp}} + \frac{d_{nitr2}}{\kappa_{nitr}\epsilon_0 A_{mp}} + \frac{g}{\epsilon_0 A_{mp}} \tag{5.5}$$

$$\Rightarrow C_{el} = \frac{\epsilon_0 A_{mp}}{g + d_{up} + d_{nitr}}, \tag{5.6}$$

where

$$d_{nitr} = \left(d_{nitr1} + d_{nitr2}\right)/\kappa_{nitr}. \tag{5.7}$$

In order to find the electrostatic force, the derivative of W with respect to the lower gap thickness g, is taken.

$$F_{ES} = -\frac{\partial W\left(V_{act}, d\right)}{\partial g}\bigg|_{V_{act}} = \frac{\epsilon_0 A_{mp} V_{act}^2}{2\left(g + d_{up} + d_{nitr}\right)^2}. \tag{5.8}$$

To find the net force acting on the suspending microplates, the mechanical force F_{mech} is expressed as

$$F_{mech} = k_{eq}\left(g_0 - g\right), \tag{5.9}$$

where g_0 is the lower gap thickness in the unactuated state ($V_{act} = 0$).

To find the contact voltage $V_{contact}$, the net force on the microplate F_{net} is expressed first.

$$F_{net} = F_{mech} - F_{ES} = k_{eq}\left(g_0 - g\right) - \frac{\epsilon_0 A_{mp} V_{act}^2}{2\left(g + d_{up} + d_{nitr}\right)^2}. \tag{5.10}$$

At the onset of contact state, both F_{net} and the derivative of F_{net} with respect to g equals zero, which gives

$$V_{contact} = \sqrt{\frac{8k_{eq}\left(g + d_{up} + d_{nitr}\right)^3}{27\epsilon_0 A_{mp}}}. \tag{5.11}$$

The dimensions d_{up}, d_{nitr} and A_{mp} were already assigned during the design. In Fig. 5.7, $V_{contact}$, calculated by Eq. (5.11), is plotted as g_0 is varied between 1.1

μm and 1.8 μm. From the plot, the limit value of g_0 is found as 1.5 μm, which corresponds to a contact voltage of $\sim$14.8 V. To be on the safe side, g_0 is chosen as 1.4 μm, which corresponds to $V_{contact} = 14.1$ V. The reason of choosing a high value of g_0 is to decrease the risk of in-use-stiction. As the value of g_0 is increased, the arms deflect more at contact state. Therefore, the mechanical restoring force increases, which reduces the risk of in-use stiction. A detailed discussion about in-use stiction is given in Section 5.4.

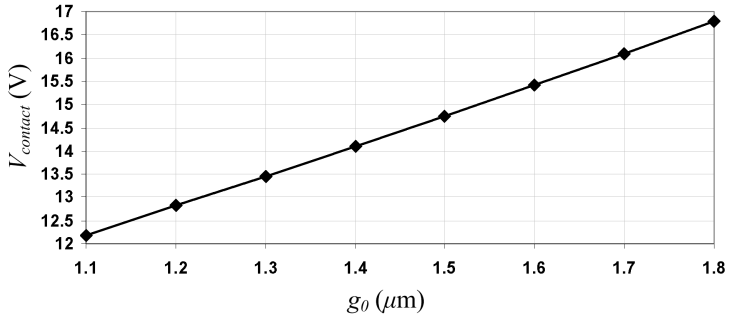

Figure 5.7: The contact voltage, calculated by Eq. (5.11), as g is varied from 1.1 μm to 1.8 μm.

The realization of the proposed microbolometer design can be achieved by assuming the following fabrication sequence. A 500 μm Silicon wafer is used as substrate. To electrically insulate the substrate, a 500 nm low-stress LPCVD (low-pressure chemical vapor deposition) silicon nitride layer is deposited on the wafer. This is followed directly by the deposition of a 200 nm Titanium layer to form the electrical connections and the actuation electrode (layer 10). The Ti layer is deposited by RF sputtering, and patterned using a lift-off process. Other methods, such as e-beam evaporation or PVD (physical vapor deposition) can be used for Ti deposition as well.

The next step is the deposition of the first sacrificial layer. As the sacrificial layers, polyimide is used, as it is a common sacrificial layer when SiN_x is used as the structural layer [5, 35]. To improve the adhesion between the polyimide and the SiN_x insulation layer, 0.1% VM-651, diluted in DI water is spin coated [5]. The details of the polyimide deposition, such as the spin coater revolution speed, spinning time, and curing time after deposition, affect the final polyimide thickness. Thus, the deposition conditions should be varied in order to achieve the desired polyimide thickness. The thickness of the first sacrificial layer is taken as 300

nm. After deposition and curing of the polyimide, it is patterned using a 300 nm thick Aluminum masking layer, which is patterned by lift-off. The etching of the polyimide is done with O_2 plasma to form the anchor of the arms and stoppers. The side view of the half of the microbolometer pixel after patterning the first polyimide layer is shown in Fig. 5.8(a).

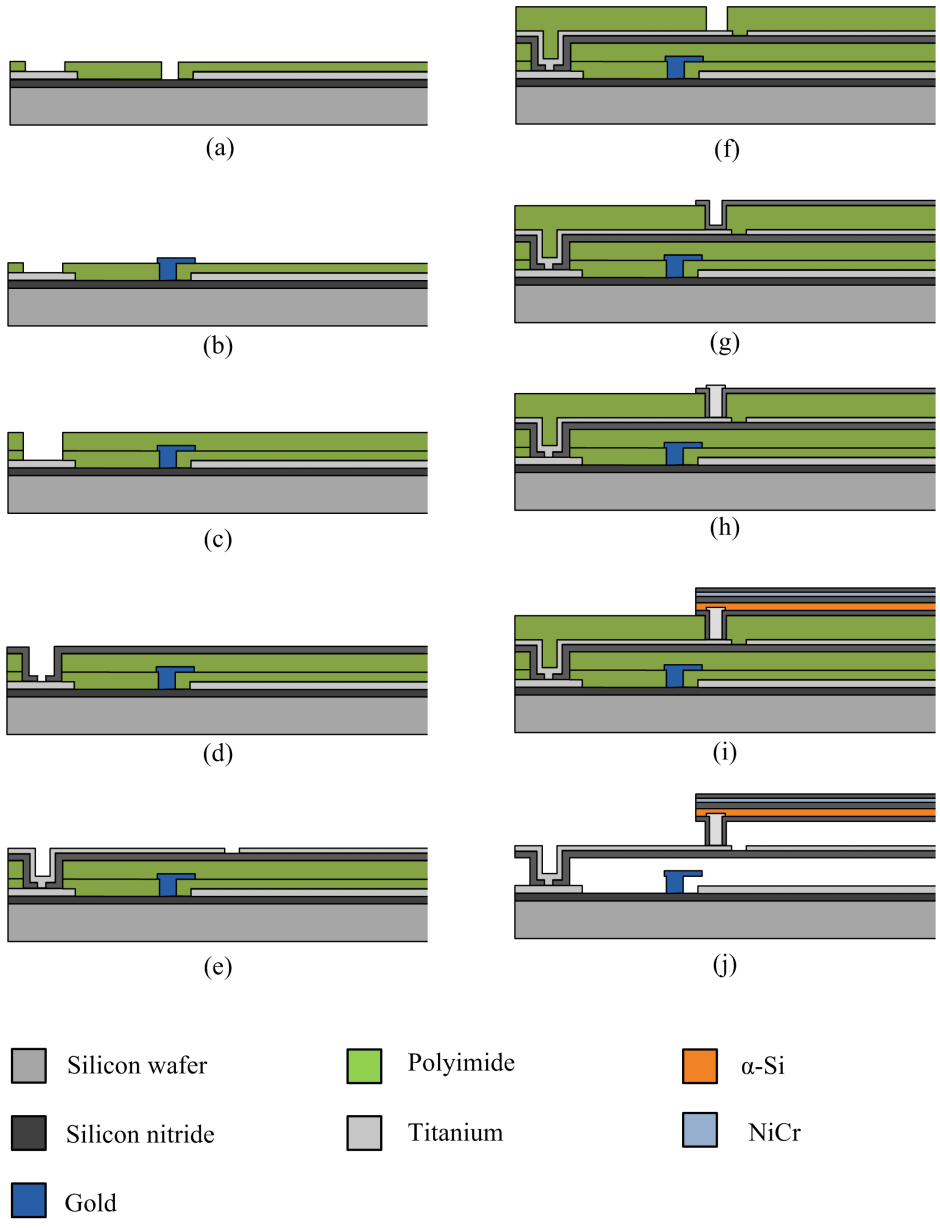

Figure 5.8: The fabrication process flow for the proposed microbolometer. Only half of the microbolometer pixel is shown.

The next step is the deposition of the stoppers. The stopper material should

have a high thermal conductivity, as its aim is to form a strong thermal link between the lower microplate and the substrate. Hence, Titanium is not a good stopper material, due to its low thermal conductivity. As the stopper material, gold (Au) is used, due to its high thermal conductivity and chemical resistivity. However, a thin adhesion layer of Ti should be deposited before the deposition of Au. The geometry and the dimensions of the stoppers are not specified, as they only affect the thermal conductance at the actuated state, which is not given in the design requirements. However, it is expected that short stoppers with large contact area will result in a high thermal conductance at the actuated state. The side view of the half-pixel after the patterning of the stopper is shown in Fig. 5.8(b).

Following the stoppers, the second Polyimide sacrificial layer is deposited. The total thickness of the first and second sacrificial layers equals the lower gap thickness, which was designed as 1.4 μm. Therefore, the thickness of the second sacrificial layer after deposition and post-annealing steps should be 1.1 μm. The Polyimide is patterned by an Al masking layer, and etched with O_2 plasma, to form the anchor of the arms (Fig. 5.8(c)).

As the structural layer (layer 8), a 400 nm PECVD (plasma enhanced chemical vapor deposition) SiN_x is deposited. The reason of choosing PECVD nitride instead of LPCVD nitride is that very low-stress nitride films with low thermal conductivity can be produced by varying the fabrication conditions of the PECVD process [92, 93]. The PECVD nitride is patterned using CF_4+O_2 plasma, to form the arms and the microplate (Fig. 5.8(d)). Following the patterning of the nitride layer, a 200 nm Ti layer is sputter deposited and patterned using lift-off, to form the micromirror and the Ti coating of the arms. In order to ensure that the sidewall between the edge of the arm and the anchor is covered with Ti, an additional Ti film can be deposited on the sidewall. The side view of the half-pixel after the patterning of the Ti layer is shown in Fig. 5.8(e).

The next step is the deposition of the last polyimide sacrificial layer, which will form the 1.7 μm-thick upper cavity after release. The Polyimide layer is patterned to form the anchor of the upper microplate (see Fig. 5.8(f)). A 200 nm PECVD nitride is deposited and patterned next to form the support layer (layer 5) of the upper microplate (see Fig. 5.8(g)). To form the connectors between the upper and the lower microplate, a Ti layer with a thickness of 1.7 μm is deposited on the anchors of the upper microplate. The patterning of the Ti layer is made by lift-off

process. The side view of the half-pixel after patterning of connectors is shown in Fig. 5.8(h).

Following the connectors, the α-Si layer is deposited using sputtering and patterned by dry etching. Next, a 150 nm PECVD nitride isolation layer (layer 3) is deposited and etched, which is followed by the sputter deposition of the 3 nm NiCr absorber layer. Then, the 5 nm PECVD nitride passivation layer (layer 1) is deposited and patterned to encapsulate the upper microplate (see Fig. 5.8(i)). Finally, the polyimide sacrificial layers are isotropically etched in an O_2 plasma [94], to release the pixel. To facilitate the etching process, etch holes should be cut on the microplate layers. The side view of the half pixel after release is shown in Fig. 5.8(j).

In the next section, the results of the finite element simulations are presented, together with the evaluation of microbolometer performance and fabrication challenges.

5.4 Results and Discussion

The finite element analysis of the proposed microbolometer includes two finite element (FE) models:

- Infrared absorption FEM constructed using HFSS,
- Thermal FEM constructed using COMSOL,

Using these models, the microbolometer performance is characterized, and the results are compared to the design requirements. The models are constructed using the same methodology used in constructing the FE models for designs T80 and T120 (see Section 3.5).

For the IR absorption simulations, a composite slab is constructed, which includes layers 1-6 of the microbolometer. The total length of the slab is taken as 4 μm, and an extra layer of vacuum is added to the top of layer 1 to apply the electromagnetic wave excitation properly from the top. The simulations are made in the wavelength range of 3-12 μm. The result of the simulations are compared to the data plotted in Fig. 5.4, and it is found that the average absolute discrepancy

of the model with respect to the simulations is as low as 0.0065, in the range of 3-12 μm. Therefore, the spectral absorbance simulations verify that the second design requirement is satisfied.

To check whether the third and fourth design requirements are satisfied, a thermal FEM is constructed using COMSOL. Prescribing a uniform heat generation rate within the high TCR layer, the steady-state temperature distribution is computed. The thermal conductance G is then determined by dividing the total generated heat to the steady-state area-averaged temperature increase of the high TCR layer. To find the thermal time constant, the transient solver is used and the area-averaged temperature increase of the microplate is plotted as a function of time. As a result of the simulations, G is found as 5.42×10^{-7} W/K, which is less than the upper limit prescribed by the corresponding design requirement (1×10^{-6} W/K). One should notice that this G value is less than G calculated by the theoretical models, which are given in the previous section. This difference is due to the separation between the upper and lower microplate, which is not considered by the theoretical models. The thermal time constant found by the FEM simulations is 11.4 msec, which is within the 10-15 msec range, prescribed by the 30 fps frame-rate requirement.

Avoiding in-use stiction is also an important aspect of a tunable G microbolometer design. In order to decrease the risk of in-use stiction, the molecular adhesion force between the stoppers and the microplate should be reduced and the mechanical restoring force should be increased. The adhesion force can be decreased by choosing proper materials for the stopper and the support layer of the microplate, and by decreasing the contact area. The restoring force, defined as $k_{eq}(g_0 - g_{contact})$, can be increased by increasing either the equivalent spring constant k_{eq} or the deflection of the arms at contact $(g_0 - g_{contact})$. An effective way of increasing k_{eq} is to fabricate thicker, wider and shorter arms, which has the drawback of increasing G. Increasing $g_0 - g_{contact}$ is a better option; however it results in a higher contact voltage. Therefore, while decreasing the risk of in-use stiction, the performance degradation of the microbolometer should be taken into account.

The fabrication process proposed in the previous section uses a standard structural layer-sacrificial layer, silicon nitride and polyimide. The other materials used in the process are also commonly used materials in MEMS processes. However, the fabrication process uses three sacrificial layers, which increases the fabrication complexity and the risk of failure during release. If the stoppers are designed as

simple rectangular prisms, the first sacrificial layer will be redundant, and only two sacrificial layers will be enough for the whole process, which reduces the fabrication complexity.

Another factor that increases the fabrication complexity is the double layer structure of the microbolometer. Etching of the sacrificial layer can be cumbersome, if the number and size of the etch holes are inadequate. In addition, the upper gap thickness may be different from its design value after release, which may result in an undesired absorption spectrum. This risk can be avoided by varying the fabrication conditions until a process flow is achieved where the gap thickness does not change after release. Another solution to this problem is to fabricate a single microplate instead of two, where the micromirror is the bottom layer of the microplate. In this structure, the resonant cavity is filled by a material, preferably with a high refractive index. The thickness of the thin-film layers forming this structure can be tailored so that the desired absorption spectrum can be obtained. The fabrication of this structure is less cumbersome than fabricating a double layer structure. However, as the cavity is filled with a dielectric, the thermal mass of the microplate will increase tremendously, which will increase the thermal time constant. Therefore, this alternative design will not be suitable for high frame-rate imaging applications.

5.5 Conclusions

In this chapter, the effect of thermal conductance tuning on spectral response in a typical tunable G microbolometer is investigated, with an emphasize on its potential hurdles in applications requiring constant spectral response. As a solution, a new tunable G microbolometer architecture is proposed, in which the spectral response remains constant as G is tuned by electrostatic actuation. The microbolometer is designed using the theoretical models for IR absorption, thermal conductance, thermal capacitance and contact voltage. A fabrication process for the proposed microbolometer is offered, and the microbolometer is characterized using FEM simulations. It was shown that the proposed model can be employed to build a high performance tunable G microbolometer with constant spectral response.

Chapter 6

Conclusions

6.1 Summary of Contributions

In this thesis, approximate analytical models for tunable thermal conductance (tunable G) microbolometers were developed, and validated experimentally. In addition, a novel tunable G microbolometer with constant spectral response was designed. The contributions of this research are summarized below.

1. **Development of a microbolometer analytical model, including an accurate thermal model:** An extensive analytical model was developed for tunable G microbolometers. The model estimates the basic parameters that characterize the microbolometer performance, using the basic principles of electromagnetics, electrostatics, mechanics, and heat transfer. These parameters include:

    - Coupling efficiency (η): η is calculated based on the propagation of TEM waves within multilayer media. Two models for η are constructed: The typical case where a micromirror is deposited on the substrate, and the case where the substrate partly absorbs the IR radiation. Compared to the finite element simulations, the proposed models estimate η with a discrepancy lower than 2 %.
    - Contact voltage ($V_{contact}$): Based on the geometry of the microbolometer pixel and the mechanical properties of the materials forming the pixel,

the equivalent spring constant of the arms were expressed, and $V_{contact}$ was calculated by a parallel-plate tunable MEMS capacitor approach.

- Thermal conductance (G) and thermal capacitance (C): A novel thermal model that is more accurate than the conventional thermal models was developed. Unlike the conventional models, this model considers the spatial temperature change within the IR sensitive microplate, and uses the area averaged temperature increase of the microplate for the calculation of G. To increase the accuracy of the G estimation, approximate models for the constriction thermal resistance between the microplate and arms are used for different pixel architectures. In addition to G, the thermal capacitance C can also be calculated from the transient solution of the heat equation obtained by the thermal model. When compared to the experimental results in various arm and microplate dimensions, it was found that the proposed method estimates the G with a maximum discrepancy of 10% with respect to the experimental results, whereas the maximum discrepancy of the conventional method was 42 %. A journal paper that includes these promising results and a detailed explanation of the model has been submitted to Sensors and Actuators A: Physical of Elsevier [95]. In addition, two refereed conference papers and one refereed conference abstract have been published [96–98]. At contact state, the thermal conductance is mainly determined by the thermal contact resistance of the newly formed contacts between the microplate and the surface it contacts. The thermal contact model for conforming rough surfaces is used to estimate the thermal conductance at the actuated state.

2. **Improvement of the current thermal conductance tuning mechanism:** Several modifications were made to the current design, which include using the micromirror as the actuation terminal and using stoppers. The stoppers are beneficial in decreasing the risk of in-use stiction, whereas using the micromirror as the actuation terminal enables pixel-by-pixel actuation. The proper operation of the G tuning mechanism was validated by optical profiler, electrical capacitance and thermal conductance measurements. It was found that, with an actuation voltage of ∼11 V, G can be increased from 1.42×10^{-5} to 3.36×10^{-5} W/K, and can be tuned linearly from 3.36×10^{-5} to

4.85×10^{-5} W/K, as the applied voltage is tuned between 11 V and 35 V. A journal paper that reports the results of the experiments has been submitted to the Journal of Micromechanics and Microengineering [99], and a refereed conference paper has also been published [100]. The proposed mechanism can be used as a potential G tuning mechanism in next generation adaptive microbolometers.

3. **Tunable thermal conductance with constant spectral response:** A new tunable G microbolometer pixel is designed, addressing the problem of undesired change in spectral response as G is tuned. The designed pixel is a double layer structure consisting of an IR sensitive upper microplate and a lower microplate that has a micromirror. The thickness of the gap between the IR sensitive layer and the micromirror does not change during actuation, resulting in a constant spectral response as G is tuned. The microbolometer is designed using the theoretical models developed in Chapter 3, and a fabrication process for the designed microbolometer is offered. Using FEM simulations, it was shown that a state-of-art microbolometer with high performance ($G = 5.42 \times 10^{-7}$ W/K, $\tau = 11.4$ msec) can be produced.

6.2 Suggestions for Future Work

In this section, some suggestions are given, which can be beneficial for the improvement of the proposed mechanisms and devices.

- The G tuning mechanism proposed in Section 2.3.3 is fabricated using a PolyMUMPs process. The capabilities of PolyMUMPs are not enough to build a microbolometer pixel. Building a tunable G microbolometer by using a custom fabrication process will be beneficial, as it gives the opportunity to determine the effectiveness of the proposed mechanism. In addition, some important performance parameters such as responsivity and thermal time constant can be verified, and the infrared absorption model can be validated. A custom fabrication will also give the opportunity to build stoppers that are shorter in height, so that the risk of in-use stiction can be decreased.

- By fabricating stoppers with various geometries, their effect on thermal conductance tunability, surface planarity and contact voltage can be analyzed.

The stopper geometry employed in this thesis and two other suggested stopper geometries are shown in Fig. 6.1. The stopper shown in Fig. 6.1(b) is easy to fabricate; however the surface planarity of the microplate at actuation is a question mark. Increasing the number of these simple stoppers will result in a decrease in IR absorption, as they decrease the effectiveness of the micromirror. A microbolometer having the microbridge shaped stoppers in Fig. 6.1(c) is expected to exhibit high microplate surface planarity at actuation, however the absorption spectrum of this structure is needs investigation. The gap between the microplate and the micromirror resembles the multiple resonant cavity design in [37], and it can be used in applications that require a broadband response.

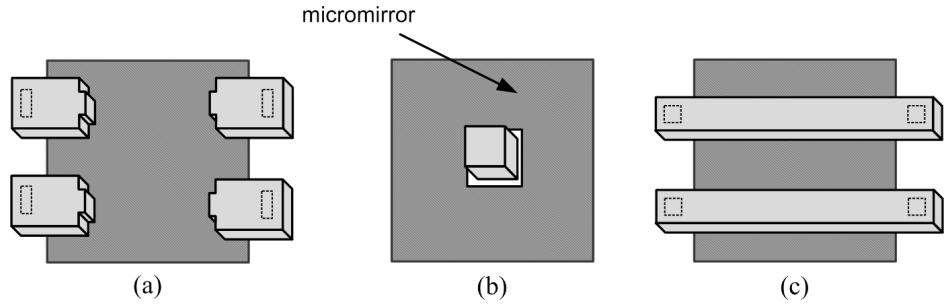

Figure 6.1: Schematics of various stopper designs: (a) the design used in this research, (b) a simple stopper design that does not require a sacrificial layer, (c) microbridge shaped stoppers for improved microplate planarity and broadband absorption.

- Fabrication of the proposed design in Chapter 5 will be a major improvement, as it will be the first tunable G microbolometer with constant spectral response. The fabrication process flow offered in Section 5.3 can be used as a guideline.

- The design in Chapter 5 can be improved by using a hidden arm structure, in which the arms are deposited below the lower microplate. The advantage of this design will be the improvement in the fill-factor, however the fabrication of such a structure will be more complex as the number of sacrificial layers will increase.

- In a typical microbolometer focal planar array (FPA), the cross talk between

adjacent pixels is not significant due to the high thermal capacitance of each pixel [24]. However, in a tunable G microbolometer, the thermal capacitance decreases significantly in the actuated state, which may result in cross talk between adjacent pixels. Therefore, the cross talk effect should be investigated by fabricating a 2D tunable G microbolometer array.

- The readout circuitry of a microbolometer FPA consists of on-off electronic switches that control the voltage of each pixel. In a tunable G microbolometer FPA, an additional controller unit is necessary to actuate the G tuning mechanism of each pixel, when the signal level of that pixel is above a threshold. Designing such a control unit and integration of this unit with standard microbolometer readout electronics would be a significant advance in high performance microbolometer technology.

Appendix A

Matlab Script for Calculation of the Contact Voltage of the PolyMUMPs Test Structures

The following Matlab script is used to calculate the contact voltage of the fabricated PolyMUMPs test structures.

A.1 Design T80

```
%================================================
% The contact voltage calculation for design T80:
%================================================
clear all;

%------------------------------------------------
% Material properties and geometric parameters:
%------------------------------------------------
E1 = 158e9; % Young's modulus (polysilicon)
E2 = 77.2e9; % Young's modulus (gold)

pr_1 = 0.22; % Poisson's ratio (polysilicon)
pr_2 = 0.42; % Poisson's ratio (gold)

w1 = 10e-6; % Width (polysilicon)
w2 = 4e-6; % Width (gold)
```

```
t1 = 1.3e-6; % Thickness (polysilicon)
t2 = 0.5e-6; % Thickness (gold)

Z0 = 2.7e-6;  % Initial gap thickness

%-----------------------------------------------
% Implementing the method of transformed sections:
%-----------------------------------------------
% The width of gold region is transformed:
w2_new = w2*(E2/E1);

% Area moment of inertias:
I1 = (w1*t1^3)/12;
I2 = (w2_new*t2^3)/12;

% Areas of lower and upper section:
A1 = w1*t1;
A2 = w2_new*t2;

%  Location of centroids of lower and upper section:
y1 = t1/2;
y2 = t1 + (t2/2);

% The centroid location of the transformed section:
y_c = (A1*y1 + A2*y2)/(A1+A2);

% The area moment of inertia of the transformed section:
I_c = I1 + A1*(y_c-y1)^2+A2*(y_c-y2)^2+I2;

% The total bending stifnesss of the composite section:
Et_it = E1*I_c;

%-----------------------------------------------
% Calculation of the equivalent spring constant k_eq:
%-----------------------------------------------
L1 = 37e-6; % Length of 1st beam
L2 = 143e-6; % Length of 2nd beam

% Calculation of the torsional stiffness by Swanson's method:
```

```
% Torsional modulus of rigidity for polysilicon and gold:
G1 = E1/(2*(1+pr_1));
G2 = E2/(2*(1+pr_2));

% The half width and half thickness of the simplified section:
a = w1/2;
b = (t1+t2)/2;

% The parameters h0, h1 and h2:
h0 = -b;
h1 = t1-b;
h2 = b;

T = G1/G2; % The constant Theta
Ka = h1/b; % The constant Kappa

% The coefficients A1, A2, B1 and B2:
B1 = ((Ka-1)^2)/2 +(2*Ka-1)/(2*T);
B2 = T*(B1 + 2*Ka)-2*Ka;
A1 = 1-B1;
A2 = 1+B2;

Sum1 = (A1*(h1-h0)/b)-(B1*(h1^2-h0^2)/(2*(b^2)))-((h1^3-h0^3)/(3*(b^3)));
Sum2 = (A2*(h2-h1)/b)-(B2*(h2^2-h1^2)/(2*(b^2)))-((h2^3-h1^3)/(3*(b^3)));

% The torsional stiffness:
K_times_G = ((2*a)*((2*b)^3)/4)*(G1*Sum1 +G2*Sum2);

Forc = 1e-8; % An arbitrary value for the force

Tork2 = (Forc*L1*L1/2)/(L1+(L2*Et_it/KKK)); %T2
Tork1 = (Forc*L2*L2/2)/(L2+(L1*Et_it/KKK)); %T1

% Expressing v_tot:
v_tot = ((Tork2-Forc*L1)*L1^2)/2;
v_tot = v_tot+ Forc*(L1^3+L2^3)/6;
v_tot = v_tot - (Tork1*L2^2)/2;
v_tot = v_tot/(Et_it) - Tork1*L1*L2/(K_times_G);

% The equivalent spring constant:
k_eq = -2*Forc/v_tot;
```

```
%-----------------------------------------------
% Calculation of the contact voltage V_contact:
%-----------------------------------------------
plate = 80e-6; % Microlate size length
A_mp = plate^2; % Microplate area

epsilon_0 = 8.854e-12; % Permittivity of free space

% The contact voltage:
V_contact = sqrt(8*k_eq*Z0^3/(27*epsilon_0*A_mp))
```

A.2 Design T120

```
%===============================================
% The contact voltage calculation for design T80:
%===============================================
clear all;

%-----------------------------------------------
% Material properties and geometric parameters:
%-----------------------------------------------

E1 = 158e9; % Young's modulus (polysilicon)
E2 = 77.2e9; % Young's modulus (gold)

pr_1 = 0.22; % Poisson's ratio (polysilicon)
pr_2 = 0.42; % Poisson's ratio (gold)

w1 = 10e-6; % Width (polysilicon)
w2 = 4e-6; % Width (gold)

t1 = 1.3e-6; % Thickness (polysilicon)
t2 = 0.5e-6; % Thickness (gold)

Z0 = 2.7e-6;  % Initial gap thickness

%-----------------------------------------------
% Implementing the method of transformed sections:
%-----------------------------------------------
```

```
% The width of gold region is transformed:
w2_new = w2*(E2/E1);

% Area moment of inertias:
I1 = (w1*t1^3)/12;
I2 = (w2_new*t2^3)/12;

% Areas of lower and upper section:
A1 = w1*t1;
A2 = w2_new*t2;

%  Location of centroids of lower and upper section:
y1 = t1/2;
y2 = t1 + (t2/2);

% The centroid location of the transformed section:
y_c = (A1*y1 + A2*y2)/(A1+A2);

% The area moment of inertia of the transformed section:
I_c = I1 + A1*(y_c-y1)^2+A2*(y_c-y2)^2+I2;

% The total bending stifnesss of the composite section:
Et_it = E1*I_c;

%-------------------------------------------------
% Calculation of the equivalent spring constant k_eq:
%-------------------------------------------------
L = 160e-6; % Arm length
k_eq = (24*Et_it)/(L^3); % 1 for guided, 4 for free end

%-------------------------------------------------
% Calculation of the contact voltage V_contact:
%-------------------------------------------------
plate = 120e-6; % Microlate size length
A_mp = plate^2; % Microplate area

epsilon_0 = 8.854e-12; % Permittivity of free space

% The contact voltage:
V_contact = sqrt(8*k_eq*Z0^3/(27*epsilon_0*A_mp))
```

Appendix B

Matlab Script for Calculation of η of the Test Structures

The following Matlab script is used to calculate η of the fabricated PolyMUMPs test structures, within a wavelength range of 4-12 μm.

```
clear all;

% The constants:
c = 299792458; % speed of light
eps_0 = 8.8541878176e-12; % permittivity of free space
mu_0 = 4*pi*1e-7; % permeability of free space
eta0 = 1/sqrt(mu_0/eps_0); % Characteristic impedance of free space
j = sqrt(-1);

% The thickness vector L. The 1st element of the vector corresponds to the
% thickness of the Poly 2 layer, and the last element corresponds to the
% thickness of the substrate.
L = [1.5e-6;2.75e-6;5e-7;5e-7;5e-4];

% The resistivity vector:
rho = [30e-6;1/0;15e-6;1e13;0.01];
% Note: the resistivity of the cavity is taken as infinite.

% The relative permittivity vector:
eps_r = [11.2;1;11.2;4;11.2];

% X vector, calculated from L vector:
```

```
X = [L(1);L(1)+L(2);L(1)+L(2)+L(3);L(1)+L(2)+L(3)+L(4); ...
    L(1)+L(2)+L(3)+L(4)+L(5)];


% The wavelength range of interest:
Lamb = 4:0.05:12;


for kkk = 1:length(Lamb) % Loop begins

w = 2*pi*c/(Lamb(kkk)*1e-6); % Omega

for i = 1:length(eps_r)
    eps(i) = eps_0*(eps_r(i)-j/(w*rho(i)*eps_0));
    % The characteristic impedance (eta) of each medium is calculated:
    eta(i) = 1/sqrt(mu_0/eps(i));
    % The propagation constant (k) of each medium is calculated:
    k(i) = w*sqrt(mu_0*eps(i));
end

r = zeros(length(eps_r),1); % Reflection coeff. vector initialized
t = zeros(length(eps_r),1); % Transmission coeff. vector initialized

% The last boundary condition (at the mirror surface):
r(length(eps_r)) = 0.1; % Taken arbitrarily, doesn't affect the result.
t(length(eps_r)) = -r(length(eps_r))*exp(2*j*k(length(eps_r))* ...
                    X(length(eps_r)));

% By using a backwards iteration, t and r vectors are found:
for i = length(eps_r)-1:-1:1
    t(i)=(1/(2*exp(-j*k(i)*X(i))))* ...
         ((t(i+1)*exp(-j*k(i+1)*X(i))*((eta(i+1)/eta(i))+1)) + ...
         (r(i+1)*exp(j*k(i+1)*X(i))*(-(eta(i+1)/eta(i))+1)));
    r(i)=(1/(2*exp(j*k(i)*X(i))))* ...
         ((t(i+1)*exp(-j*k(i+1)*X(i))*((-eta(i+1)/eta(i))+1)) + ...
         (r(i+1)*exp(j*k(i+1)*X(i))*((eta(i+1)/eta(i))+1)));
end

ratio = 2/(t(1)+r(1)+(eta(1)/eta0)*(t(1)-r(1))); % Normalization factor

for i = 1:1:length(eps_r)
```

```
    t(i)=t(i)*ratio;
    r(i)=r(i)*ratio;
end

% t0 and r0 are calculated from r1 and t1.
t0 = 0.5*(t(1)*(1+eta(1)/eta0)+r(1)*(1-eta(1)/eta0));
r0 = t(1)+r(1)-t0;

E1 = t(1)+r(1); % The E field at boundary X = 0
H1 = eta(1)*(t(1)-r(1)); % The H field at boundary X = 0

% The E and H field at boundary X = X(1):
E2 = t(2)*exp(-j*k(2)*X(1)) + r(2)*exp(j*k(2)*X(1));
H2 = eta(2)*t(2)*exp(-j*k(2)*X(1)) - eta(2)*r(2)*exp(j*k(2)*X(1));



% The E and H field of the incident field:
Ein = t0;
Hin = eta0*t0;

% To find eta when there is no substrate absorption:
eta(kkk)=((abs(t0))^2-(abs(r0))^2)/((abs(t0))^2);

% To find eta when substrate absorption is present,
% the Poynting Vector is calculated.
% Power at Boundary 1 - Power at Boundary 5 =
%               Absorbed power between 1 and 5
% Absorbed power / input power = eta_prime
eta_prime(kkk) = ...
(real(E1*conj(H1)) - real(E2*conj(H2)))/real(Ein*conj(Hin));
% Note: eta_prime gives more accurate results
%       than eta for the test structures.

end % Loop ends

figure;
plot(Lamb,eta_prime);
```

Appendix C

Matlab Script for Calculation of the Thermal Parameters of the Test Structures

The following Matlab script is used to calculate the thermal parameters of the fabricated PolyMUMPs test structures.

```
clear all;
syms x; % x is defined as a symbol
RESOL = 100; % Resolution for beta
% COUNT_MAX: The number of iterations. In the model, this number is
% infinite, but the temperature distribution converges after a small
% value of COUNT_MAX, like 4.
COUNT_MAX = 4;

L1 = 40e-6; % Microplate length
W1 = 40e-6; % Microplate width
L2 = 40e-6; % Arm length
W2_polysi = 10e-6; % Arm width (polysilicon)
W2_gold = 4e-6; % Arm width (gold)
th_polysi = 1.5e-6; % Thickness (polysilicon)
th_gold = 0.5e-6; % Thickness (gold)

k_polysi = 41; % Thermal conducticity (polysilicon)
k_gold = 320; % Thermal conducticity (gold)
g_polysi = 753*2330; % Volumetric heat capacity (polysilicon)
g_gold = 19300*129; % Volumetric heat capacity (gold)
```

```
x1 = 0; % Leftmost boundary (midplate)
x2 = L1/2; % The interface
x3 = x2 + L2; % Rightmost boundary (anchor)

% Calculation of the constriction resistance R_c:
eps = W2_polysi/W1;
dummy = 1; % dummy = 1 for shape-B and dummy = 2 for shape-A
R_c = ((eps+(1/eps))*log((1+eps)/(1-eps))+2*log((1-(eps^2))/(4*eps))) ...
    /(dummy*pi*k_polysi*th_polysi);
h_c = (1/R_c)/(W1*th_polysi); % The thermal contact conductance (K/W/m^2)

% 3D to 2D conversion:
k2_2D = ...
 (k_polysi*W2_polysi*th_polysi+k_gold*W2_gold*th_gold)/(W2_polysi*th_polysi);
g2_2D = ...
 (g_polysi*W2_polysi*th_polysi+g_gold*W2_gold*th_gold)/(W2_polysi*th_polysi);

% 2D to 1D conversion:
k2_1D = (W2_polysi/W1)*(k2_2D);
k1_1D = k_polysi;
g2_1D = (W2_polysi/W1)*(g2_2D);
g1_1D = g_polysi;

% Thermal diffusivity of region 1 and 2:
al1 = k1_1D/g1_1D;
al2 = k2_1D/g2_1D;

Q = 1e10; % Heat generation rate (arbitrary value)

% The composite region solution:
beta = 1/RESOL; % The minimum value of the eigenvalue (beta)
% The elements of the boundary conditions matrix are found:
t1 = beta/sqrt(al1);
t2 = beta/sqrt(al2);
a1 = -t1*sin(t1*x1);
a2 = t1*cos(t1*x1);
b1 = (-k1_1D/h_c)*(-t1*sin(t1*x2))-cos(t1*x2);
b2 = (-k1_1D/h_c)*(t1*cos(t1*x2))-sin(t1*x2);
b3 = cos(t2*x2);
b4 = sin(t2*x2);
```

```
c1 = (-k1_1D/k2_1D)*t1*sin(t1*x2);
c2 = (k1_1D/k2_1D)*t1*cos(t1*x2);
c3 = t2*sin(t2*x2);
c4 = -t2*cos(t2*x2);
d3 = cos(t2*x3);
d4 = sin(t2*x3);
% The boundary conditions matrix:
A = [a1 a2 0 0; b1 b2 b3 b4; c1 c2 c3 c4; 0 0 d3 d4];
% The determinant of the matrix:
DET(1) = det(A);

COUNT = 1;
t = 1;
while COUNT<COUNT_MAX
    t = t + 1;
    beta = t/RESOL; % The temporary eigenvalue
    t1 = beta/sqrt(al1);
    t2 = beta/sqrt(al2);
    a1 = -t1*sin(t1*x1);
    a2 = t1*cos(t1*x1);
    b1 = (-k1_1D/h_c)*(-t1*sin(t1*x2))-cos(t1*x2);
    b2 = (-k1_1D/h_c)*(t1*cos(t1*x2))-sin(t1*x2);
    b3 = cos(t2*x2);
    b4 = sin(t2*x2);
    c1 = (-k1_1D/k2_1D)*t1*sin(t1*x2);
    c2 = (k1_1D/k2_1D)*t1*cos(t1*x2);
    c3 = t2*sin(t2*x2);
    c4 = -t2*cos(t2*x2);
    d3 = cos(t2*x3);
    d4 = sin(t2*x3);
    A = [a1 a2 0 0; b1 b2 b3 b4; c1 c2 c3 c4; 0 0 d3 d4];
    DET(t) = det(A);
    if DET(t)*DET(t-1)<0
        BETA(COUNT)=(t-1)/RESOL; % Eigenvalue vector
        COUNT = COUNT+1;
    end
end

syms C1; % The coefficient C1 is defined as a symbol.
for i = 1:COUNT-1
    t1 = BETA(i)/sqrt(al1);
```

```
    t2 = BETA(i)/sqrt(al2);
    % For each i, the coefficients D1, D2 and C2 are found, in terms of
    % C1, which is defined as a symbol.
    D1 = 0;
    D2 = (k1_1D/k2_1D)*(sqrt(al2/al1))* ...
      C1*(-sin(t1*x2)/(cos(t2*x2)+ (tan(t2*x3)*sin(t2*x2))));
    C2 = -D2*tan(t2*x3);

    NUM_INT = int(C1*cos(t1*x),x,0,x2); % Numerator of the integral
    %Denominator of the integral:
    DENOM_INT = int(((k1_1D/al1)*((C1*cos(t1*x))^2)),x,0,x2) + ...
        int(((k2_1D/al2)*(((C2*cos(t2*x))+(D2*sin(t2*x)))^2)),x,x2,x3);

    % RES(i) equals ith element of the excess temperature theta_r (x,t):
    RES(i) = double(int(((C1*cos(t1*x))),x,0,x2)*(NUM_INT/DENOM_INT));
    RES(i) = RES(i)/((BETA(i))^2);
end

SUMMATION = 0;
for i =1:COUNT-1  % The elements RES are added up.
    SUMMATION = SUMMATION + RES(i);
end
% The temperature distribution Theta:
Theta = SUMMATION*Q/x2;

% The thermal conductance and thermal capacitance:
G = (Q*L1*W1*th_polysi)/Theta;
C = G/(BETA(1)^2);
```

Appendix D

ANSYS Script for the Actuator Finite Element Model

The following script demonstrates the finite element model simulation of the electrostatic actuation mechanism of the test structures.

1. The actuation voltage, material constants and geometrical parameters are defined. MicroMKS units are used.

```
*SET,voltage1,5 ! Voltage of the Poly 2 microplate
*SET,voltage2,0 ! Voltage of the Poly 0 base plate

*SET,E_poly,162e3 ! Young's modulus of polysilicon
*SET,PR_poly,0.22 ! Poisson's ratio of polysilicon
*SET,d_poly,2330e-18 ! Density of polysilicon

*SET,E_gold,78e3 ! Young's modulus of gold
*SET,PR_gold,0.44 ! Poisson's ratio of gold
*SET,d_gold,19300e-18 ! Density of gold

*SET,L1,160
*SET,Lp,120
*SET,Wp,120
*SET,Lg1,(L1-3)
*SET,Lg2,10
*SET,Lg3,(Wp-6)
*SET,W1,10
*SET,Wg1,4
```

```
*SET,enc1,3
*SET,enc2,5
*SET,W2,Wg1+enc1+enc1
*SET,g1,4
*SET,t_poly0,0.5
*SET,t_poly2,1.5
*SET,t_ox,(3.3)
*SET,t_gold,0.5
```

2. The 3D model of the test structure is drawn.

```
/PREP7
emunit,epzro,8.854e-6

! Poly2 parts:
BLOCK,0,L1,0,W1,t_ox,(t_ox+t_poly2)
BLOCK,(L1-W2),L1,W1,W1+g1,t_ox,(t_ox+t_poly2)
BLOCK,(L1-Lp),L1,W1+g1,W1+g1+Wp,t_ox,(t_ox+t_poly2)
BLOCK,L1-Lp,L1-Lp+W2, W1+g1+Wp,W1+g1+Wp+g1,t_ox,(t_ox+t_poly2)
BLOCK,L1-Lp,2*L1-Lp, W1+g1+Wp+g1,W1+g1+Wp+g1+W1,t_ox,(t_ox+t_poly2)
VADD,ALL

! Gold parts:
BLOCK,0,Lg1,enc1,enc1+Wg1,t_ox+t_poly2,t_ox+t_poly2+t_gold
BLOCK,Lg1-Wg1,Lg1,enc1+Wg1,enc1+Wg1+Lg2,t_ox+t_poly2,
      t_ox+t_poly2+t_gold
BLOCK,Lg1-Lg3,Lg1, enc1+Wg1+Lg2,enc1+2*Wg1+Lg2,t_ox+t_poly2,
      t_ox+t_poly2+t_gold
BLOCK,Lg1-Lg3,Lg1,-enc1+Lg2+Wp,-enc1+Lg2+Wp+Wg1,t_ox+t_poly2,
      t_ox+t_poly2+t_gold
BLOCK,L1-Lp+enc1,L1-Lp+enc1+Wg1,-enc1+Lg2+Wp+Wg1,-enc1+2*Lg2+Wp+Wg1,
      t_ox+t_poly2,t_ox+t_poly2+t_gold
BLOCK,L1-Lp+enc1,L1-Lp+enc1+Lg1,2*Lg2+Wp+Wg1-enc1,2*Lg2+Wp+2*Wg1-enc1,
      t_ox+t_poly2,t_ox+t_poly2+t_gold
VADD,1,2,3,4,5,7

! Poly0 layer:
BLOCK,  L1-Lp-enc2,L1+enc2,-enc2+W1+g1,enc2+W1+g1+Wp,0,t_poly0

! Air:
BLOCK,  -1.5*enc2*10,2*L1-Wp+1.5*enc2*10,-2*enc2*10+W1+g1,
        2*enc2*10+W1+g1+Wp,-3*MICRON,8*MICRON
```

```
VSEL,ALL
VOVLAP,ALL
NUMCMP,VOLU
ALLSEL,ALL
```

3. Material properties and element types are defined and assigned to volumes

```
! The volumes:
! Volume 1: poly 0 plate
! Volume 2: gold
! Volume 3: gold
! Volume 4: poly2 structure
! Volume 5: surrounding air, including the gap

ET,1,SOLID122
ET,2,SOLID122



mp,perx,3,1
! Let's make material 3 = air
!            material 1 = poly2
!            material 2 = gold
!            material 4 = poly0

VSEL,S,,,4,,,   ! poly2
VATT,1,,1,    ! material 1, type 1

VSEL,S,,,2,,,   ! gold
VSEL,A,,,3,,,
VATT,2,,1,        ! material 2, type 1

VSEL,S,,,5,,,   ! air
CM,air,VOLU
VATT,3,,2,    ! material 3, type 2
```

4. Meshing is done using smart-meshing feature.

```
ALLSEL,ALL
SMRTSIZE,6
MSHAPE,1,3D
VSEL,S,,,4,,,   ! poly2
```

```
VMESH,ALL
SMRTSIZE,8
VSEL,S,,,2,,,     ! gold
VSEL,A,,,3,,,     ! gold
VMESH,ALL
SMRTSIZE,8
VSEL,S,,,5,,,     ! air
VMESH,5
```

5. The voltages are applied to the Poly0 and Poly2 layers, and the electrostatic environment is saved to the physics file, ELECTROS.

```
ALLSEL,ALL
VSEL,S,,,1,,,   ! Poly 0
ASLV,S
DA,ALL,volt,voltage2

VSEL,S,,,4,,,   ! Poly 2
VSEL,A,,,2,,,     ! Gold
VSEL,A,,,3,,,     ! Gold
ASLV,S
DA,ALL,volt,voltage1
allsel,all

ET,1,0 ! Element type of the microbolometer
! The electrostatic environment is saved:
physics,write,ELECTROS
physics,clear
```

6. Material properties are assigned to the volumes for the structural analysis

```
ET,1,SOLID95 ! Element type of the microbolometer
ET,2,0 ! Element type of the surrounding air

MP,EX,1,E_poly
mp,nuxy,1,PR_poly
MP,EX,2,E_gold
mp,nuxy,2,PR_gold
```

7. Boundary conditions are defined as fixed arm connections to the substrate.

```
VSEL,S,,,4,,,   ! poly2
```

```
VSEL,A,,,2,,,     ! gold
VSEL,A,,,3,,,     ! gold
ASLV,S

DA,88,UX,0 !substrate connection 1 (poly2)
DA,88,UY,0
DA,88,UZ,0

DA,62,UX,0 !substrate connection 1 (gold)
DA,62,UY,0
DA,62,UZ,0

DA,87,UX,0 !substrate connection 2 (poly2)
DA,87,UY,0
DA,87,UZ,0

DA,8,UX,0 !substrate connection 2 (gold)
DA,8,UY,0
DA,8,UZ,0

allsel,all
finish
physics,write,STRUCTURE
```

8. The solution is found using the ESSOLV macro.

```
ESSOLV,'ELECTROS', 'STRUCTURE',3,0,'air',,,,15
finish
```

9. Finally, the structural deformations are plotted.

```
/post1
vsel,all
PLNSOL, U,SUM, 0,1.0
```

Appendix E

The Parameters calculated by the Electrostatic-Structural Model

In this appendix, the parameters calculated by the electrostatic-structural model are presented in tabular form. The parameters for design T80 are given in Table E.1 and the parameters for design T120 are given in Table E.2. Note that since both design T80 and T120 have the same composite section, they have the same area moment of inertia and bending stiffness.

Table E.1: The parameters calculated by the electrostatic-structural model, for design T80.

Parameter	Description	Value
I_{comp} (m^4)	Area moment of inertia of the transformed section	2.59×10^{-24}
$E_{Poly2}I_{comp}$ (Nm^2)	Bending stiffness of the transformed section	4.09×10^{-13}
A_1	Coefficient (Eq. 3.71)	0.87
A_2	Coefficient (Eq. 3.72)	2.54
B_1	Coefficient (Eq. 3.73)	0.13
B_2	Coefficient (Eq. 3.74)	1.54
Γ	Coefficient (Eq. 3.75)	0.44
Λ	Coefficient (Eq. 3.76)	2.38
KG	Torsional stiffness (Eq. 3.58)	2.38
k_{eq} (N/m)	Equivalent spring constant (Eq. 3.57)	2.55

Table E.2: The parameters calculated by the electrostatic-structural model, for design T120.

Parameter	Description	Value
I_{comp} (m^4)	Area moment of inertia of the transformed section	2.59×10^{-24}
$E_{Poly2}I_{comp}$ (Nm^2)	Bending stiffness of the transformed section	4.09×10^{-13}
k_{eq} (N/m)	Equivalent spring constant (Eq. 3.57)	2.40

References

[1] D. Murphy, M. Ray, R. Wyles, J. Asbrock, N. Lum, J. Wyles, C. Hewitt, A. Kennedy, and D. Van Lue. High sensitivity 25 μm microbolometer FPAs. In *Proc. SPIE*, volume 4721, pages 99–110, Orlando, FL, April 2002.

[2] J. Carter, A. Cowen, B. Hardy, R. Mahadevan, M. Stonefield, and S. Wilcenski. *POLYMUMPs Design Handbook Revision v11.0*, 2005.

[3] M. Almasri, D. P. Butler, and Z. Çelik Butler. Self-supporting uncooled infrared microbolometers with low-thermal mass. *J. Microelectromech. S.*, 10:469–476, September 2001.

[4] W.-B. Song and J. J. Talghader. Adjustable responsivity for thermal infrared detectors. *Appl. Phys. Lett.*, 81(3):550–552, 2002.

[5] W.-B. Song and J. J. Talghader. Design and characterization of adaptive microbolometers. *J. Micromech. and Microeng.*, 16(5):1073–1079, May 2006.

[6] R. A. Wood and N. A. Foss. Micromachined bolometer arrays achieved low-cost imaging. *Laser Focus World*, 29:101–106, June 1993.

[7] R. T. Rajendra Kumar, B. Karunagaran, D. Mangalaraj, Sa. K. Narayandass, P. Manoravi, M. Joseph, V. Gopal, R. K. Madaria, and J. P. Singh. Determination of thermal parameters of vanadium oxide uncooled microbolometer infrared detector. *Int. J. Infrared Milli.*, 24(3):327–334, March 2003.

[8] A. Rogalski. Infrared detectors: status and trends. *Prog. Quant. Electron.*, 27:59–210, 2003.

[9] A. D. Oliver and K. D. Wise. A 1024-element bulk-micromachined thermopile infrared imaging array. *Sens. Actuators A*, 73:222–231, 1999.

[10] Y. Zhao, M. Mao, R. Horowitz, A. Majumdar, J. Varesi, P. Norton, and J. Kitching. Optomechanical uncooled infrared imaging system: Design, microfabrication and performance. *J. Microelectromech. S.*, 11:136–146, April 2002.

[11] J. D. Vincent. *Fundamentals of Infrared Detector Operation and Testing.* Wiley, New York, Toronto, 1990.

[12] A. Tanaka, S. Matsumoto, N. Tsukamoto, S. Itoh, T. Endoh, A. Nakazato, Y. Kumazawa, M. Hijikawa, H. Gotoh, T. Tanaka, and N. Terenashi. Silicon IC process compatible bolometer infrared focal plane array. In *Proc. Int. Conf. Solid State Sens. Actuators, 8th*, volume 2, pages 632–635, Stockholm, June 1995.

[13] J. S. Shie and P. K. Weng. Design considerations of metalfilm bolometer with micromachined floating membrane. *Sens. Actuators*, A33:183–189, 2002.

[14] L. Dong, R. Yue, and L. Liu. An uncooled microbolometer infrared detector based on Poly-SiGe thermistor. *Sens. Actuators A*, 105:286–292, 2003.

[15] S. Sedky, P. Fiorini, M. Caymax, C. Baert, L. Hermans, and R. Mertens. Characterization of bolometers based on polycrystalline silicon germanium alloys. *Electron Devic. Lett.*, 19:376–378, October 1998.

[16] J. L. Tissot, C. Trouilleau, B. Fieque, A. Crastes, and O. Legras. Uncooled microbolometer detector: Recent developments at ULIS. *Opto-Electron. Rev.*, 14(1):25–32, 2006.

[17] E. Iborra, M. Clement, L. V. Herrero, and J. Sangrador. IR uncooled bolometers based on amorphous $Ge_1Si_{1-x}O_y$ on silicon micromachined structures. *J. Microelectromech. S.*, 11:322–329, August 2002.

[18] A. Ahmed and R. N. Tait. Noise behavior of amorphous $Ge_xSi_{1-x}O_y$ for microbolometer applications. *Infrared Phys. Techn.*, 46:468–472, January 2005.

[19] B. I. Craig, R. J. Watson, and M. H. Unewisse. Anisotropic excess noise within a-Si:H. *Solid-State Electron.*, 39:807–812, 1996.

[20] H. Wang, X. Yi, G. Huang, J. Xiao, X. Li, and S. Chen. Room temperature bolometric applications using manganese oxide thin films. *Infrared Phys. Techn.*, 45(1):53–57, January 2004.

[21] X. Yi, C. Chen, L. Liu, Y. Wang, B. Xiong, H. Wang, and S. Chen. A new fabrication method for vanadium dioxide thin films deposited by ion beam sputtering. *Infrared Phys. Techn.*, 44(2):137–141, April 2003.

[22] D. Murphy, M. Ray, R. Wyles, J. Asbrock, N. Lum, A. Kennedy, J. Wyles, C. Hewitt, G. Graham, W. Radford, J. Anderson, D. Bradley, R. Chin, and T. Kostrzewa. High sensitivity (25 μm pitch) microbolometer FPAs and application development. In *Proc. SPIE*, volume 4369, pages 222–234, Orlando, FL, April 2001.

[23] H. Jerominek, F. Picard, and D. Vincent. Vanadium oxide films for optical switching and detection. *Opt. Eng.*, 32(9):2092–2099, 1993.

[24] P. W. Kruse and D. D. Skatrud. *Uncooled Infrared Imaging Arrays and Systems*. Academic Press: Vol. 47, San Diego, 1997.

[25] L. A. L. Almeida, G. S. Deep, A. M. Lima, and H. Neff. Modeling of the hysteretic metal-insulator transition in a vanadium dioxide infrared detector. *Opt. Eng.*, 41(10):2582–2588, October 2002.

[26] P. C. Shan, Z. Celik-Butler, D. P. Butler, A. Jahanzeb, C. M. Travers, W. Kula, and R. Sobolewski. Investigation of semiconducting YBaCuO thin films: A new room temperature bolometer. *J. Appl. Phys.*, 80(12):7118–7123, December 1996.

[27] R. Sobolewski, D. P. Butler, and Z. Celik-Butler. Cooled and uncooled infrared detectors based on yttrium barium copper oxide. In *Proc. SPIE*, volume 4318, pages 204–214, Vilnius, Lithuania, March 2001.

[28] T. Ichirara, Y. Watabe, Y. Honda, and K. Aizawa. A high performance amorphous $Si_{1-x}C_x$:H thermistor bolometer based on micro-machined structure. In *Solid State Sensors and Actuators, 1997. TRANSDUCERS '97 Chicago., 1997 International Conference on*, volume 2, pages 1253–1256, Chicago, IL, June 1997.

[29] F. Yang, L. Méchin, J.-M. Routoire, and B. Guillet. Low noise $La_{0.7}Sr_{0.3}MnO_3$ thermometers for uncooled bolometric applications. *J. Appl. Phys.*, 99:024903, January 2006.

[30] R. J. Choudhary, A. S. Ogale, S. R. Shinde, S. Hullavarad, S. B. Ogale, T. Venkatesan, R. N. Bathe, S. I. Patil, and R. Kumar. Evaluation of manganite films on silicon for uncooled bolometric applications. *Appl. Phys. Lett.*, 84:3846–3848, May 2004.

[31] M. A. Todd, P. P. Donohue, P. J. Wright, M. J. Crosbie, P.A. Lane, M.-H. Jo, B. S. H. Pang, and M. G. Blamire. Colossal magnetoresistive manganite thin-films for infrared detection and imaging. *Ann. Phys.*, 13(1-2):48–51, 2004.

[32] A.-M. Haghiri-Gosnet and J.-P. Renard. CMR manganites: Physics, thin films and devices. *J. Phys. D: Appl. Phys.*, 36:R127–R150, April 2003.

[33] J. H. Hao, X. Mao, C. H. Chen, and D. X. Lu. Room temperature bolometric applications using manganese oxide thin films. *Int. J. Infrared Milli.*, 20(12):R127–R150, 1999.

[34] J.-L. Tissot, F. Rothan, C. Vedel, M. Vilain, and J.-J. Yon. LETI/LIR's uncooled microbolometer development. In *Proc. SPIE*, volume 3436, pages 605–610, San Diego, CA, July 1998.

[35] H. Jerominek, T. D. Pope, C. Alain, R. Zhang, F. Picard, M. Lehoux, F. Cayer, S. Savard, C. Larouche, and C. Grenier. Miniature $v0_2$-based bolometric detectors for high-resolution uncooled FPAs. In *Proc. SPIE*, volume 4028, pages 47–56, Orlando, FL, April 2000.

[36] S.-B. Ju, Y.-J. Yong, and S.-G. Kim. Design and fabrication of a high fill-factor micro-bolometer using double sacrificial layers. In *Proc. SPIE*, volume 3698, pages 180–189, Orlando, FL, April 1999.

[37] M. Almasri, Z. Celik-Butler, D. P. Butler, A. Yaradanakul, and A. Yildiz. Uncooled multimirror broad-band infrared microbolometers. *J. Microelectromech. S.*, 11(5):528–535, October 2002.

[38] N. Nelms and J. Dowson. Goldblack coating for thermal infrared detectors. *Sens. Actuators A*, 120:403–407, February 2005.

[39] P. Merel, P. Laou, and F. Wong. Enhancement of YBCO microbolometer performances with regionally thinned microbridges. In *Proc. SPIE*, volume 5783, pages 607–615, Orlando, FL, April 2005.

[40] K. C. Liddiard. Thin-film resistance bolometer IR detectors. *Infrared Phys.*, 24:57–64, January 1984.

[41] M A Yaradanakul. *Room Temperature Infrared Microbolometers on a Flexible Substrate*. PhD thesis, Southern Methodist University, 2002.

[42] R. N. Supino and J. J. Talghader. Average optical power monitoring in micromirrors. *IEEE J. Selected Topics in Quantum Electronics*, 8:12–18, January 2002.

[43] J. J. Talghader. Thermal and mechanical phenomena in micromechanical optics. *J. Phys. D Appl. Phys.*, 37:R109–R122, May 2004.

[44] P. Eriksson, J. Y. Andersson, and G. Stemme. Thermal characterization of surface-micromachined silicon nitride membranes for thermal infrared detectors. *J. Microelectromech. S.*, 6:55–61, March 1997.

[45] M. Almasri, B. Xu, and J. Castracane. Amorphous silicon two-color microbolometer for uncooled IR detection. *IEEE Sens. J.*, 6:293–300, April 2006.

[46] W. M. Rohsenow, J.P. Hartnett, and Y. Cho. *Handbook of Heat Transfer*. McGraw-Hill, New York, 1998.

[47] R. Siegel and J. R. Howell. *Thermal Radiation Heat Transfer*. Taylor & Francis, New York, 2002.

[48] V. N. Leonov and D. P. Butler. Two-color thermal detector with thermal chopping for infrared focal-plane arrays. *Appl. Optics*, 40(16):2601–2610, 2001.

[49] A. K. Bhaskar, M. Packirisamy, and R. B. Bhat. Modeling switching response of torsional micromirrors for optical microsystems. *Mech. Mach. Theory*.

[50] J. M. Bustillo, G. K. Fedder, C. T.-C. Nguyen, and R. T. Howe. Process technology for the modular integration of CMOS and polysilicon microstructures. *Microsyst. Technol.*

[51] F. P. Beer. *Mechanics of materials*. McGraw-Hill, New York, 1981.

[52] S. R. Swanson. Torsion of laminated rectangular rods. *Compos. Struct.*, 42(1):23–31, May 1998.

[53] S.-J. Yoo. *Micromachined Wavelength Microbolometer Sensors Operating at Room Temperature*. PhD thesis, University of Texas, Austin, 2000.

[54] D. K. Cheng. *Fundamentals of Engineering Electromagnetics*. Addison-Wesley, Dedham.

[55] A. J. Chapman. *Heat Transfer*. MacMillan, New York, 1984.

[56] P. E. Bulavin and V. M. Kashcheev. Solution of nonhomogenous heat conduction equation for multilayered bodies. *Int. Chem. Eng.*, 5:112–115, 1965.

[57] M. N. Ozisik. *Boundary Value Problems of Heat Conduction*. International Textbook Co., Scranton, PA, 1968.

[58] M. Cooper, B. Mikic, and M. M. Yovanovich. Thermal contact conductance. *J. Mass Heat Transfer*, 12:279–300, 1969.

[59] M. R. Sridhar and M. M. Yovanovich. Review of elastic and plastic contact conductance models: Comparison with experiment. *J. Thermophys. Heat Tr.*, 8(4):633–640, 1994.

[60] B. Mikic, B. Mikic, and M. M. Yovanovich. Thermal contact conductance: Theoretical considerations. *Int. J. Heat Mass Transfer*, 17:205–214, 1974.

[61] F. H. Milanez, M. M. Yovanovich, and J. R. Culham. Effect of surface asperity truncation on thermal contact conductance. *IEEE T. Compon. Pack. T.*, 26(1):48–54, March 2003.

[62] F. H. Milanez, M. M. Yovanovich, and M. B. H. Mantelli. Thermal contact conductance at low contact pressures. *J. Thermophys. Heat Tr.*, 18(1):37–44, 2004.

[63] Ansoft - HFSS. http://www.ansoft.com/products/hf/hfss/.

[64] Profilometer. http://en.wikipedia.org/wiki/Profilometer.

[65] WYKO NT1100 Optical Profiling System. http://www.veeco.com/pdfs/datasheets/nt110020reva520final_394.pdf.

[66] L. M. Phinney, G. Lin, J. Wellman, and A. Garcia. Surface roughness measurements of micromachined polycrystalline silicon films. *J. Micromech. Microeng.*, 14:927–931, May 2004.

[67] M. Shavezipur, A. Khajepour, and S. M. Hashemi. A novel linearly tunable butterfly-shape MEMS capacitor. *Microelectr. J.*, 39(5):756–762, May 2008.

[68] S. D. Senturia. *Microsystem Design*. Springer, New York, 2001.

[69] A. Tuantranont, T. Lomas, K. Jaruwongrungsee, A. Jomphoak, and A. Wisitsoraat. Symmetrical polyMUMPs-based piezoresistive microcantilever sensors with on-chip temperature compensation for microfluidics applications. *IEEE Sens. J.*, 8(5):543–547, May 2008.

[70] D. R. Lide, editor. *CRC Handbook of Chemistry and Physics*. CRC Press, Boca Raton, Fla., 1992-1993.

[71] S. A. Dayeh, D. P. Butler, and Z. Celik-Butler. Micromachined infrared bolometers on flexible polyimide substrates. *Sens. Actuators A*, 118:49–56, 2005.

[72] A Khajepour D Yan and R Mansour. Modeling of two-hot-arm horizontal thermal actuator. *J. Micromech. and Microeng.*, 13(2):312–322, 2003.

[73] C. T. Leondes. *MEMS/NEMS Handbook Techniques and Applications*. Springer US, New York, 2006.

[74] C. H. Mastrangelo. *Thermal applications of micro-bridges*. PhD thesis, University of California, Berkeley, 1991.

[75] K. Underhill-Shanks and M. K. Hudson. Fixed and scanning infrared raditometers for combustion studies. *Journal of Pyrotechnics*, 12:57067, 2000.

[76] H. R. Shea. Reliability of MEMS for space applications. In *Proc. SPIE*, volume 6111, page 61110A, San Jose, CA, January 2006.

[77] R. G. Driggers, P. Cox, and T. Edwards. *Introduction to Infrared and Electro-Optical Systems*. Artech House, Boston, 1999.

[78] J. L. Tissot. IR detection with uncooled sensors. *Infrared Phys. Techn.*, 46(1-2):147–153, December 2004.

[79] A. Z. Kattamis, I-C. Cheng, K. Long, B. Hekmatshoar, K. H. Cherenack, S. Wagner, J. C. Sturm, S. M. Venugopal, D. E. Loy, S. M. O'Rourke, and D. R. Allee. Amorphous silicon thin-film transistor backplanes deposited at 200°c on clear plastic for lamination to electrophoretic displays. *J. Display Technol.*, 3(3):304–308, September 2007.

[80] M. P. Thompson, J. R. Troxell, M. E. Murray, C. M. Thrush, and J. V. Mantese. Infrared absorber for pyroelectric detectors. *J. Vac. Sci. Technol. A*, 25(3):437–440, 2007.

[81] P. G. Le Comber and J. Mort. *Electronic and structural properties of amorphous semiconductors*. Academic Press, New York, 1973.

[82] Periodic table of elements: Titanium. `http://environmentalchemistry.com/yogi/periodic/Ti.html`.

[83] M. J. Madou. *Fundamentals of Microfabrication*. CRC Press, 2001.

[84] Ellipsometer data table. http://ece-www.colorado.edu/ bart/book/ellipstb.htm. 1997.

[85] C. H. Mastrangelo, Y. C. Tai, and R. S. Muller. Thermophysical properties of low-residual stress, silicon-rich, LPCVD silicon nitride films. *Sens. Actuators*, A21/23:856–860, April 1990.

[86] B. L. Zink, R. Pietri, and F. Hellman. Thermal conductivity and specific heat of thin-film amorphous silicon. *Phys. Rev. Lett.*, 96:055902, 2006.

[87] B. Li. Design and simulation of an uncooled double-cantilever microbolometer with the potential for mk NETD. *Sens. Actuators A*, 112:351–359, 2004.

[88] G. E. McGuire. *Semiconductor Materials and Process Technology Handbook*. William Andrew Publishing, Noyes, 1988.

[89] L. B. Freund and S. Suresh. *Thin Film Materials*. Cambridge University Press, 2003.

[90] efunda: Typical properties of titanium alloys. http://www.efunda.com/materials/alloys/titanium/properties.cfm. 2009.

[91] R. Schmitt. *Electromagnetics Explained: A Handbook for Wireless/RF, EMC, and High-speed Electronics*. Newnes, 2002.

[92] R. R. Davies, M. E. McNie, K. M. Brunson, and D. J. Combes. Engineering in- and out-of-plane stress in PECVD silicon nitride for CMOS-compatible surface micromachining. In *Proc. SPIE*, volume 4557, pages 320–328, San Francisco, CA, October 2001.

[93] P. R. Scheeper, J. A. Voorthuyzen, and P. Bergveld. PECVD silicon nitride diaphragms for condenser microphones. *Sens. Actuators B*, 4:79–84, 1991.

[94] W.-B. Song and J. J. Talghader. Fabrication of adaptive microbolometers. *Proc. SPIE*, 5406:566–576, 2004.

[95] N. Topaloglu, P. M. Nieva, M. Yavuz, and J. P. Huissoon. Modeling of thermal conductance in uncooled microbolometer pixel. Submitted to Sensors and Actuators A: Physical.

[96] N. Topaloglu, P. M. Nieva, M. Yavuz, and J. P. Huissoon. A novel method for estimating the thermal conductance of uncooled microbolometer pixels. In *ISIE'07 IEEE International Symposium on Industrial Electronics*, pages 1554–1558, Vigo, Spain, June 2007.

[97] N. Topaloglu, P. M. Nieva, M. Yavuz, and J. P. Huissoon. Thermal modeling of thermally isolated microplates. In *Proc. SPIE*, volume 6926, page 69260U, San Diego, CA, March 2008.

[98] N. Topaloglu, P. M. Nieva, M. Yavuz, and J. P. Huissoon. Thermal conductance estimation for uncooled microbolometer pixels. In *Proc. of 21st Canadian Congress of Applied Mechanics (CANCAM'07)*, pages 740–741, Vigo, Spain, June 2007.

[99] N. Topaloglu, P. M. Nieva, M. Yavuz, and J. P. Huissoon. An effective thermal conductance tuning mechanism for uncooled microbolometers. Submitted to Journal of Micromechanics and Microengineering.

[100] N. Topaloglu, P. M. Nieva, M. Yavuz, and J. P. Huissoon. A pixel-by-pixel thermal conductance tuning mechanism for uncooled microbolometers. In *Microsystems and Nanoelectronics Research Conference, MNRC 2008. 1st*, pages 201–204, October 2008.